Accretion flows in compact binary stars

Coel Hellier

Mullard Space Science Laboratory
Department of Physics and Astronomy
University College London

A thesis submitted to the University of London
for the degree of Doctor of Philosophy

September 1989

Summary

The thesis describes an observational study of accretion flows occurring in close binary stars where one binary component is a degenerate star (white dwarf or neutron star). In particular it focuses upon the 'intermediate polar' sub-class in which the compact white dwarf possesses a substantial magnetic field able to control the accretion flow.

After an introductory chapter, I report the analysis of spectroscopy of the eclipsing intermediate polar EX Hya. To explain the data I propose a new model for the optical modulations at the spin period of the white dwarf.

The next chapter contains the first spectra of EX Hya obtained during one of its rare outbursts. The analysis suggests that this outburst was caused by an increase in the mass transfer rate from the secondary star, rather than by an instability in an accretion disc as in the alternative model for such outbursts.

I then describe the most extensive spectroscopic study of the intermediate polar FO Aqr to date. The data confirm the model for the spin period modulations proposed for EX Hya, which suggests the model's applicability to the whole intermediate polar class. The data show that this binary is also eclipsing, whereas previously it had been thought to be at low inclination. I also report a unique 'absorption S-wave' feature in the emission lines which is blue-shifted by 200 $\mathrm{km\,s^{-1}}$ from the line centers.

A final chapter explores another sub-class of interacting binary stars, the high inclination Low Mass X-ray Binaries (which contain a neutron star). In the system X 1822–371, the direct X-ray flux from the neutron star is obscured by material in the accretion disc. We see only X-rays scattered by a 'corona' around the disc. This provides an excellent opportunity to study the accretion flow which I exploit using X-ray data from the EXOSAT satellite.

Contents

List of Figures

List of Tables

CHAPTER 1

Introductory

This thesis is concerned with compact binary stars; systems in which at least one component is a degenerate object (white dwarf or neutron star) or a black hole. In particular I discuss the 'semi-detached' systems in which the second star has the lower mass (usually a red dwarf) and is losing matter to the compact star. Systems of this type in which the compact star (primary) is a white dwarf are known as Cataclysmic Variables (CV) while those containing neutron stars or black holes are the Low Mass X-ray Binaries (LMXB).

1.1 Mass transfer and accretion flows

The equipotential surfaces in a binary system are nearly spherical close to a star, but are substantially distorted where the gravitational attractions of the two stars are comparable. The Roche-lobe is the particular equipotential surface where the distorted spheres from each star first meet as their size is increased. The junction, called the inner Lagrangian point, is thus the boundary and the lowest energy path between the regions controlled by the two stars.

If the secondary star overfills its Roche-lobe then matter will transfer through the Lagrangian point and eventually accrete onto the compact primary. When the secondary is the lower mass star, mass-transfer will cause the Roche-lobe of the secondary to expand away from the star, ceasing the mass transfer. Stable mass transfer results only if either the secondary star radius is increasing (because of internal evolution, for instance) or if the Roche-lobe is shrinking for other reasons. The evolutionary time-scale for a low mass star, though, is longer than the age of the Galaxy. It is generally believed that the mechanism responsible for mass transfer is a loss of orbital angular momentum from the binary system causing the separation of the stars to decrease and so shrinking their Roche-lobes.

At long periods, >3 hours, the angular momentum loss is believed to be caused by the magnetic wind of the secondary star coupling with the interstellar medium (Eggleton 1976). This is sufficient to drive mass transfer rates of $\sim 10^{-9}\ M_{\odot}\ \mathrm{yr}^{-1}$. As the system

evolves to shorter periods, the secondary becomes smaller and, at ~ 3 hours, becomes fully convective and loses its magnetic wind. The secondary, which is out of thermal equilibrium due to the mass transfer, shrinks back to equilibrium and detaches from its Roche-lobe — thus mass transfer ceases (Rappaport, Verbunt & Joss 1983; Spruit & Ritter 1983). Angular momentum is still dissipated by gravitational radiation and at a period of ~ 2 hours the Roche-lobe has shrunk sufficiently for contact and mass transfer to resume. The gravitational radiation drives a lower rate of $\sim 10^{-10}\ M_\odot\ \mathrm{yr}^{-1}$. Mass transfer continues until at a period of ~ 80 mins, the secondary departs from thermal equilibrium and eventually becomes degenerate and so increases in size with further mass loss. This theory was largely developed to explain the highly significant deficit in accreting binaries observed with periods between 2 and 3 hours and also the lack of CVs with periods below 80 mins. The evolution of compact binaries has been recently reviewed by King (1988).

In considering the fate of material passing through the Lagrangian point, it is useful to contemplate the potential well into which it has fallen. For a compact star of mass M and radius R, the potential energy liberated per unit mass by the time the material settles onto the surface of the star is approximately,

$$E = \mathrm{G}M/R.$$

For a white dwarf ($M \sim 1M_\odot$, $R \sim 10^7$ m) this is 10^{13} J while for a neutron star ($M \sim 1M_\odot$, $R \sim 10$ km) it is 10^{16} J; this energy will mostly result in electro-magnetic radiation. If the gravitational energy were entirely liberated radiatively then the radiation would be characterised by

$$\hbar\nu = k\mathrm{T} \ \sim\ \mathrm{G}Mm_p/3kR, \qquad \text{where } \mathrm{m}_p = \text{proton mass.}$$

This temperature, 50 M eV for a neutron star and 100 keV for a white dwarf, is the upper limit to that attainable in an accretion shock near the surface of the compact star. The energy may, however, be liberated over several shocks and by viscous interaction, yielding lower temperatures.

The above discussion assumes that the accreting material falls directly onto the compact object. This, however, cannot generally occur owing to the orbital angular momentum possessed by the material which causes it to circulate around the compact star. Viscous forces in the circulating material produce an exchange of angular momentum so that some of the material spirals inwards and some spirals outwards, creating an 'accretion disc' in the orbital plane. The physics of an accretion disc are poorly understood; principally, the nature and magnitude of the viscosity is unknown. Many theoretical approaches assume

that the material orbits with Keplerian velocity and simplify to an axi-symmetric two-dimensional flow. The classical work of Shakura & Sunyaev (1973) suggests that the scale of turbulent viscosity is bounded by the turbulent cell size being smaller than the vertical dimension of the disc (H) and by the interaction speed being smaller than the sound speed (c_s). Thus, the viscosity, $\nu = \alpha c_s H$, where α has an upper limit of 1 and formalises the uncertainty in the viscosity.

The viscous interaction results in the dissipation of kinetic energy and heats the accretion disc to produce strong optical and UV emission. This dominates in CV discs whereas in LMXBs, reprocessed X-ray energy dominates. The spectrum of a CV accretion disc can crudely be considered as the sum of a series of black-bodies, each characterised by the local effective temperature, $\sim 4000\,\mathrm{K}$ at the outer edge to $\sim 10^6\,\mathrm{K}$ in the inner regions. In the mid-range, these sum approximately to the power-law spectrum, $F_\nu \propto \nu^{1/3}$. For extensive discussions of accretion discs and accretion in binary systems see Frank, King & Raine (1985) and Shapiro & Teukolsky (1983).

The simple picture outlined above, although in itself difficult enough for present theory, is in practice further complicated. The outer region of the disc is struck by the stream of material emanating from the secondary. The observational evidence shows that this results in marked departures from axi-symmetry. The observations also question the thin disc assumption. A further complication arises if the compact star possesses a magnetic field sufficient to disrupt the Keplerian motion and control the accretion flow. This thesis is largely an observational study of the additional complications focussing on, firstly, the intermediate polar systems containing a magnetic white dwarf, and, secondly, the sub-class of LMXB possessing an 'accretion disc corona' which provides an X-ray emitting back-cloth against which the structure of the accretion disc can be viewed. I now turn, therefore, to an introduction of these two classes of interacting binary stars.

1.2 The intermediate polars

The intermediate polars (IPs) are CVs distinguished by the presence of two or more coherent, long-lived periods seen either in the optical band, in X-rays or in both. The longer of the periods has, in all objects so far, been found to be the orbital period of the binary while the shorter period(s) are the spin period of the white dwarf and its orbital side-bands. The main properties of the known IPs are summarised in Table 1.1. There is a distinction commonly made between the systems with very short spin periods which are generally weak X-ray emitters (AE Aqr, V533 Her & DQ Her) and the stronger X-ray emitters with longer spin periods. These two groups are sometimes called the

'DQ Her stars' and 'intermediate polars' respectively — although other authors use the terms synonymously to refer to all objects. I shall use the term 'intermediate polar' to mean the longer period systems with which this thesis is primarily concerned, ignoring the shorter period systems except insofar as their properties overlap.

The reason why the spin period of the white dwarf is detected in IPs, and not in other CVs, is believed to be that the white dwarf is strongly magnetic. The magnetic field controls the later stages of accretion onto the white dwarf, channelling material onto the magnetic poles. As the magnetic axis is in general offset from the spin axis, the resulting asymmetry produces spin period modulations. In the related class of magnetic CV, the polars or AM Her stars, the magnetic field also dominates the accretion flow; however in these systems the spin period is synchronised with the orbital period resulting in only one observed periodicity and very different properties (see Cropper 1989 for a review of polars).

1.2.1 The light curves and spectrum

To illustrate typical IP behaviour, I show in Fig. 1.1 sample light curves of EX Hya and V1223 Sgr. The orbital cycle produces eclipses in a high inclination system such as EX Hya, while more usually it is seen as a quasi-sinusoidal modulation (as in V1223 Sgr), possibly due to the varying aspect of an X-ray heated face of the secondary. In the X-ray band the orbital cycle sometimes appears as broad recurrent dips. These are most prominent in the low energy X-ray light curves of EX Hya, where they precede the narrower X-ray eclipse. Such dips are believed to be due to photo-electric absorption of the central X-ray flux by material in the disc (e.g. Córdova, Mason & Kahn 1985). Where the phasing of such dips has been determined, it suggests that the absorbing material arises near the impact of the mass-transfer stream with the disc.

Prominent in the light curves shown (Fig. 1.1) are the shorter period quasi-sinusoidal modulations due to the spin cycle. In the optical band the dominant variation may be at the spin period or alternatively at the beat period between the orbital and spin periods. The spin period is identified from X-ray light curves where it always dominates (although H0542–407 also has a strong X-ray beat period modulation, Tuohy *et al.* 1986). Whether the spin or beat period dominates in the optical band is probably related to the inclination of the system; high inclination systems tend to show the spin period while face on systems tend to show the beat period. The cause of the spin period modulations will be extensively discussed in later chapters in the light of the observations presented.

Warner (1986) has discussed the orbital side-bands of the spin period commonly seen

TABLE 1.1: Properties of intermediate polars.

Object	P_{spin} (mins)	P_{other}	P_{orb} (hr)	Optical mag.	X-ray flux μJy 2–11 keV	Distance pc	Refs.
AE Aqr	0.55		9.88	11	0.5	60-140	1,2,3,4
V533 Her	1.06		6.7	14	<0.01	1200	5,6,7
DQ Her	1.18		3.67	14	<0.01	420	5,7,8,9
GK Per	5.85		47.9	10–13	0.5–9	480	7,10,11
V1223 Sgr	12.4	13.2	3.37	13	2	600:	12,13,14,15
AO Psc	13.4	14.3	3.59	14	3	100-750	12,16,17,18
BG CMi	15.2		3.24	15	0.7	800:	19,20
SW UMa†	15.9		1.36	12–17	<0.3*	140:	7,21
FO Aqr	20.9	22.8	4.85	13	0.5	250:	3,7,15,22
TV Col	31.9	5.2hr	5.49	14	2	160-500	7,23,24,25
H0542–407	32	35	6.2:	16	1.5	600:	26,27
V426 Oph†	60:		6.0:	12–13	4	100:	7,28
EX Hya	67.0		1.64	10–13	5	125:	3,4,29,30
KO Vel†	68.1	88.8	4.9	17	0.2–2		31,32
H0534–581†	126:	45:	6.5:	15	2		26,33

† status as intermediate polar unconfirmed. *detected at 0.1 μJy in 0.5–2 keV band.

(1) Patterson 1979 (2) Patterson *et al.* 1980 (3) Berriman, Szkody & Capps 1985 (4) Warner 1987 (5) Córdova, Mason & Nelson 1981 (6) Robinson & Nather 1983 (7) Patterson 1984 (8) Young & Schneider 1980 (9) Young & Schneider 1981 (10) Córdova & Mason 1984 (11) Watson, King & Osborne 1985 (12) Penning 1985 (13) Watts *et al.* 1985 (14) Osborne *et al.* 1985 (15) Bonnet-Bidaud, Mouchet & Motch 1982 (16) White & Marshall 1981 (17) Pietsch *et al.* 1987 (18) Hassall *et al.* 1981 (19) McHardy *et al.* 1984 (20) McHardy *et al.* 1987 (21) Shafter, Szkody & Thorstenson 1986 (22) Cook, Watson & McHardy 1985 (23) Watts *et al.* 1982 (24) Schrijver, Brinkman & van der Woerd 1987 (25) Bonnet-Bidaud, Motch & Mouchet 1985 (26) Tuohy *et al.* 1986 (27) Buckley & Tuohy 1989 (28) Szkody 1986 (29) Jablonski & Busko 1985 (30) Rosen, Mason & Córdova 1988 (31) Mason *et al.* 1983 (32) Kubiak & Krzeminski 1989 (33) Buckley & Tuohy 1989.

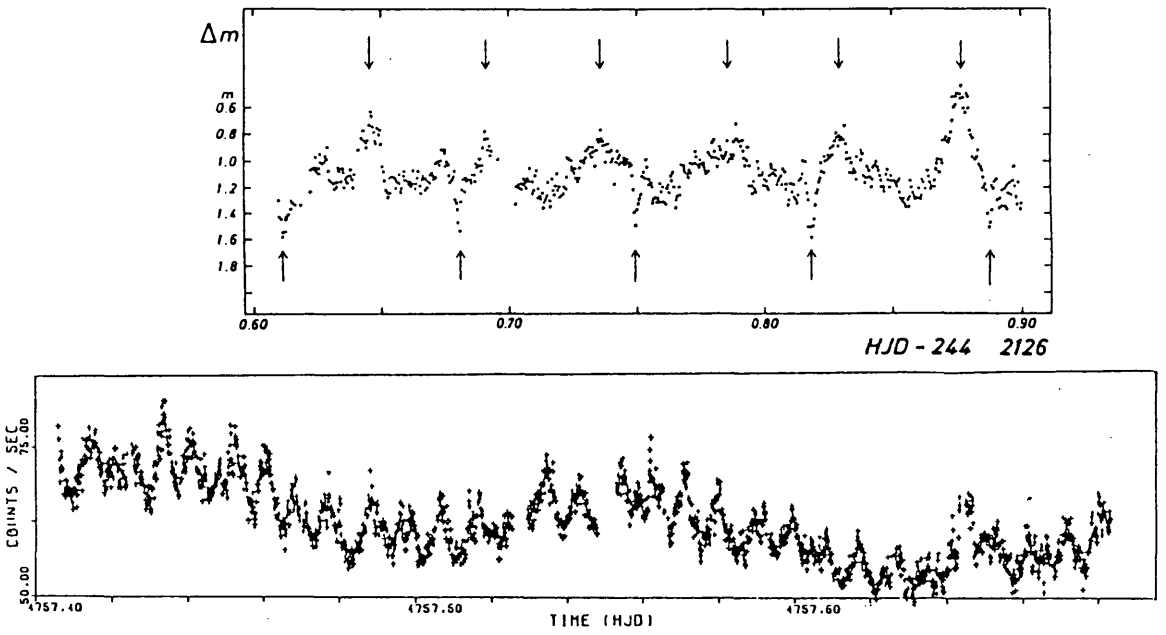

FIGURE 1.1: Typical light curves of EX Hya (upper panel) and V1223 Sgr (lower panel) displaying the twin periods characteristic of intermediate polars. From Vogt, Krzeminski & Sterken (1980) and Warner & Cropper (1984).

in intermediate polars. He predicted that reprocessing of spin pulsed flux by structure fixed in the orbital frame, together with orbital period amplitude modulation of the spin and reprocessed modulations, would produce modulations at the $\Omega - 2\omega$, $\Omega - \omega$ and $\Omega + \omega$ frequencies (Ω = orbital frequency and ω = spin frequency).

On top of the periodic behaviour discussed, all IP light curves show considerable random fluctuations (flickering) on a range of timescales. This is often sufficient to obliterate the local orbital and spin variations. There have been no reports of a quasi-periodic nature to this flickering in IPs.

Fig. 1.2 shows the optical spectrum of BG CMi, which is typical of the IP class. The hot accretion flow produces a very blue continuum together with strong doppler-broadened emission lines. The hydrogen Balmer series dominates the spectrum while He I and He II lines are also visible. The He II λ 4686 line and CN III λ 4640 blend is commonly very strong in magnetic CVs and is a useful distinguishing feature. The changes in the emission lines with the spin, orbital and beat cycles are the major topic of study of this thesis. The UV spectra of IPs also show strong emission lines with lines due to carbon and silicon as well as those due to hydrogen and helium (e.g. Verbunt 1987).

The X-ray emission arises principally near the white dwarf surface. The kinetic energy of the accreting material is turned into thermal energy by a substantial shock and the

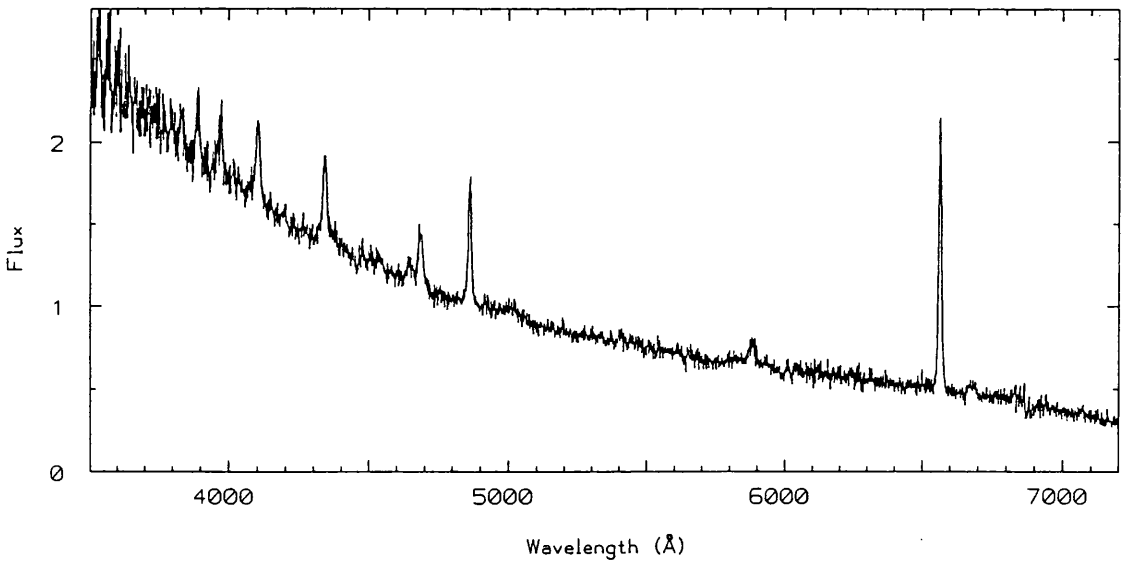

FIGURE 1.2: The optical spectrum of BG CMi showing the blue continuum and strong hydrogen and helium emission lines typical of intermediate polars.

post-shock region produces hard X-ray (~ 10 keV) bremsstrahlung emission. In IPs this radiation is usually seen through cooler material, further out in the accretion flow, and so the spectra show substantial low energy absorption (columns $10^{22} - 10^{23}$ H atom cm^{-2}). This absorbative covering is partial and spin-phase dependant and so produces complex, spin modulated spectra. For a detailed discussion of the X-ray properties of IPs, see Watson (1986), Rosen, Mason & Córdova (1988) and Norton & Watson (1989).

1.2.2 THE MAGNETIC FIELD AND THE ACCRETION FLOW

Except for the star BG CMi, there is little direct evidence that IPs contain a magnetic white dwarf. This was first proposed, by analogy with the polars, as the best explanation for the short period coherent optical modulations. In polars the magnetic field is revealed by substantial ($\sim 10\%$) circular and linear polarization of the optical light, hence the name. This results from cyclotron radiation emitted by electrons spiralling in the magnetic field. Further, cyclotron humps and Zeeman split features in the spectra of polars confirm the presence of a field, typically 10–50 MGauss (Cropper 1989).

Polarized radiation has also been found in the IP BG CMi at the $\sim 1\%$ level (Penning, Schmidt & Leibert 1986) while in other IPs any polarization is well below this level (Cropper 1986). The lower level of polarization in IPs compared with polars implies either that the fields are at least an order of magnitude lower or that the larger emitting areas in IPs causes the polarization to cancel out. Additionally, optical emission from an accretion disc (not present in polars) would dilute any polarized signal. The observed distribution of the

orbital periods of magnetic CVs supports the idea that IPs have field strengths similar to those of the polars. Polars are strongly concentrated below the period gap while IPs typically have longer periods above the gap. The summed distribution of magnetic CVs, however, is similar to that of non-magnetic CVs. Assuming that the two populations are the same, this suggests that IPs evolve into polars (become synchronised) as their periods decrease. For a discussion of these issues see King (1986) and Lamb & Melia (1986).

In the polars the narrow accretion stream emanating from the L_1 point falls on a ballistic trajectory until the energy density due to the interaction of the ions with the primary's magnetic field becomes similar to the material's kinetic energy (the 'threading region') at which point the material follows the field lines onto the white dwarf. As the spin and orbital periods are the same, the only motion with respect to the binary frame is that of the accreting material. Hence the stream remains narrow throughout.

In the non-synchronous IPs the stream approaches a magnetic field which is rotating with respect to the stream. The nature of the accretion flow between the narrow stream phase and the magnetically controlled final descent onto the white dwarf depends on whether an intermediate disc stage occurs. Hameury, King & Lasota (1986) suggested that if the effective magnetospheric radius is greater than the natural circularization radius of the stream, then no disc will form and the stream will impact directly onto the magnetosphere. The stream will tend to break up (owing to Rayleigh-Taylor instabilities) into large blobs which are not penetrated by the field and therefore continue on a ballistic (fixed in the orbital frame) trajectory — perhaps as far as the white dwarf surface. The blobs will be progressively stripped of material (by Kelvin-Helmholtz instabilities) and the stripped material will co-rotate with the magnetic field. This material may mimic many of the observed characteristics of an accretion disc. Hameury *et al.* further pointed out that if IP fields are similar to polar fields then this 'discless' accretion will occur in most IPs (all those with orbital periods $< 5\,\mathrm{hr}$).

An accretion disc may form for several reasons. For a sufficiently low magnetic field, the stream will circularize outside the magnetosphere. Also, as pointed out by Lamb & Melia (1986) a disc may form when the system has a long orbital period (and a large circularization radius). Given continuous mass transfer, such a disc would persist even as the period decreases and the circularization radius shrinks within the magnetosphere. In addition the physics of the impact of the stream with the magnetosphere is very poorly understood. A substantial shock is likely to form and result in loosely controlled co-rotating material (at the magnetosphere, the co-rotation velocity is similar to the Keplerian velocity). This narrow ring would partially screen the magnetic field as seen from greater

radii. Thus the stream may impact on the outer edge of the ring, largely unaffected by the field, and interact to produce a Keplerian disc.

If a disc is present then the outer regions are likely to be similar to those in non-magnetic CV. After transiting the disc the accreting material will encounter the 'boundary layer' between the disc and the magnetosphere. See Gosh & Lamb (1979) for a discussion of this complex region. Inside the magnetosphere the accretion flow will follow the field lines onto the white dwarf, passing through one or more shocks. The details will depend on the radial extent of the interaction region and its distance form the white dwarf, and therefore the fraction of field lines onto which material threads. This will be further discussed later in the thesis and is also considered in Rosen, Mason & Córdova (1988) and Mason, Rosen & Hellier (1988).

1.3 Low Mass X-ray Binaries

The second class of interacting binary studied in this thesis is the Low Mass X-ray Binaries (LMXB). These objects are much more X-ray luminous than the CVs (typically 10^{38} erg s^{-1} compared with 10^{33} erg s^{-1}) and have higher L_x/L_{opt} ratios (~ 1000 compared with ~ 1). The difference is explained by the LMXB possessing a neutron star (or possibly a black hole) as the compact object instead of a less compact white dwarf. The optical light is produced predominantly by reprocessing of the intense X-ray flux in the accretion disc; this results in blue spectra with high excitation emission lines, such as He II λ 4686, which are typically stronger than the Balmer lines, the reverse of the situation in CVs. Despite the greater optical luminosity of LMXB their lower space density places them, in general, at larger distances (typically a few Kpc compared with ~ 100 pc for CVs). They are therefore optically faint ($M_V \sim 16 - 20$) and so have been more intensively studied in the X-ray band where they are among the brightest objects in the sky.

Further support for the idea that LMXB contain neutron stars comes from the observation of short duration (a few minutes) bursts during which the X-ray flux may typically double. Such events are believed to be the result of thermo-nuclear ignition of accreted material on the neutron star surface. In addition, analogy can be made with the X-ray pulsars where the rates of change in the period of the short period pulsations, thought to result from the spin of the compact object, are incompatible with white dwarf primaries but consistent with neutron stars. For reviews of LMXB see McClintock & Rappaport (1985) and White & Mason (1985).

There is generally a dearth of LMXB seen at high inclinations with few showing deep X-ray eclipses. This suggests that a selection effect is in operation and it is generally

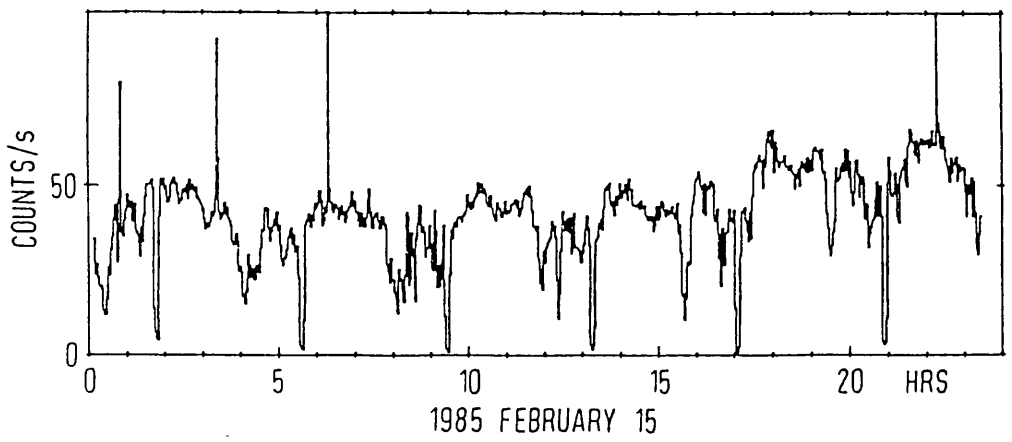

FIGURE 1.3: X-ray light curve of EXO 0748–676 showing the regular eclipses and more variable dipping behaviour. Note also the frequent sharp 'bursts' arising from thermonuclear ignitions of accreted material. From Parmar *et al.* (1986).

thought that LMXB contain thick accretion discs which, when seen edge on, can hide the central X-ray source (Milgrom 1978). Those LMXB which are seen at high inclination provide direct evidence of thick discs and are the source of much of our knowledge of disc structure. Material in the accretion flow may interpose in the line of sight to the central X-ray source, and partially absorb the X-ray flux, producing highly erratic 'dipping' activity. As an example, I show in Fig. 1.3 an X-ray light curve of the source EXO 0748–676. Periodic, deep eclipses occur when the secondary blocks the X-ray flux while in addition there are recurrent, shallower, highly variable dips. The dips are deepest at lowest energies, confirming that they are caused by photo-electric absorption.

In the dipping sources it is difficult to determine the disc structure due to the point source nature of the X-rays. The light curve of EXO 0748–676 shows, though, that not all of the X-rays act as a point source. At mid eclipse there remains a residual flux of 4% of the uneclipsed level. This is thought to be X-rays scattered from an extended hot corona surrounding the central neutron star. This ties in with the 'accretion disc corona' (ADC) sources of which X 1822–371 is proto-typical. X 1822–371 is an eclipsing LMXB with a unusually low L_x/L_{opt} ratio (~ 20) and a smooth, almost sinusoidal X-ray light curve. Here the direct line to the primary is entirely obscured and we see only the X-rays scattered by the corona. The corona acts as an extended X-ray source against which the disc is projected. Variations in the disc alter the proportion of the corona that is visible and so produce a smooth modulation of the X-ray flux — a situation which provides an excellent diagnostic of accretion disc structure, exploited in Chapter 5.

There is no evidence that the LMXB exhibiting dipping or ADC behaviour are intrin-

sically different from other LMXB (their period distributions, for instance, are similar). Thus it is possible to construct a unified model of LMXB in which those seen at low inclination (face on) show no orbital periodicity while at higher inclinations dipping activity occurs and when edge on, an ADC source is seen. For a fuller account of X-ray orbital variations in LMXB see Parmar & White (1988) and White (1989).

Appendix

1.A The binary orbit

I consider here the situation of a higher mass compact star (denoted by the subscript 1) and a lower mass star which fills its Roche-lobe (denoted by the subscript 2) in orbit around their common centre of mass with a separation, a.

Spectral lines emitted by either star will be Doppler shifted and, for a circular orbit, undergo a sinusoidal modulation in velocity with the orbital period P. The observed amplitude of this variation, when viewed at an inclination, i, is,

$$K_{1,2} = \frac{2\pi}{P} a_{1,2} \sin i$$

where $a_{1,2}$ denotes the star's distance from the center of mass.
Now, Kepler's Third Law states that,

$$\frac{G(M_1 + M_2)}{a^3} = \left(\frac{2\pi}{P}\right)^2,$$

where M is the star's mass, and as,

$$a = \frac{M_1 + M_2}{M_2} . a_1,$$

we have,

$$\frac{(M_{2,1} \sin i)^3}{(M_1 + M_2)^2} = \frac{P K_{1,2}^3}{2\pi G}.$$

The quantity on the right is a function of the observables P and K only. The quantity on the left is termed the 'mass function'. If both K_1 and K_2 are measured (see below) then the mass ratio, $q = M_2/M_1$, is known and the individual masses are a function of the inclination alone. If, further, the inclination can be deduced from the light curves (eclipse profiles for instance) then the binary masses and geometry are fully determined. This, however, is a rare situation in the study of compact binaries.

More likely only one or neither of K_1 and K_2 can be measured. It is then necessary to make additional assumptions. If the lower mass star fills its Roche-lobe then its radius

is a function of the mass ratio and binary separation only. Eggleton (1983) approximates the volume averaged Roche-lobe radius with the expression,

$$R_L = a.\frac{0.49q^{2/3}}{0.6q^{2/3} + \ln(1+q^{2/3})}.$$

Now the radius and mass of a star are related by its internal structure. It is usually assumed that the low mass stars in compact binaries are on the Zero Age Main Sequence — although this is only for want of a better calibration and is frequently questioned. Patterson (1984) provides the empirical lower-ZAMS calibration,

$$R/R_\odot \sim (M/M_\odot)^{0.88}$$

and hence, using the Roche geometry,

$$M_2/M_\odot = 0.380P_4^{1.220}, \qquad \text{where } P_4 \text{ is } P/(4 \text{ hr}).$$

With the use of this formula and the measurement of either K_1 or K_2, the binary geometry is determined as a function of inclination only.

In the situation where neither K_1 or K_2 are known it is necessary to fall back on more general arguments to constrain the mass of the compact star. A white dwarf is limited to $M \leq 1.4M_\odot$ (Chandrasekhar's limit) while a neutron star can be as massive as $\sim 3\,\mathrm{M}_\odot$ (depending on the equation of state). Additional information may be deduced from the Doppler broadening of spectral lines and the velocity amplitudes of S-wave features in the spectrum. By assuming that the matter is in a Keplerian orbit or in free-fall, a knowledge of the distance of the material from the compact star yields information about the star's mass and the inclination.

Measuring K_1

The prominent emission lines in the spectra of cataclysmic variables arise in the accretion flow around the compact star. If this accretion flow is axi-symmetric, then the mean velocity of the emission lines will equal that of the compact star and thus its orbital variation, K_1, can be measured. In general, though, the accretion flow is not axi-symmetric. The largest asymmetry is normally that caused by the impact of the accretion stream from the secondary with the edge of the disc; this produces a region of enhanced line emission and hence an S-wave feature in time-resolved spectra. This feature resides at the edge of the disc and usually reflects the Keplerian velocity at this radius. It is therefore sometimes possible to circumvent its effect by measuring the velocity only of the higher velocity line wings which originate closer to the compact star — provided the disc here

is axi-symmetric. A common method is to measure the emission line velocity by fitting the profile with a Gaussian or Lorentz function while assigning zero weight to the central regions of the profile. Alternatively a technique suggested by Schneider & Young (1980) and developed by Shafter (1985) cross-correlates the line profile with a template consisting of pair of Gaussians separated by an amount comparable to the line width — thus being sensitive only to the line wings. With both techniques more of the central regions of the line are progressively excluded until the statistical quality of the result decreases unacceptably. This ensures that the measurement is most sensitive to the highest velocity regions nearest the compact star which are most likely to take on the orbital velocity of that star.

Measuring K_2

The secondary in cataclysmic variables is typically an M-dwarf. It is therefore most easily seen by looking in the red part of the spectrum where the fractional contribution from the blue accretion disc and compact star is least. Measurement of the orbital velocity of the secondary can be achieved using the narrow absorption doublet, Na I $\lambda\lambda$8183, 8195 Å, which is prominent in the spectra of M-dwarfs. This technique has proved successful when applied to polars (Mukai & Charles 1987) and has recently been extended to many other CVs (Friend *et al.* 1988). Unfortunately similar attempts with the intermediate polars have so far failed to convincingly detect the Na I doublet (Mukai, private communication).

CHAPTER 2

Spectroscopy of EX Hydrae

2.1 Introduction

EX Hydrae is an intermediate polar with an orbital period of 98 mins and a white dwarf spin period of 67 mins. EX Hya is the only known member of the class in which eclipses of X-ray emission are observed, a factor which makes it particularly suitable for studying the geometry of the accretion process in such a star. It is also the intermediate polar in which the white dwarf rotation period and the orbital period are most nearly equal and, with SW UMa (Shafter, Szkody & Thorstensen 1986), is one of only two known intermediate polars with an orbital period below the 2–3 hour CV period gap.

EX Hya is a $13^{\rm th}$ magnitude optical star, and an X-ray source with a flux of 4 μJy in the 2-11 keV range. Its optical variability has been studied recently by Vogt, Krzeminski & Sterken 1980, Warner & McGraw 1981, Gilliland 1982, Sterken *et al.* 1983, Córdova, Mason & Kahn 1985 (hereafter CMK), and Jablonski & Busko 1985. The X-ray emission of the star has been examined by Kruszewski *et al.* 1981, CMK, Beuermann & Osborne 1985, and Rosen, Mason & Córdova 1988. In both the optical and X-ray bands the radiation is modulated almost sinusoidally with the 67-min white dwarf rotation period; the pulse fraction is 15% in the optical band, and is about 30% in the X-ray band at 1 keV, decreasing to zero above about 6 keV. The X-ray and optical modulations are in phase. A narrow, partial eclipse of the optical and X-ray emission recurs every 98 mins and is interpreted as an occultation of the white dwarf star and its environs by the mass-donating companion. Jablonski & Busko (1985) found that the time of the optical eclipse moves back and forth depending on the phase in the 67-min cycle at which it occurs. The full amplitude of the variation is ~ 70 seconds, implying that the center of eclipsed light moves by about $\pm 2 \times 10^9$ cm. The eclipse is earliest at $\phi_{67} = 0.75$. The depth of the eclipse in the X-ray band depends on energy, being most pronounced above 3 keV (Rosen, Mason & Córdova 1988). The lowest energy X-rays also (E < 2 keV) show a broad dip every orbital cycle, centered around phase 0.9 with respect to the narrow eclipse (CMK).

This chapter describes time-resolved optical spectroscopy of EX Hya. The principal optical spectroscopic features of the star are broad hydrogen emission lines, showing double-peaked structure and a superimposed S-wave, together with weaker He I and He II emission. Spectral studies of EX Hya have been published previously by Breysacher & Vogt 1980 (BV); Cowley, Hutchings & Crampton 1981 (CHC) and Gilliland 1982, but the results have not always been in agreement. Gilliland confirmed BV's detection of equivalent width variations on the 67-min cycle although CHC saw no clear evidence for them. Gilliland gave a radial velocity half-amplitude $K_1 = 58 \pm 9\,\mathrm{km\,s^{-1}}$ whereas BV found $K_1 = 68 \pm 9$ and CHC $K_1 = 90 \pm 28$. CHC saw rapid V/R line changes near eclipse but these were not confirmed by Gilliland. Gilliland did, however, report a variation on a new period of half the 67-min cycle. The present study, the most extensive to date, was undertaken in an attempt to resolve these issues and to further investigate the accretion geometry in this object.

2.2 Observations

The data were obtained in the interval 1983 March 9^{th}–22^{th} at the South African Astronomical Observatory using the 1.9-m telescope with the two detector (A,B) Reticon Photon Counting System. The star was recorded in detector B while the background was monitored with detector A. Wavelength calibration was provided by regular exposures of Cu/Ar arc spectra and flux calibration was obtained from spectra of the standard star LTT4816 and data published by Stone & Baldwin (1983).

A total of 1083 spectra were taken at a dispersion of 0.65 Å per channel; 90% were integrated for 30 seconds, the rest integrated for 60 seconds. The useful wavelength range was 4200–5050 Å and the resolution was ~ 1 Å. The observations were made in relatively poor observing conditions when the primary programme on fainter objects was not feasible. As a result the absolute flux level in the individual spectra is unreliable and all spectral analysis has been done relative to the continuum. In the same two week interval during which spectroscopic observations of EX Hya were made with the 1.9-m telescope, B-band CCD photometry of the star was obtained with the SAAO 1-m telescope. Both EX Hya and a nearby star were imaged simultaneously to provide accurate relative magnitudes for the variable despite the poor conditions. By reference to the CCD photometry, which is discussed at greater length by CMK, the mean variation in the lines can be separated from that of the continuum.

All observation times were converted to Ephemeris Time. In analysing the data I have adopted Gilliland's quadratic ephemeris for the 67-min cycle. The B-band photometry

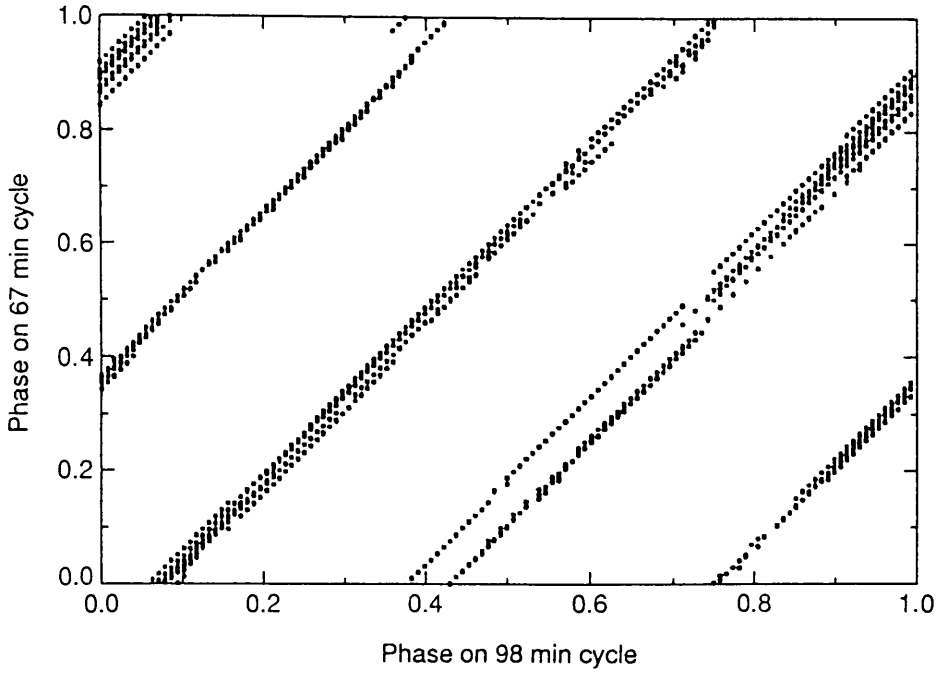

FIGURE 2.1: Each 30-sec spectral observation of EX Hya is plotted according to its phase on the 67- and 98-min cycles. The incomplete phase-space coverage complicates deconvolution of the orbital and spin periods.

(CMK) shows that the 67-min optical maxima (defined as the peak of the best fitting sinusoid) occurred 1.2 mins (0.018 cycles) later than the predicted times. The pulse profile in the data is asymmetric, however, so changes in the shape of the pulse may account for the discrepancy. As the long term behaviour of the 98-min orbital cycle is unclear (Jablonski & Busko 1985) I have used Mumford's (1967) linear ephemeris which predicts eclipse times which are coincident with the observed eclipses to within the time resolution of the data.

EX Hya presents peculiar difficulties in that the 67-min period is only 2% different from two thirds of the orbital period while both periods are nearly commensurate with one day. A given phase in the 67-min cycle will recur to within 3.3% of the same U. T. every 2 days, while the 98-min cycle repeats with similar accuracy every 3 days. This means that the 2 week observing run does not uniformly fill the phase space between these periods (see Fig. 2.1) complicating the interpretation of the data. Presumably all previously published data will be similarly affected.

2.3 Analysis

The phase averaged spectrum of EX Hya derived from the data is shown in Fig. 2.2. Prominent in the wavelength range covered are the Balmer lines, Hβ and Hγ and also

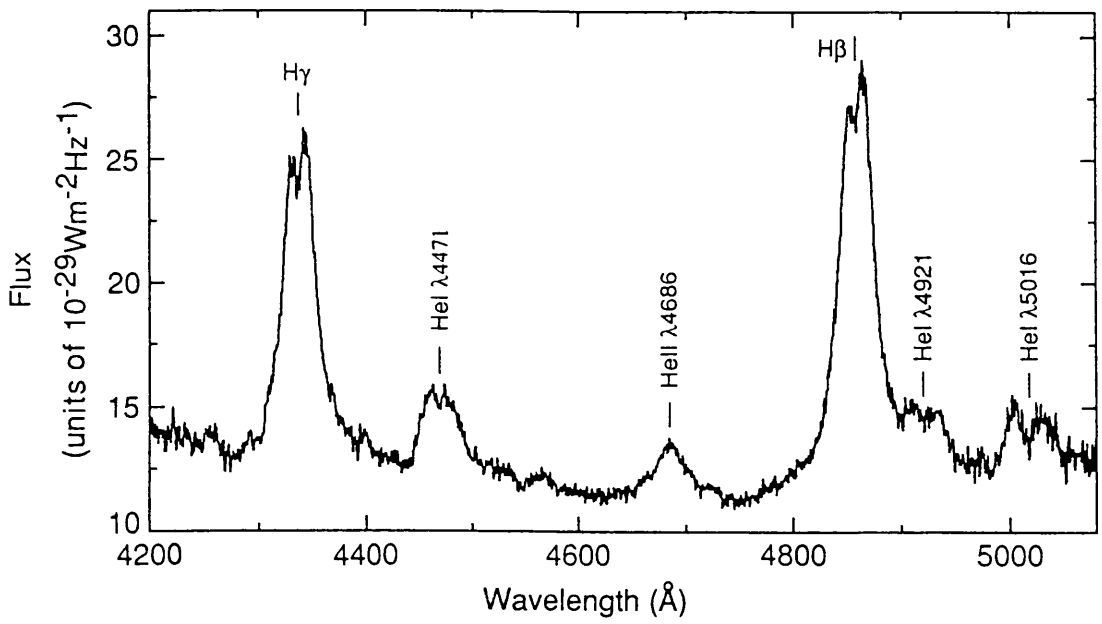

FIGURE 2.2: The phase averaged spectrum of EX Hya. Owing to the poor observing conditions the absolute flux calibration is unreliable.

He I λ 4471 and He II λ 4686. All the lines are broad, with a full-width at base of order 7000 km s^{-1}. The Balmer and He I lines have a double peaked profile while the He II λ 4686 line is single peaked, clearly different from the others.

2.3.1 · PERIODIC VARIATION OF THE EMISSION LINES

To examine how the gross properties of the lines vary with time I have calculated their equivalent width and V/R ratio in each spectrum. Power spectrum analysis was used to search for periodic variability in these quantities. The V/R ratio was determined by dividing each line about the centroid wavelength, calculating the equivalent widths of the red and violet halves separately and taking the ratio of these values.

Equivalent widths

The power spectrum of the Hβ equivalent width data is shown in Fig 2.3. There is a strong peak at a frequency corresponding to the 67-min period, as reported by Gilliland and BV, along with a retinue of window peaks caused primarily by the diurnal sampling. The inset to the figure shows, for comparison, the power spectrum of a pure 67-min sinusoid sampled in the same way as the data. There is no evidence of significant power at other frequencies, in particular at the 46.4-min optical photometry period reported by CMK and the 33.6-($\frac{1}{2}$67) min period reported by Gilliland.

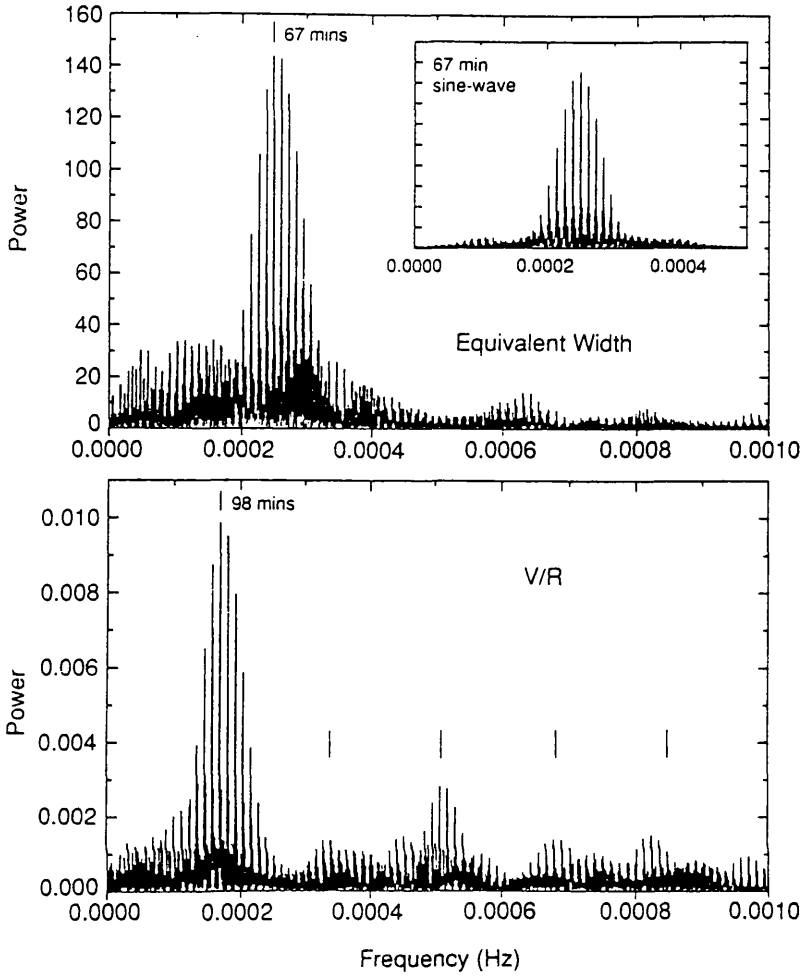

FIGURE 2.3: Power spectrum of the equivalent widths (upper panel) and V/R data (lower panel) for the Hβ line. The window function, caused primarily by diurnal sampling, is illustrated by the inset which shows the power spectrum of a pure sinusoid sampled in the same way as the data. The tick marks in the V/R plot correspond to the harmonics of the 98-min period.

The equivalent widths of each line, folded on the 67-min period, are shown in Fig. 2.4 and the parameters of the sinusoids that best fit the data are given in Table 2.1. The maximum in each line occurs at phase 1.00 ± 0.01 (1σ), consistent with the peak of the B-band 67-min variation which is measured to be at phase 1.02 ± 0.01. This result contrasts with that of Gilliland (1982) who found that the equivalent width of the lines peaked at phase 0.91. Since the variation in line equivalent width is in phase with that of the continuum, the line *flux* is modulated by more than the continuum. The fractional variation in equivalent width varies significantly from line to line, being greatest for He I λ4471 (pulse fraction 0.35 ± 0.04), and least for He II λ4686 (pulse fraction 0.09 ± 0.06). The pulse fraction of the B-band continuum measured from the CCD photometry is $15 \pm 1\%$,

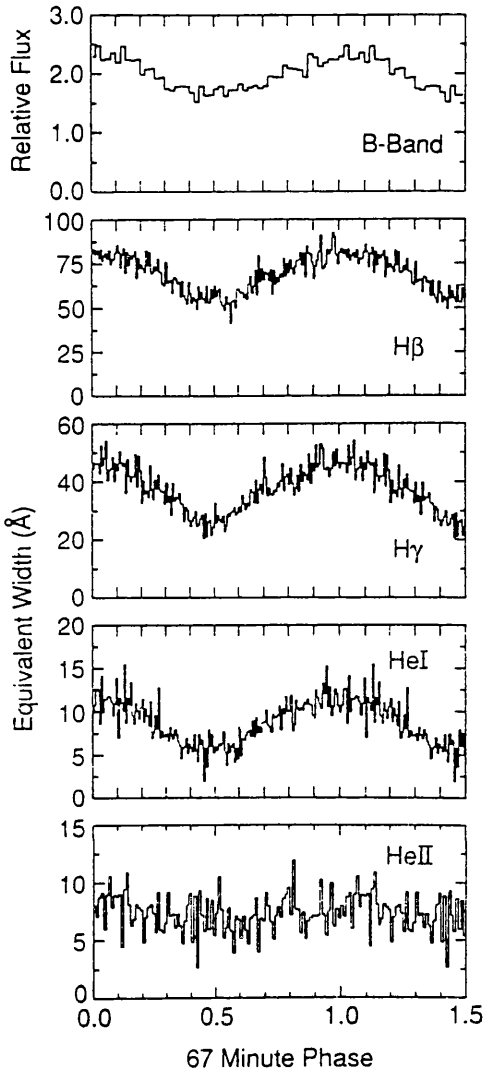

FIGURE 2.4: Equivalent widths of the spectral lines of EX Hya folded on the 67-min cycle together with the B-band photometric data (top panel). The ephemeris used is that of Gilliland (1982); ET= $2,437,699.8900 + 0.046546549\,E - 1.05 \times 10^{-12}E^2$ (E = cycle no.).

implying that the pulse fractions of the $\lambda 4471$ and $\lambda 4686$ line fluxes are 0.48 ± 0.05 and 0.24 ± 0.07 respectively.

V/R ratio

A power spectrum of the V/R data (Fig. 2.3) shows a system of peaks corresponding to a period of 98-mins, together with the 1^{st}, 2^{nd}, 3^{th} and possibly 4^{th} harmonics of this period. The V/R data for the Hβ line are shown folded on the 98-min period in Fig. 2.5. Also plotted in this figure are the total equivalent width of the line, the equivalent width

TABLE 2.1: Equivalent width modulations with the 67-min cycle.

Line	Mean (Å)	Half-Amp. (Å)	Pulse Fraction	ϕ_{max}
Hβ	67.6 ± 0.4	12.2 ± 0.7	0.18 ± 0.01	1.01
Hγ	37.0 ± 0.4	9.1 ± 0.5	0.25 ± 0.01	1.00
He I	8.6 ± 0.2	3.0 ± 0.3	0.35 ± 0.04	0.99
He II	7.1 ± 0.3	0.6 ± 0.4	0.09 ± 0.06	1.02

of the V and R halves separately, and the B-band photometry, all folded on the 98-min period. Because there is a strong modulation of the equivalent width at the 67-min period, as discussed above, and because the 67-min and 98-min cycles are nearly commensurate, a sinusoid with the parameters of the 67-min cycle was subtracted from the equivalent width data before they were folded on the 98-min period.

The total equivalent width of the line shows little modulation with the 98-min cycle, in agreement with the results of the power spectrum analysis (Fig. 2.3). However there is a significant sharp peak in the total equivalent width, and also in the equivalent widths of the separate V and R components (Fig. 2.5), exactly coincident with the narrow, B-band-continuum eclipse at phase 0.0. The magnitude of the peak in the equivalent width is consistent with there being no narrow eclipse of the emission line flux.

The folded V/R data show an approximately sinusoidal variation with the 98-min period except for a region approximately a tenth of a cycle either side of the B-band eclipse (phase 0.0) where significant deviations from the best fit sinusoid occur. Fitting a sine-wave to this variation, excluding the eclipse region (phase 0.8–1.2), yields an amplitude of 0.07 ± 0.02 for the Hβ line and 0.04 ± 0.02 for the Hγ line with mean offsets of 0.85 ± 0.02 and 0.87 ± 0.02 respectively. In both lines the maximum of the sine wave occurs at phase 0.61 ± 0.05.

The sinusoidal variation in V/R is, as demonstrated in Section 2.3, caused by an *S*-wave feature in the line. However, between phase $\sim$ 0.9 and phase 0.0 there is a progressive reduction in the V/R ratio below the best fit sinusoid. The trend reverses rapidly at the time of B-band eclipse, and between phase 0.0 and $\sim$ 0.1 there is an excess in the V/R ratio compared to the best fit sinusoid. This 'eclipse effect' in the V/R curve is the cause of the harmonic structure in the power spectrum of the data. I interpret the effect as an

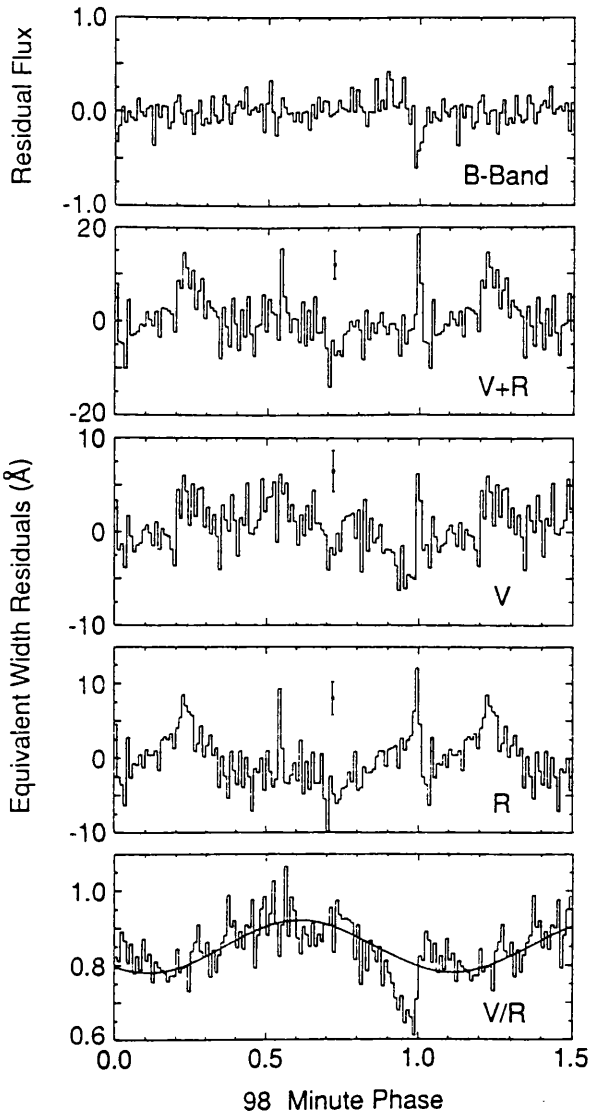

FIGURE 2.5: Orbital cycle variations; from top to bottom: B-band data; equivalent width of the Hβ line; equivalent width of the violet (V) side of the Hβ line; equivalent width of the red (R) side of the Hβ line; V/R ratio for the Hβ line. The best fit sinusoid (Section 2.3.1) is shown superimposed on the V/R data. In all cases the 67-min variation has been subtracted out before folding on the orbital cycle. Ephemeris; $T_{min} = JED_{\odot} 2\,437\,699.94179 + 0.068233846\,E$ (Jablonski & Busko (1985)).

occultation, by the companion star, of a mass-flow circulating around the white dwarf. The companion obscures the approaching half of the flow before phase 0.0, and the receding half after phase 0.0. Inspection of the separate plots of V and R equivalent width confirms that there is a deficit in the V half of the line before phase 0.0, and a deficit in the R half after phase 0.0. A similar 'eclipse effect' or 'rotational disturbance' has been seen in other

eclipsing cataclysmic binaries, e.g. DQ Her (Young & Schneider 1980; Greenstein & Kraft 1959), HT Cas (Young, Schneider & Shectman 1981) and Z Cha (Marsh, Horne & Shipman 1987), and is usually taken to be indicative of an accretion disc.

An eclipse effect in the V/R data of EX Hya was also reported by CHC, although in much sparser measurements. Gilliland (1982) did not interpret his data in this way, although I believe his data to be consistent with the effect. Instead Gilliland interpreted the residuals from the mean sinusoidal variation in V/R in terms of another periodic variation at 33.6-mins (i.e. $\frac{1}{2}67$ mins). The amplitude of the 98-min and the 33.6-min variations he measured to be 0.094 and 0.052 respectively, the eclipse effect contributing to the amplitude of the 33.6-min variation.

My data are more extensive than those of Gilliland, and the eclipse effect measured cannot be fit in a satisfactory manner by a sinusoid with a 33.6-min period — the variation is clearly not sinusoidal and Gilliland's interpretation does not explain the deficits in the individual V and R equivalent width plots that make up the effect. I have nevertheless searched for other evidence of a 33.6-min period in my data. Such a periodicity would be obscured in the power spectrum of all the V/R data (Fig. 2.3) because it is coincident with a window peak of the much stronger second harmonic of the 98-min variation (a consequence of the near commensurability of the 67-min and 98-min periods with one day). Instead I constructed the power spectrum of the V/R residuals from the best fit 98-min sine-wave, after excluding all data within a phase interval of 0.2 either side of eclipse. There are no significant peaks in the resulting spectrum whilst the noise level near the 33.6-min period corresponds to an amplitude of ~ 0.01. To confirm this I folded the residuals on the 33.6-min period. The best fit sine wave to the folded data had an amplitude of 0.011 ± 0.017 (1σ). My results are therefore consistent with no modulation at 33.6- ($\frac{1}{2}67$) mins, while a variation at the level reported by Gilliland can be excluded with 95% confidence.

2.3.2 Line profile variations

To examine the variation of the line profiles in more detail, I normalize each line spectrum to the continuum and compute the average spectrum in each of 20 phase-bins for both the 67-min and 98-min periods. Fig. 2.6 displays the result for the Balmer lines, Hβ and Hγ, in the form of a grey scale intensity plot as a function of phase and wavelength. In Fig. 2.7 (a,b) the data for the Hβ line are displayed again as an intensity profile versus wavelength for each phase bin.

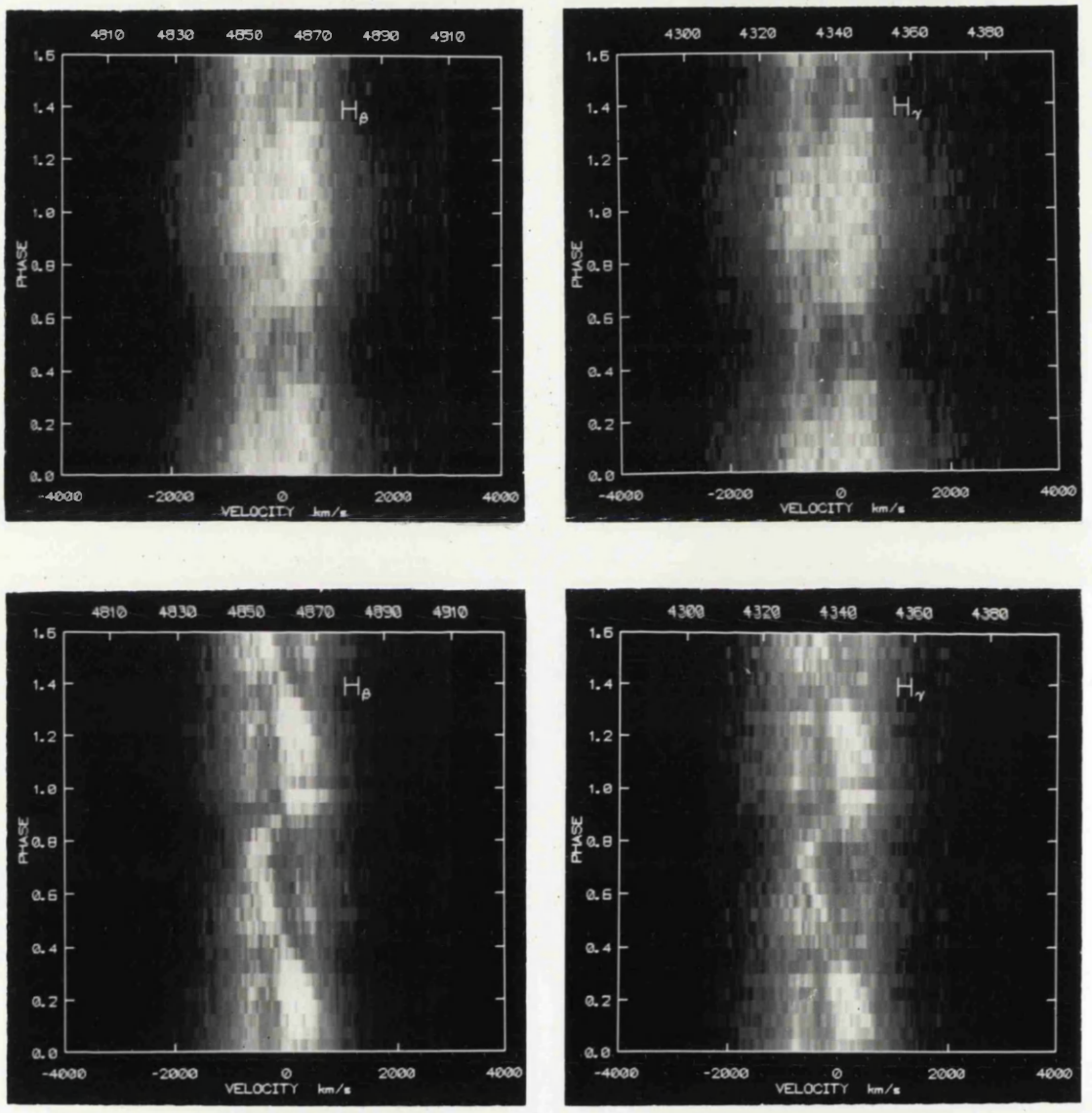

FIGURE 2.6: Hβ and Hγ line profile variations displayed in a grey-scale intensity plot as a function of wavelength (velocity) and phase on both the 98- and 67-min cycles.

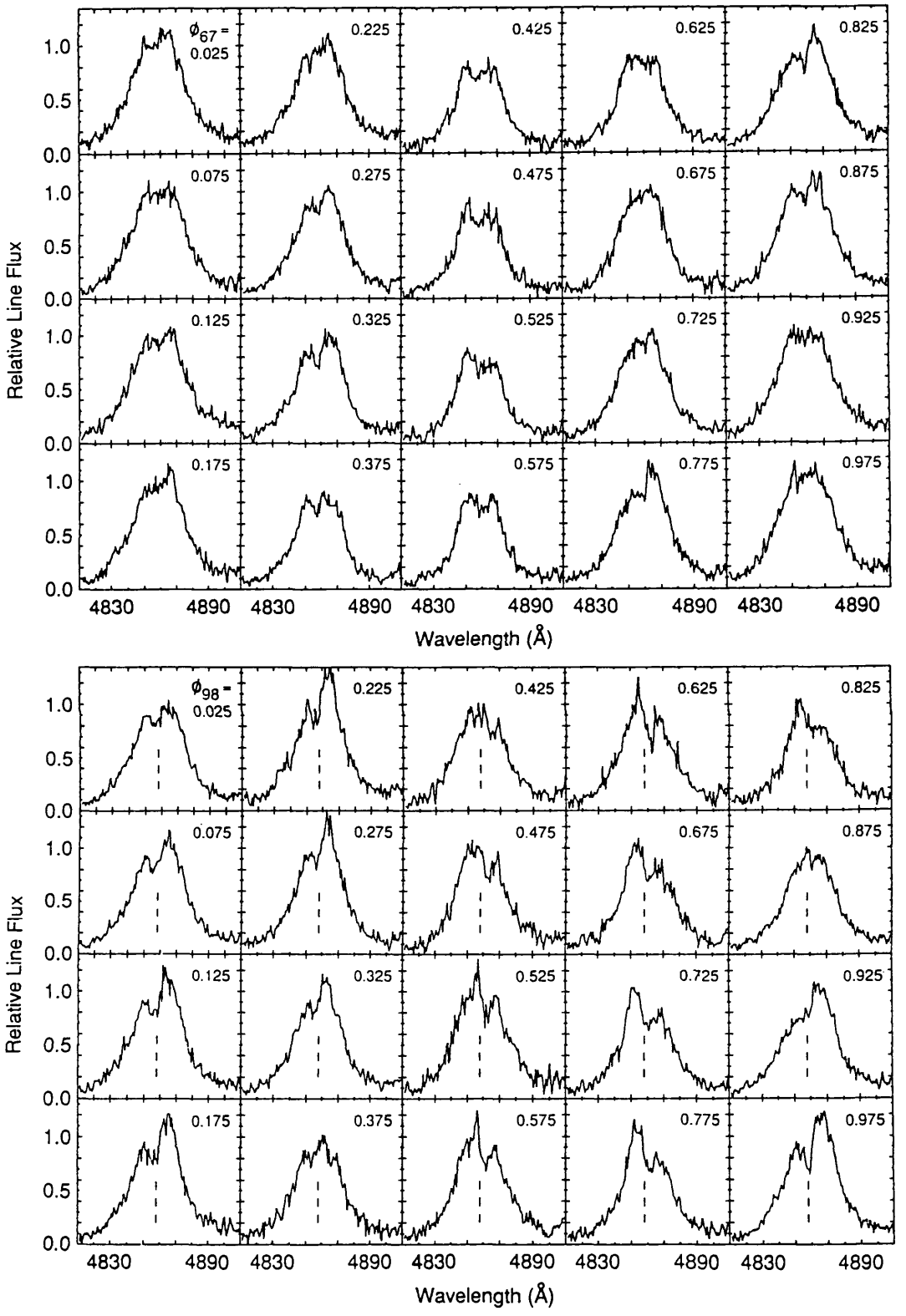

FIGURE 2.7: Hβ line profile changes — the same data as in Fig. 2.6 plotted to show intensity against wavelength for each phase-bin. The data have been normalized to the continuum so that zero corresponds to the continuum level and one to twice the continuum level. The upper panel shows the 67-min cycle variations and the lower panel variations on the orbital cycle.

67-min cycle

The grey-scale plot shows clearly the double peaked nature of the Balmer lines, and the marked variation in their strength as a function of 67-min phase. The relative strength of the violet and red peaks appears to change with phase. However I believe this apparent effect is caused by contamination from the orbital (98-min) cycle S-wave. The S-wave is brightest and reddest at phase $\phi_{98} \sim 0.2$ which, as can be seen from Fig. 2.1, occurs on the 67-min cycle at phases $\phi_{67} \sim 0.2$ and 0.7 in the data. These are the 67-min phases where the red peak appears to be stronger than the blue peak in Fig. 2.6. I have tested this conclusion quantitatively by generating a pseudo-dataset in which each individual spectrum was replaced by the folded spectrum with the appropriate value of the 98-min phase. The pseudo-data were then folded on the 67-min cycle in exactly the same way as the real data. The resulting grey-scale plot showed changes in the relative brightness of the V and R peaks which were indistinguishable from those in the real data. Thus there is no evidence that there are large intrinsic changes in the relative height of the V and R peaks with the 67-min cycle, confirming the power spectrum analysis of the V/R ratio discussed in Section 2.3.1 (but see Section 2.3.2).

The most striking aspect of the grey-scale plot, confirmed by the detailed line profiles in Fig. 2.7, is the marked variation in the width of the lines with 67-min phase. This implies that the wings of the lines are modulated more strongly than the core. To verify this I have calculated the equivalent widths of the core and wing regions of the lines separately. The variation is sinusoidal in both cases, but the pulse fractions differ. For the Hβ line the pulse fraction of the equivalent width variation for absolute velocities less than 1000 km s^{-1} is 0.14 ± 0.03 whereas for velocities greater than 1000 km s^{-1} it is 0.25 ± 0.04. For the Hγ line the values are 0.21 ± 0.03 and 0.34 ± 0.05 respectively.

To examine the profile of the modulated part of the line, I have computed the mean spectrum for the maximum and minimum of the 67-min cycle (phases 0.75–1.25 and 0.25–0.75 respectively) and subtracted them. The difference is the relative spectral distribution of the pulsed component of the emission, and this is shown in Fig. 2.8. The pulsed emission is clearly broad, the Hβ line having a FWHM of 60 Å compared to a value of 39 Å in the 'total' spectrum. The lines in the 'pulsed' spectrum are also significantly less double-peaked than the 'total'. The structure that there is in the profile of the pulsed emission can be accounted for by contamination from the 98-min S-wave (see Section 2.3.2). I have corrected for the gross effects of the S-wave in a manner similar to that described earlier in this section, by constructing a pseudo-dataset based on the mean spectra phase folded on the 98-min period. The inset profiles in the lower panel of Fig. 2.8 shows the

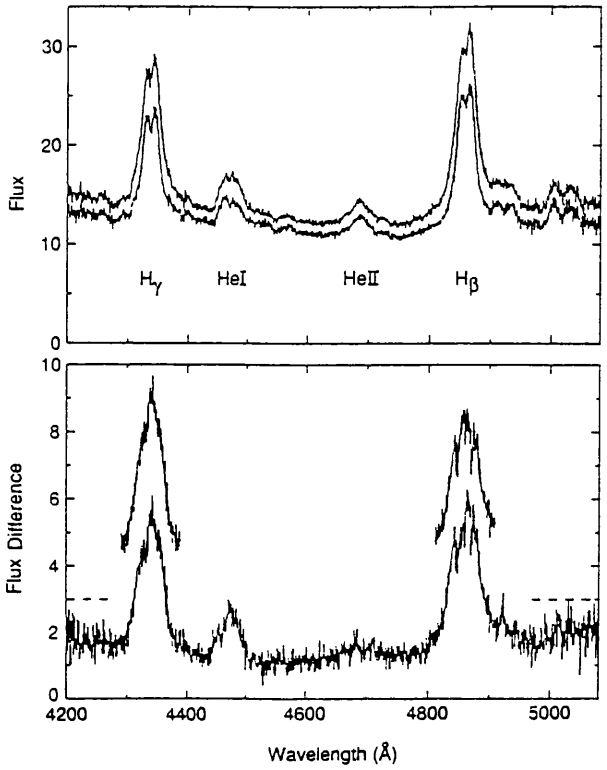

FIGURE 2.8: Modulated emission component. The upper panel shows the spectrum averaged over the brighter half of the 67-min cycle (ϕ_{67} = 0.75–1.25) together with the mean spectrum from the fainter half (ϕ_{67} = 0.25–0.75). The lower panel shows the difference between the upper curves *i.e.* the relative flux distribution in the modulated component of the emission. The raised line profiles in the lower panel show the modulated component after correcting for the orbital *S*-wave contamination (see Section 2.3.2); for clarity these profiles are offset by 3 flux units.

effect of applying this correction to the lines. The corrected profiles are significantly more symmetric than the original. Thus a consistent interpretation of the data is that the emission lines in EX Hya are made up of a steady, double-peaked component together with a broad component whose flux is modulated with the 67-min cycle.

In determining the accretion geometry it is crucial to know where in the system the modulated component originates. In principle, analysis of the magnitude of the V/R 'eclipse effect' as a function of 67-min phase could, given data of adequate statistical quality, allow us to determine the size of the region emitting this component. If the region is point-like then there will be no eclipse effect in the modulated component and one would expect to see a reduction in the magnitude of the eclipse effect near 67 cycle maximum compared with that near 67 cycle minimum (by $\sim$ 25%). A reduction in the amplitude of the eclipse effect by this amount is only marginally consistent with the data, suggesting

that the broad line emitting region is not point-like. This is consistent with the absence of any detectable narrow eclipse in the lines (Section 2.3.1).

The He I λ4471 line shows variations similar to the Balmer lines, as far as can be judged given its much poorer statistical quality. The He II λ4686 line shows a slight intensity enhancement at phase $\sim$ 0.0, in agreement with the results in Table 2.1, but no other detectable structure or variation.

Profile variations of the line wings

In Section 2.3.1 I examined the variability of the V/R ratio in the lines in EX Hya. Given that the analysis of Section 2.3.2 indicates that the pulsed component of the lines dominates at high velocities, I have repeated the V/R ratio analysis calculating the ratio from the wings of the line only (absolute velocity > 1200 km s^{-1}) in order to have maximum sensitivity to variations in the profile of the pulsed emission. This was done for both the Hβ and Hγ lines, but the results for Hβ were not useful because of contamination of the red wing of the line by He I λ4921.

The power spectrum of V/R variations in the wings of Hγ is complicated because of the large number of window peaks associated with the diurnal sampling. However, it shows V/R modulation in the line wings at both the 67-min and 98-min periods. The 98-min variations are such that the maximum V/R occurs at phase 0.25, and this modulation is, I believe, due to orbital motion of the binary which is discussed more fully in Section 2.3.3. The data folded on the 67-min period are shown in Fig. 2.9 and are well fit by a sinusoid with an amplitude of 0.10 ± 0.02. Maximum V/R ratio occurs at phase 0.04 ± 0.03, almost coincident with the photometric maximum in the 67-min cycle.

Orbital (98-min) cycle

There are 3 peaked components visible in the Balmer lines (Figs. 2.6 & 2.7), twin peaks (violet and red) separated by ~ 1300 km s^{-1} with a mean velocity of -95 km s^{-1} and an *S*-wave component with full amplitude 1200 km s^{-1} and mean velocity -80 km s^{-1}. The *S*-wave is brightest at maximum red shift (phase 0.15) and is also enhanced at maximum blue shift (phase 0.65). It is asymmetric in that the transition from blue to red proceeds more rapidly than that from red to blue. In regions of the figure away from the *S*-wave it is clear that the strength of the violet and red peaks also changes with phase. There is an enhancement of the red peak, and probably also the violet peak, at about phase 0.5, and an enhancement of the violet peak at phase 0.25. Some of this modulation in the equivalent width of the features may be due to the $\sim$ 5% B-band variation at the 49-min

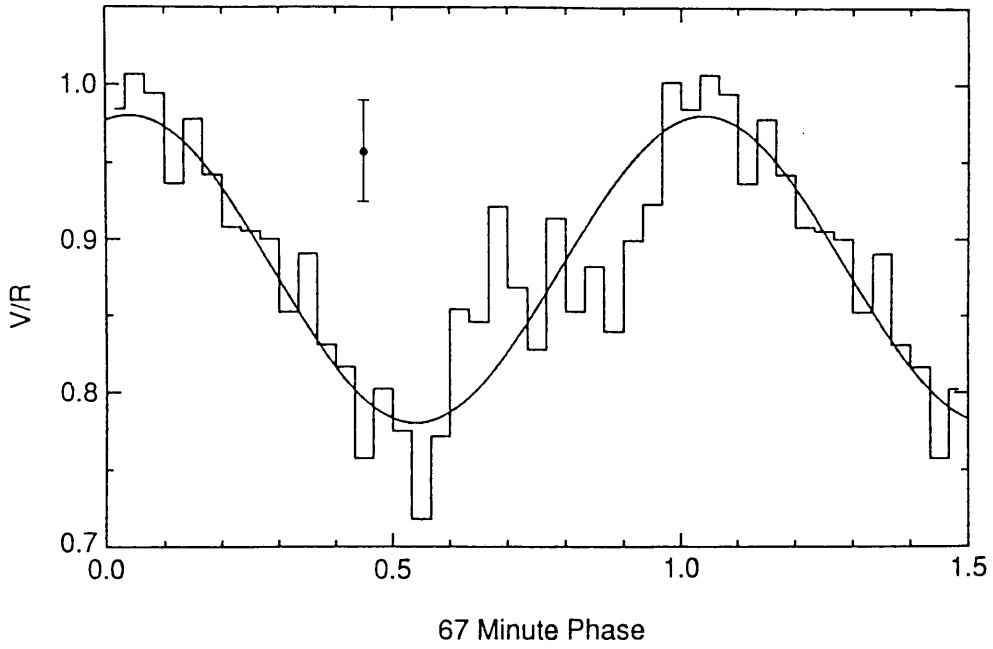

FIGURE 2.9: V/R variations of the Hγ line wings with the 67-min cycle. The mean error is shown. Line regions with velocities greater than 1200 km s^{-1} were included.

(half orbital) period reported by CMK.

There is an enhancement in the equivalent width of the lines at exactly phase 0.0 due to the narrow photometric eclipse as discussed in Section 2.3.1, although this is not properly resolved in Figs. 2.6 & 2.7. The disc eclipse which causes the 'eclipse effect' in the V/R data is clearly seen in the grey-scale plot as a fading of the blue wing around phase 0.93 followed by the partial obscuration of the red wing around phase 1.02. As is evident from Fig. 2.7b, the *S*-wave is occulted just after the narrow eclipse. The behaviour of the He I λ 4471 line appears similar to the Balmer lines in showing an *S*-wave. No such variation is detectable in the He II λ 4686 line.

2.3.3 ORBITAL RADIAL VELOCITY CURVE

The orbital radial velocity variations of the spectral lines in EX Hya were measured by fitting the phase-binned data with gaussian profiles. To minimize the effects of the *S*-wave variation it is standard procedure with cataclysmic binaries to exclude the central regions of the line during fitting. I performed the fits excluding central regions ranging from 600 km s^{-1} either side of the line center to 1600 km s^{-1} in steps of 200 km s^{-1}. At the lower end of this range the measurements gave a variation phased with maximum red-shift at $\phi_{98} = 0.93$ compared with the value $\phi_{98} = 0.75$ expected from pure orbital motion, indicating severe contamination from the *S*-wave which has maximum red-shift at

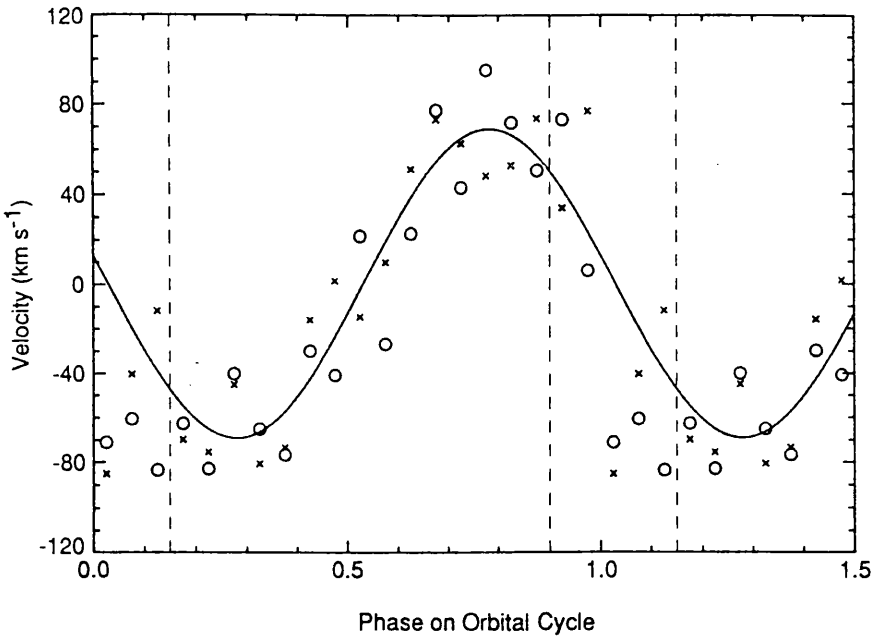

FIGURE 2.10: Radial velocity measurements. Circles represent measurements of the Hβ line and crosses those of the Hγ line. γ velocities have been subtracted from each line separately. The region near eclipse between the dashed lines was excluded from the fitting process (Section 2.3.3). The curve is the best fit sine wave whose parameters are given in Table 2.2.

$\phi_{98} = 1.15$. As the excluded region is extended the phase of maximum redshift decreases until, when excluding to ± 1200 km s^{-1}, it is consistent with $\phi_{98} = 0.75$. At the same time the measured K_1 value rises from 60 km s^{-1} (excluding to ± 600 km s^{-1}) to near 70 km s^{-1} (excluding to ± 1200 km s^{-1}).

The measured velocities of the Balmer line wings beyond ± 1200 km s^{-1} of the line center are shown in Fig. 2.10. (The He I λ 4471 and He II λ 4686 lines are to weak to allow significant velocity variations to be detected). The variations were fit by a sinusoid with a period of 98-mins, excluding data between phases 0.90 and 1.15 where there is increased scatter caused, probably, by distortion of the line profiles by the disc eclipse (Sections 2.3.1 and 2.3.2). Similar deviations near eclipse are also present in the data of BV, CHC and Gilliland, although they are less noticeable in the latter. The results of fitting the radial velocity data are summarised in Table 2.2. There is good agreement between the orbital velocities (K_1) derived from Hβ and Hγ, yielding a mean of 69 ± 9 km s^{-1}.

TABLE 2.2: Orbital radial velocity variations.

	K_1 ($\mathrm{km\,s^{-1}}$)	γ ($\mathrm{km\,s^{-1}}$)	ϕ_o max.
Hβ	68 ± 12	-34 ± 12	0.76
Hγ	70 ± 14	-11 ± 19	0.80
He I	33 ± 36	-22 ± 20	1.03
He II	52 ± 60	$+9 \pm 35$	0.53
Hγ+β	69 ± 9	-22 ± 11	0.78 ± 0.03

Stellar masses and orbit

The existence of a narrow (1.5-min FWHM) X-ray eclipse can be used, together with the measured orbital velocity variation, to restrict the binary parameters of EX Hya. If the X-ray source is point-like and near the white-dwarf, then we have, (e.g. Rappaport & Joss (1983));

$$\sin^2 i = [1 - R_L^2]/\cos\theta_e$$

where i is the inclination, θ_e is the eclipse half-angle and R_L is the volume averaged Roche-lobe radius in units of the separation, a. Eggleton (1983) gives the approximation;

$$R_L = \frac{0.49q^{2/3}}{0.6q^{2/3} + \ln(1 + q^{2/3})}$$

where q is defined as M_2/M_1 (M_2 is the companion mass and M_1 the white dwarf mass). In addition the formula for the mass function can be rearranged to give;

$$M_2 = f(m) \times \frac{(1 + 1/q)^2}{\sin^3 i}$$

These equations combine to leave one free parameter. In Fig. 2.11 I have plotted the curves of M_1 against M_2 resulting from the mass function derived from the measured K_1 value and its errors.

To proceed further one needs to make assumptions about the nature of the secondary star. If it is a lower main-sequence dwarf filling its Roche-lobe then its mass is directly related to the orbital period. Previous authors have used Warner's (1976) calibration for a theoretical zero age main sequence (ZAMS) resulting in $M_2 = 0.187\,M_\odot$ (BV) and hence a white dwarf mass $M_1 \sim 1.4\,M_\odot$. I have employed Patterson's (1984) empirical ZAMS

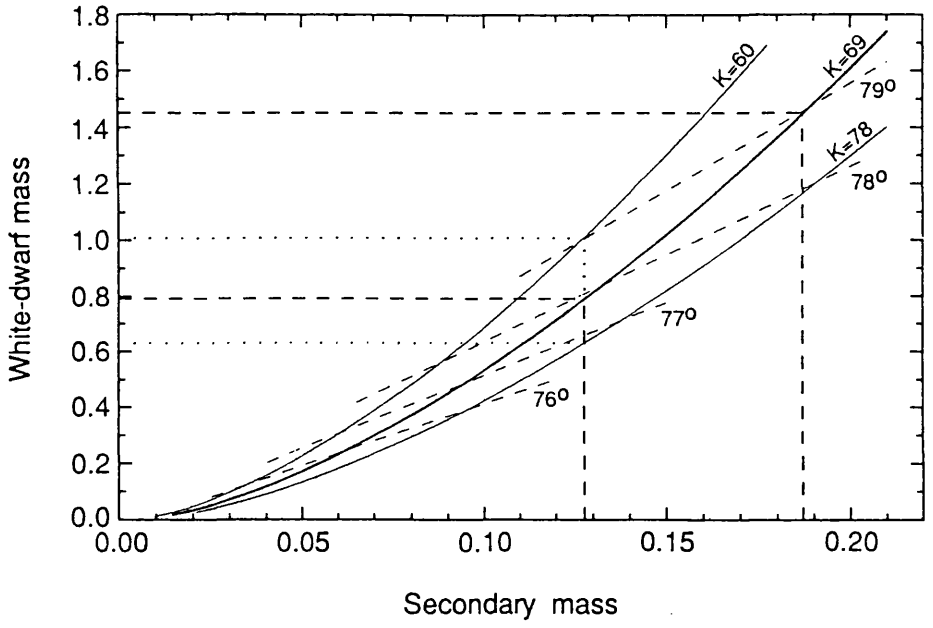

FIGURE 2.11: Masses of the component stars of EX Hya. The solid curves are the constraints derived from my measured K_1 value and its errors together with the length of the X-ray eclipse. The dashed line at a secondary mass of $0.128\,M_\odot$ results from the empirical ZAMS calibration of Patterson (1984) while the line at $0.187\,M_\odot$ results from Warner's (1976) theoretical calibration. The derived inclination contours are also shown.

calibration which gives (from his equation 7) $M_2 = 0.128\,M_\odot$. The measured range of K_1 then implies that M_1 is between $0.62\,M_\odot$ and $0.99\,M_\odot$ with the most likely value being $M_1 = 0.78\,M_\odot$ (see Fig. 2.11). The inclination is then determined to be $i = 78° \pm 1°$. Note, however, that there is large potential error in the the empirical ZAMS calibration which Patterson regards as 'quite poorly defined' in this region. Further error will result if the secondary in EX Hya has evolved significantly from the ZAMS. The derived values imply a binary separation, a, of $4.6 \pm 0.4 \times 10^{10}$ cm and a secondary Roche-lobe radius of $1.10 \pm 0.09 \times 10^{10}$ cm.

It is worth noting that the maximum measured line widths of ± 3500 km s^{-1} also constrains the mass of the white dwarf in EX Hya. A Keplerian velocity of this magnitude requires a white dwarf with a mass of at least $0.71\,M_\odot$; alternatively a free-fall velocity of this magnitude could be achieved provided the white dwarf mass were greater than $0.48\,M_\odot$.

The derived orbital parameters are summarised in Table 2.3.

TABLE 2.3: Orbital parameters of EX Hya.

Parameter	Units	Value
K_1	$km\,s^{-1}$	69 ± 9
$f(m)$	$M_\odot$	$2.3 \pm 0.9 \times 10^{-3}$
i	degrees	78 ± 1
a	cm	$4.6 \pm 0.4 \times 10^{10}$
M_1	$M_\odot$	0.78 ± 0.17
M_2	$M_\odot$	0.128
R_2	cm	$1.10 \pm 0.09 \times 10^{10}$

2.4 Discussion

The accretion geometry of an intermediate polar is potentially complicated. It is usually presumed that material leaves the secondary star through the inner Lagrangian point, forming a gas stream which feeds a disc, or torus, that is circulating around the white dwarf with Keplerian velocities. At some radius, depending on the accretion rate and the strength of the white dwarf's magnetic field, the disc is disrupted and matter attaches to the field lines to be funnelled down onto the polar regions of the white dwarf. The circulating material has access to field lines that connect with the white dwarf's surface at a range of magnetic latitudes; thus the fraction of the compact star over which accretion can occur may be large and may have a complicated shape.

With the above picture in mind, the properties of the emission lines in the spectrum of EX Hya can be interpreted. I have shown that these lines can be decomposed into three components: (i) Narrow S-wave emission whose radial velocity varies with an amplitude of $\sim 600\ km\,s^{-1}$ at the 98-min orbital period. (ii) A double-peaked component whose flux is constant and which has a peak to peak separation of $\sim 1300\ km\,s^{-1}$. (iii) A broad (FWHM $\sim 3700\ km\,s^{-1}$) line component whose flux varies as a function of the 67-min cycle. The constant, double-peaked component is readily identified with material circulating about the white dwarf, while the velocity and phasing of the S-wave component is consistent with it being due to enhanced emission in the region where the gas stream from the secondary interacts with the circulating flow. The larger width of the pulsed line component argues that this emission originates in a higher velocity region closer to the white dwarf.

2.4.1 Double-Peaked Emission

The separation of the peaks in the double-peaked line component indicates a rotation velocity of ~ 650 km s^{-1}. If this is due to Keplerian motion about the white dwarf, it implies a radial distance from that star of 2.3×10^{10} cm assuming the mass of the white dwarf to be $0.8\,M_{\odot}$ (Section 2.3.3). The base width of the un-pulsed emission is about 2500 km s^{-1}, this being measured from the Balmer lines at phase 0.5 in the 67-min cycle. Thus, again under the assumption of Keplerian motion, the un-pulsed line emission region extends inwards to about 6×10^{9} cm from the white dwarf. This may be the point at which the circulation is disrupted by the magnetic field of the white dwarf. If this were so, then this radius together with an accretion rate of $\sim 10^{16}$ g s^{-1} (CMK) would imply a white dwarf magnetic moment of $\mu \sim 7 \times 10^{31}$ G cm^3 (see e.g. King, Frank & Ritter 1985). The top panel of Fig. 2.12 is a sketch of the EX Hya system in which the various numerical constraints are illustrated.

The property that makes EX Hya particularly useful is that it is an eclipsing binary, and the eclipse by the companion can be used to probe the geometry of the accretion flow around the white dwarf. I find no evidence for a narrow eclipse in the line flux corresponding to that of the continuum, confirming that the line emission comes from an extended region. I do, however, see a more prolonged 'rotational disturbance' in the lines which is discernable for more than a tenth of an orbital cycle either side of the continuum eclipse. The 'rotational disturbance' involves a suppression of the blue wing of the line prior to phase 0.0 followed by a suppression of the red wing after phase 0.0, and is direct evidence that the line emission originates in a circulating flow.

I have modelled the V/R changes expected from the 'rotational disturbance' numerically under the assumption that the line emission comes from a uniformly emitting disc rotating with Keplerian velocities. In Fig. 2.13, I compare the expected V/R variation for such a simplified disc with the EX Hya data, using the orbital parameters for the system derived in Section 2.3.3. The simple model takes no account of the S-wave emission component or the pulsed line emission, and consequently predicts an amplitude for the eclipse effect that is about a factor of two higher than observed. In Fig. 2.13 I have arbitrarily added a constant level to both the V and R halves of the model line profile in order to match the observed data prior to phase zero. The model still does not reproduce the data after eclipse. This, I believe, is because of systematic changes in the observed intensity of the S-wave component during this time.

Because of the effects of contamination by other line emitting components, it is difficult to derive reliable quantitative information from the amplitude of the eclipse effect. One

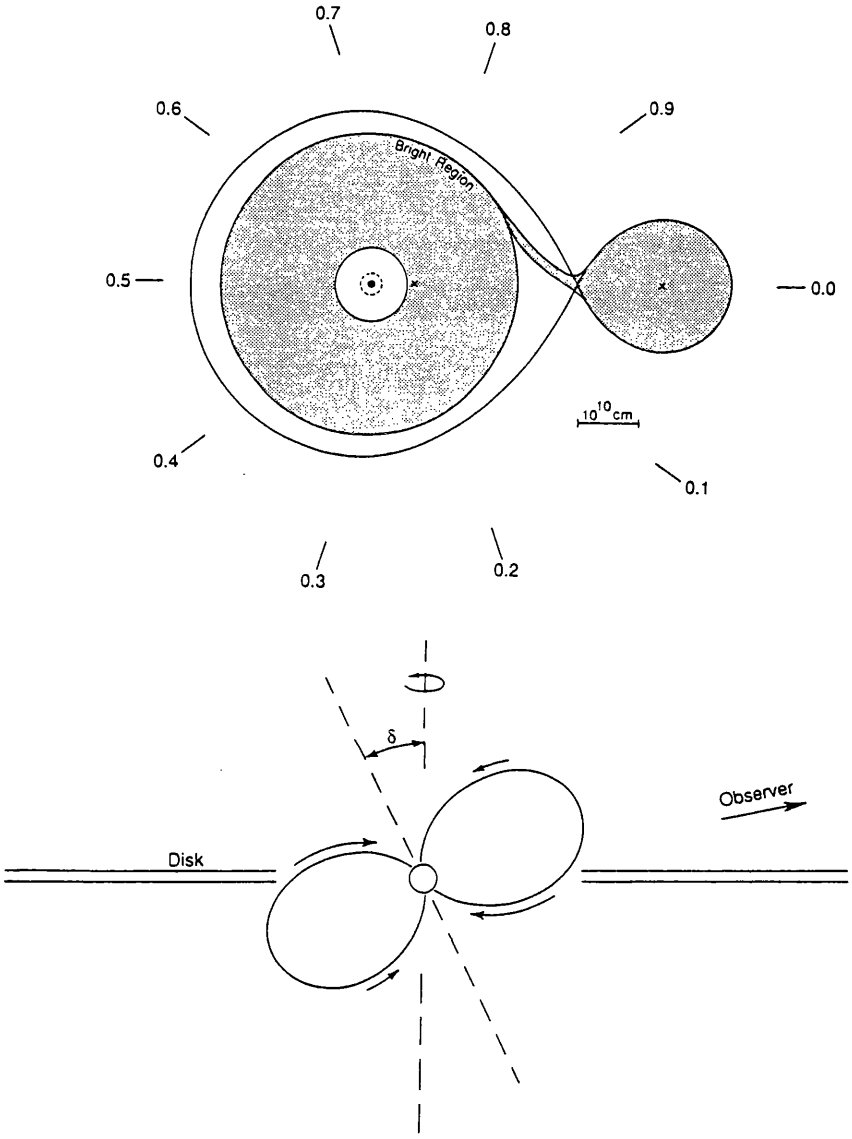

FIGURE 2.12: Schematic scale-drawing of the EX Hya binary. The upper plan view shows the relative sizes of the secondary and accretion disc. The inner edge of the disc corresponds to the minimum width of the un-modulated component of the emission lines and represents the outer limit for the Alfvén radius. The inner dotted circle marks the region over which the luminous baricenter of the system 'walks' as deduced by Jablonski & Busko (1985). The lower, side on view shows the inner regions enlarged to illustrate the geometry of the magnetic accretion onto the white-dwarf surface. The relative size of the arrows drawn next to the magnetic field lines conveys the fact that I expect the majority of matter to accrete from the side of the disc closest to the magnetic pole.

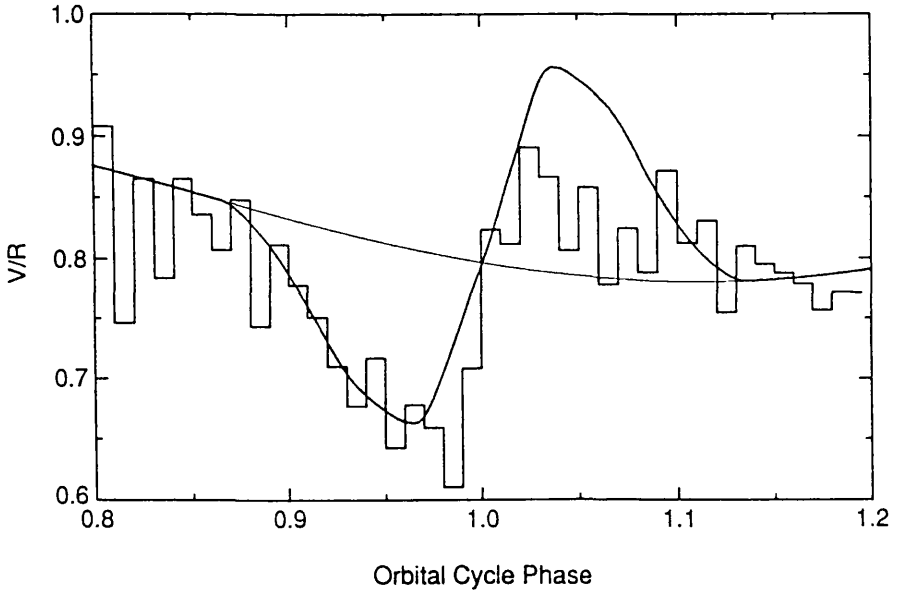

FIGURE 2.13: The Hβ V/R data around eclipse are plotted together with a simulated curve derived from a model Keplerian disc (Section 2.4.1). The discrepancies after phase 1.0 may be due to the bright spot that results from the impact of the gas stream with the outer disc.

can, though, measure the duration of the effect, and thus determine the size of the circulating line emitting region (the accretion disc). The effect extends to $\sim 0.15 \pm 0.03$ either side of phase 0.0 (i.e. a total angle of $\sim 108°$). From this angle and the orbital parameters of Section 2.3.3, the line emitting region has a maximum radius of $\sim 2.6 \times 10^{10}$ cm, in good agreement with the radius derived from the separation of the two peaks in the line profile. The line emitting accretion disc thus fills $\sim$ 80% of the white dwarf's Roche-lobe. This is illustrated in Fig. 2.12a.

2.4.2 THE S-WAVE

The data suggest that the *S*-wave emission component of the Balmer lines is eclipsed by the companion just after phase 0.0 (Fig. 2.7b). This, together with the phase and amplitude of its velocity curve, favours the interpretation of the *S*-wave component as a bright emission region near the outer edge of the circulating disc, at about phase 0.8 with respect to the companion. This is the 'standard' explanation of *S*-waves in non-magnetic CVs.

The *S*-wave in EX Hya has an asymmetric velocity curve, while its intensity varies around the orbital cycle. The sense of the velocity asymmetry is such that the transition

from blue to red, between phase 0.7 and 1.05, is more rapid than that between red and blue. The intensity of the S-wave is greatest between phase 0.0 and 0.3 (excluding the eclipsed region), and shows minima at phases 0.4 and 0.9. A number of factors may contribute to this behaviour: (i) Asymmetry in the radiation pattern of the bright region; for example it might be brighter on the side facing the white dwarf, causing the S-wave component to be stronger when viewed from the opposite side of the disc (i.e. after eclipse). (ii) The bright region may extend significantly around the disc, which could contribute to the asymmetry in the velocity curve if the radiation pattern were non-uniform (i.e. if optical depth effects are important). (iii) Obscuration of the bright region by material around the white dwarf, possibly material carried out of the orbital plane by the magnetic field lines; this might be the cause of the minimum at phase 0.4. (iv) A contribution to the line emission by lower velocity material in the gas stream from the companion.

Note that CMK have suggested that photoelectric absorption by material near the bright spot region of the disc is responsible for the broad dip in the low-energy X-ray light curve of EX Hya centered at about phase 0.85 in the orbital cycle.

2.4.3 67-MIN PULSED EMISSION

There are a number of observational facets that constrain models for the production of the pulsed component of the emission lines:

(i) The modulation of the line flux is in phase with that of the optical continuum in the current data (Section 2.3.1), and by implication in phase with the X-ray continuum variation also (CMK). Note that Gilliland (1982) found that the equivalent width of the lines peaked about 0.1 cycles before the continuum, so there may be some change in the relative phasing of the line and continuum modulations with time.

(ii) There is no evidence for a narrow eclipse of the line emission (Section 2.3.1). Thus the majority of the pulsed line component, which makes up about one third of the phase averaged flux of the Balmer lines, it not produced in the same place as the eclipsed component of the continuum. Assuming that the eclipsed continuum light is produced in the accretion column close to the surface of the white dwarf, this implies that the pulsed line emission is formed in a more extended region, most probably above the orbital plane where it is not occulted by the limb of the companion star.

(iii) There is a small change in the V/R ratio of the wings of the pulsed (Hγ) emission line with 67-min phase (Section 2.3.2). The sense of the variation is such that the maximum of the V/R ratio coincides with phase 0.0, which is the peak of the continuum and line flux variation. The fact that the V/R variability on the 67-min cycle is not more substantial

indicates that the pulsed line emission does not originate in a highly collimated flow, for instance a narrow accretion column as is seen in the AM Her stars.

(iv) The high velocities in the wings of the pulsed line component, ~ 3500 km s^{-1}, indicates that emitting gas extends almost to the surface of the white dwarf. If the mass of the white dwarf is $0.8\,M_{\odot}$, as derived in Section 2.3.3, then a velocity of 3500 km s^{-1} corresponds to a Keplerian radius of 8×10^8 cm, or a free-fall radius of 1.6×10^9 cm, i.e. at most a few white dwarf radii.

(v) The flat decrement of the Balmer lines (Hγ/H$\beta \sim 1$) implies that the line emitting region is optically thick.

To explain the properties of the pulsed line component, I propose the model sketched in Fig. 2.12b which shows a schematic cross-section through the white dwarf star in a plane perpendicular to the disc. The position of the observer at pulse maximum is indicated. In the model, the rotation axis of the white dwarf coincides with that of the disc, while the axis of the (assumed dipole) magnetic field is inclined at an angle δ. The accretion disc is disrupted by the magnetic field at about 10 white dwarf radii from the surface of that star, as suggested in Section 2.4.1.

In the model, the pulsed line emission originates in gas which is flowing down the field lines onto the surface of the white dwarf. Because the magnetic axis is inclined to the disc, matter will accrete preferentially from the side of the disc that is closest to the magnetic pole. This causes an asymmetry in the accretion pattern onto the white dwarf with the density contours of material at a given height above the white dwarf surface having a crescent shape and the maximum density occurring in the direction closest to the disc. The modulation of the line flux, and the continuum, is caused by the changing optical depth through the accretion stream along the observer's line of sight as the white dwarf rotates. Maximum flux occurs when the observer views the accretion stream most nearly sideways on, i.e. when the magnetic axis is most nearly in the plane of the sky, displaying maximum surface area. At phase 0.5 in the 67-min cycle, the observer is looking almost directly down the predominant accretion flow, and the optical depth is highest. It is difficult to make a quantitative comparison of the predicted and observed 67-min modulation amplitude because of the unknown contribution to the total light from un-modulated sources of radiation. However, in the model we describe, it would not be surprising if the 67-min modulation amplitude were greater in the lines than in the continuum because of the larger optical depth of the accretion column in the lines.

Note that in my model, the maximum line and continuum radiation is seen when the pole of the white dwarf is pointed *away* from the observer. This is the opposite of what has

often been assumed previously (e.g. Watson 1986). A similar geometry has been invoked by Rosen, Mason & Córdova (1988) for EX Hya to explain the energy dependence of the X-ray eclipse depth and that of the 67-min X-ray modulation amplitude. The model is consistent with the sense of the V/R variations in the line wings in that the maximum violet light occurs at phase 0.0 when the velocity vector of the main part of the accretion flow is directed towards the observer. The fact that there is still a red wing at phase 0.0, and a blue wing at phase 0.5, indicates that there is also some accretion occurring from the side of the disc opposite the one to which the magnetic pole is pointing (as indicated by the short arrows in Fig. 2.12b). Alternatively, the geometry of the source, as sketched in Fig. 2.12b, admits the possibility that part of the accretion column that feeds the pole which is below the disc plane is also visible. If so, this would contribute to the symmetry of the line profile and reduce the V/R variation with the spin cycle to the low level seen.

2.5 Conclusions

The dominant variation of the emission line flux occurs as a quasi-sinusoidal modulation at the 67-min spin period which is in phase with the optical and X-ray variations. The pulse fraction is greatest in the high velocity wings of the line, which originate nearest the white dwarf. There is also a radial velocity variation of the wings with the spin period, phased so that maximum blueness occurs at maximum flux. To explain the pulsed emission, I propose a new model in which the modulation is caused by the varying optical depth of an optically thick accretion curtain of material flowing onto the white dwarf. At maximum flux, the pole points away from the observer and is most nearly in the plane of the sky. The material flows towards the white dwarf, and the observer, producing blue-shifted emission. At phase 0.5 the observer looks down the accretion flow when the optical depth is highest, producing a flux minimum. The X-ray modulation is caused in a similar way to the optical, naturally explaining their similar profiles and phasing. The low level of the V/R variation with the spin period implies that we see emission from both poles which partially cancels out.

I also find spectroscopic evidence of an eclipse of material circulating around the white dwarf out to 80% of the primary's Roche-lobe (i.e. a disc). This produces marked line asymmetries near eclipse as first the approaching wing of the flow is eclipsed followed by the receding wing. A prominent *S*-wave feature, varying with the orbital cycle, arises from the impact of the mass transfer stream with the edge of the disc.

CHAPTER 3

EX Hydrae in outburst

3.1 Introduction

The previous chapter described a spectroscopic study of the quiescent EX Hya. Soon after that work was completed, in May 1987, EX Hya underwent an outburst rising from $\sim 13^{th}$ mag to $\sim 10^{th}$ mag for a two day period. Luckily, spectroscopy of this outburst was obtained with the Anglo-Australian Telescope — the first of EX Hya in outburst. One orbital cycle of coverage was obtained on each night of outburst. The 'target of opportunity' observations used a CCD to record the spectrum around Hα which yielded excellent signal-to-noise but poor time resolution. Comparing the observations with quiescent data was difficult as Hα had not been studied in quiescence. This was eventually solved by gaining more data at the South African Astronomical Observatory. To aid in interpreting the data, the analysis was also combined with photometry of the May 1987 outburst and of a previous one (July-Aug 1986) and also with visual light curves of the outburst obtained by the Royal Astronomical Society of New Zealand. This chapter reports all the data and is the first substantial study of EX Hya in outburst. The only previous digitally recorded data published is some photometry of the July-Aug 1986 outburst by Bond *et al.* (1987).

The outburst behaviour of EX Hya has been discussed by Bateson (1979). The outbursts are rare (~ 2 yearly intervals), last less than 4 days and have an amplitude of ~ 3 mags. The rise to maximum is always rapid (~ 12 hrs) and the decline lasts typically 2 days

3.2 Observations

Spectroscopy was obtained with the 3.9-m Anglo-Australian Telescope on the nights of the 5^{th} and 6^{th} May 1987 after notification that EX Hya was in outburst was received from Frank Bateson of the Variable Star Section of the Royal Astronomical Society of New Zealand. The observations were made as a secondary program and were affected by

cloud. One orbital cycle of spectroscopy of the region around Hα was obtained on each night. 5-min exposures were taken on the first night and 1-min exposures on the second night. The RGO spectrograph was used with the GEC CCD and 1200V grating giving a resolution of 1.3Å over the range 6350 – 6750Å.

For comparison with the outburst spectroscopy, I have obtained 2 orbital cycles of Hα spectroscopy when EX Hya was in quiescence, as there is none published in the literature. The data were taken at the South African Astronomical Observatory on the night of 23rd April 1988 using the 1.9-m telescope and the Unit Spectrograph with the Reticon Photon Counting System, yielding a resolution of 1.2Å.

Complementing the spectroscopy, photoelectric photometry from both the July-Aug 1986 and May 1987 outbursts is presented. High speed photometric data in the B-band were acquired at the South African Astronomical Observatory on five nights during the 1986 July-Aug outburst. EX Hya was brighter than mag. 12.5 on only one of these nights. W. H. Allen acquired UBV photometry with a time resolution of 2–3 mins at the Adams Lane Observatory, Blenheim, New Zealand during the May 1987 outburst.

3.3 The visual light curves

I show in Fig. 3.1 visual light curves of the two outbursts under consideration. These were kindly supplied by Frank Bateson of the VSS RASNZ. The figure also shows the times of the spectroscopic and photometric observations. The outburst curves are typical for EX Hya (see Bateson 1979) with rapid, unresolved rise times of less than 12 hours and linear decays lasting ~ 2 days. The amplitudes of the outbursts are ~ 3.5 magnitudes with EX Hya rising from 13th magnitude to around 9.5. The 1986 outburst was unusual, having a second rise to maximum occurring 8 days after the first. Although the data from this second rise are sparse they are consistent with a profile similar to both the first rise of the 1986 outburst and the 1987 outburst.

3.4 Photometry

The arrows in Fig. 3.1 indicate when outburst photometry was obtained during the 1986 and 1987 outbursts. Fig. 3.2 contains the data (upper panel) together with a typical quiescent light curve (lower panel) for comparison. The lower two curves in the upper panel were taken during the decline to the quiescent level after the first maximum of the 1986 July-Aug outburst. There is no apparent difference (other than in the overall intensity) between these data and quiescent light curves, of which the lower panel is

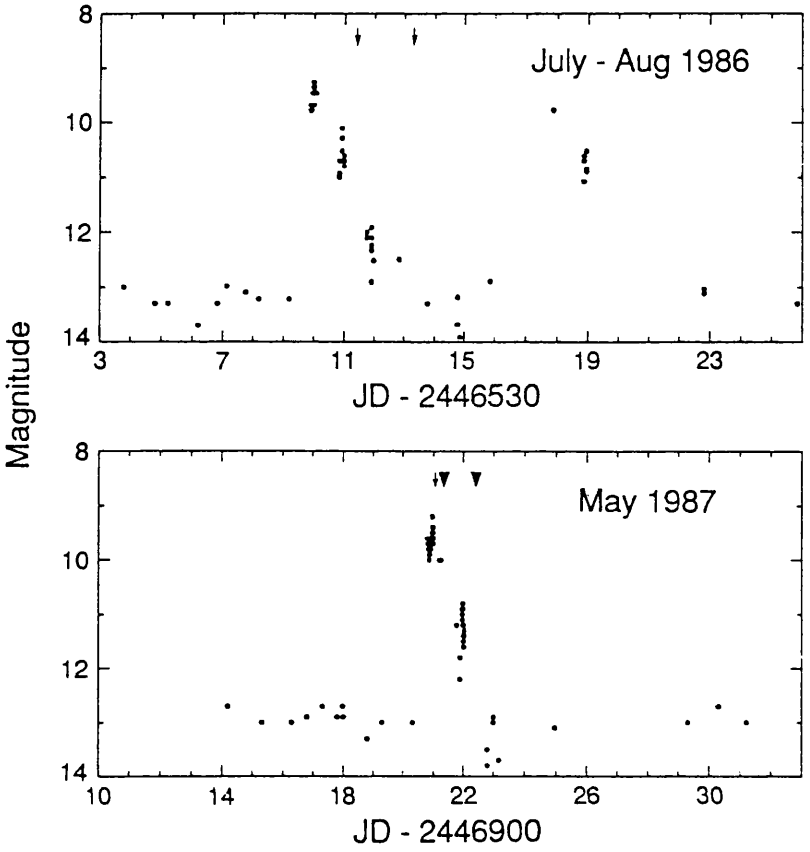

FIGURE 3.1: Visual light curves of EX Hya during the July-August 1986 and May 1987 outbursts. The data were supplied by the VSS RASNZ. The times of photometric (arrows) and spectroscopic (triangles) observations are shown.

typical (for other examples see Bond & Freeth 1988, Córdova, Mason & Kahn 1985 and Warner & McGraw 1981). The 67-min white dwarf spin period manifests itself as a quasi-sinusoidal modulation whose expected times of maxima are indicated by inverted filled triangles. Superimposed on this modulation are partial eclipses recurring with the 98-min orbital cycle.

The top light curve in the upper panel was obtained during the May 1987 outburst, the cycle before the first spectroscopic data run. In contrast to the light curves of the 1986 July-Aug outburst, these data are remarkable for showing little or no 67-min modulation. The simultaneous U and V data also show little evidence for a modulation.

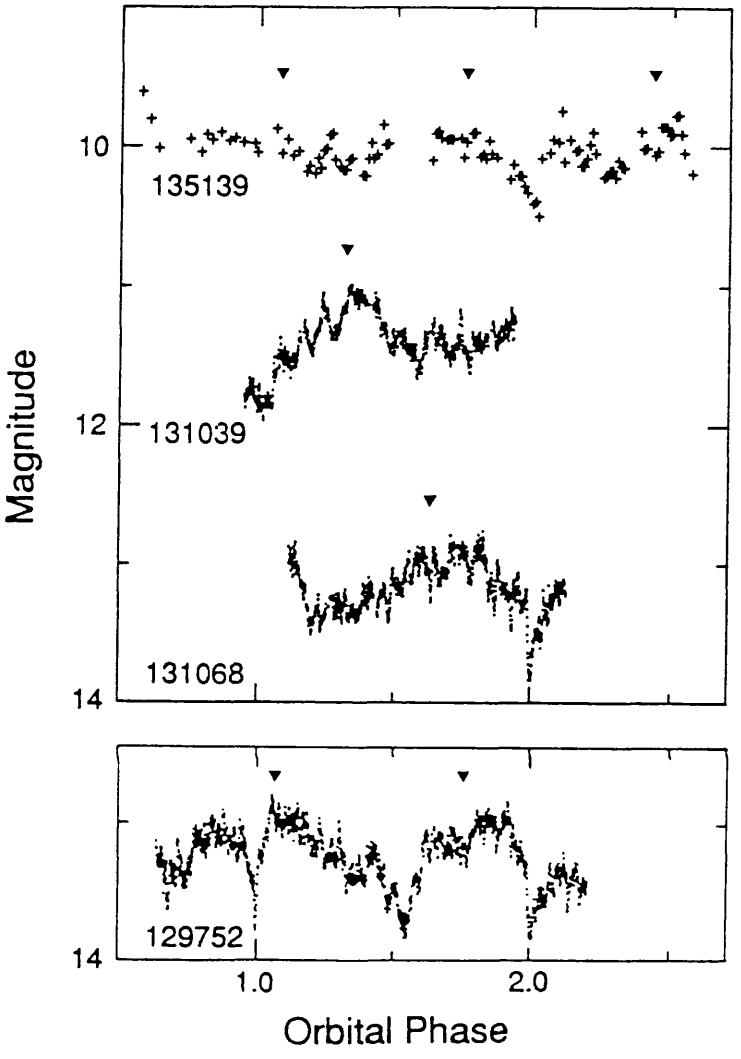

FIGURE 3.2: Photo-electric photometry of EX Hya. The top curve of the upper panel shows B-band data obtained at the Adams Lane Observatory during the May 1987 outburst. The other curves in the upper panel are B-band data obtained at SAAO during the July-Aug 1986 outburst. The times of these observations are shown in Fig. 3.1. For comparison the lower panel contains a typical quiescent curve obtained at SAAO in May 1986. The abscissa is orbital phase using Bond & Freeth's (1988) ephemeris; the figures giving the cycle number. The inverted filled triangles indicate times of maxima of the 67-min cycle according to Bond & Freeth's ephemeris.

3.5 Spectroscopy

I show in Fig. 3.3 the summed spectra, covering the Hα and He I λ 6678 lines, from the first night of the 1987 outburst (May 5th), the second night (May 6th) and in quiescence. The

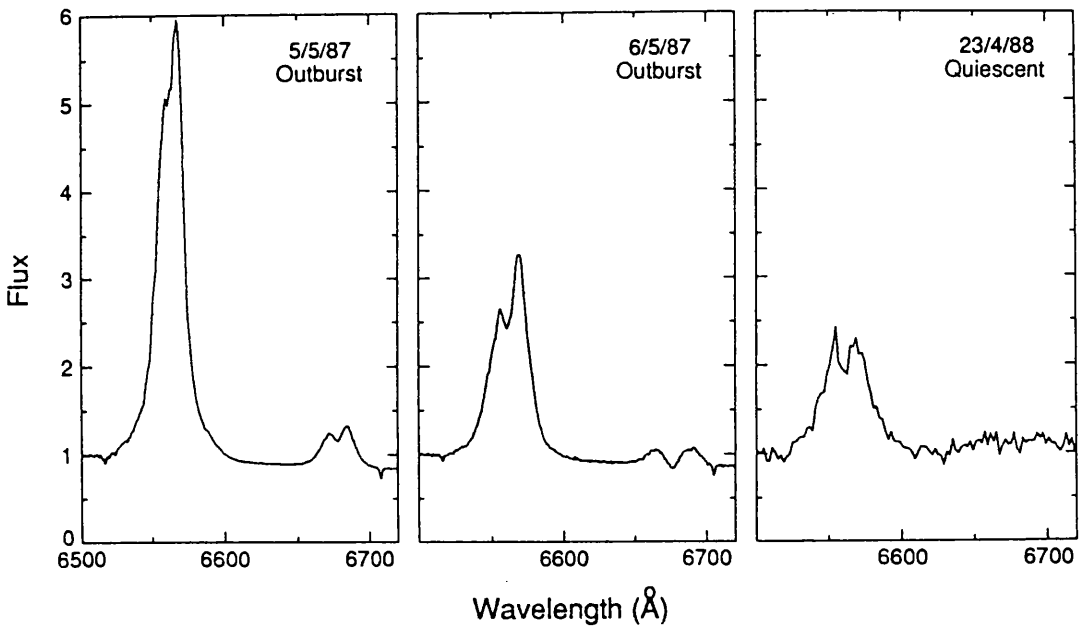

FIGURE 3.3: The summed spectra of EX Hya. The three panels show the spectra from the first night of outburst, from the second night and in quiescence. In all cases the spectra have been normalized to the continuum to aid comparison.

spectra are plotted normalized to the continuum. The equivalent widths of the emission lines are 125Å, 70Å and 50Å respectively for the Hα line in the three summed spectra and 13Å, 6Å and 2.7Å for the He I λ6678 line (note that on the second night the He I λ6678 contains a central absorption trough which subtracts from the equivalent width). As EX Hya was at magnitudes $\sim$ 10, 11.5 and 13 on these occasions there is a clear correlation between the star's brightness and equivalent width. The increased equivalent widths in the outburst data are not caused by greater line width; the Hα line extends to $\pm$2000 km s^{-1} (FWZI) in all three cases as illustrated in Fig. 3.4 where the spectra are superimposed. The extra equivalent width is concentrated in the central $\pm$500 km s^{-1} region. The summed Hα line from the first night of outburst has a profile at its base very similar to the quiescent spectra; note, though, that the profile from the the second night is significantly narrower near the base, a point discussed further in Section 3.5.2. The narrowness of the Hα line, even in quiescence, contrasts with the width of the Hβ and Hγ lines, which extend to $\pm$3500 km s^{-1} in quiescence (Chapter 2).

3.5.1 TIME VARIATION OF EQUIVALENT WIDTHS

The equivalent widths of the individual outburst spectra are shown in Fig. 3.5 together with the expected times of maxima of the 67-min cycle and the expected times of eclipse. No

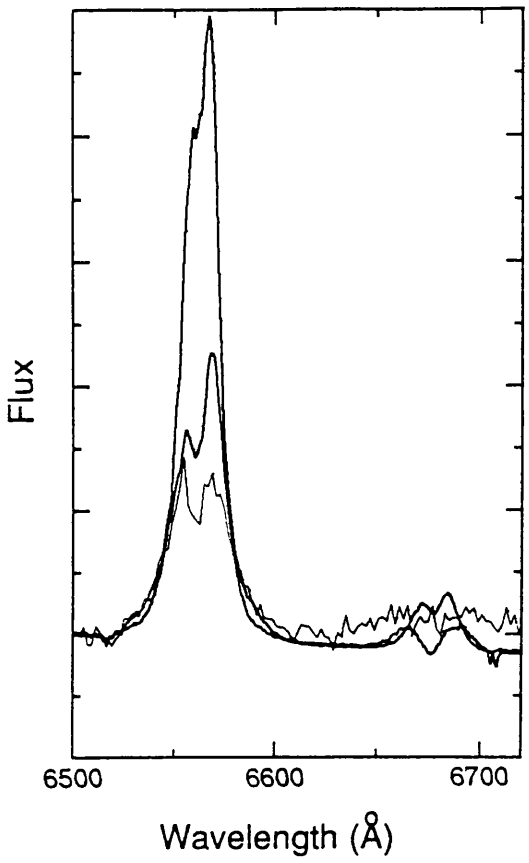

FIGURE 3.4: The summed spectra shown in Fig. 3.3 are plotted superimposed.

variation with the 67-min period is apparent. Its presence cannot by completely excluded, though, owing to the difficulty of detecting a modulation in a short data run where it could be masked by other effects, notably variations in the S-wave intensity. However, the photometry obtained in the cycle before the spectroscopic data (on May $5^{\rm th}$) also shows little or no 67 min variation (Section 3.4, Fig. 3.2).

In quiescence a dominant feature of the Balmer lines is a sinusoidal modulation of the equivalent widths with the 67-min period. This modulation is greatest in the wings of the lines and so produces a distinctive 'hourglass' shape in trailed spectra (Chapter 2, Kaitchuck *et al.* 1987). The quiescent spectra of the Hα line do show the expected equivalent width modulation although the half-amplitude is only 3 ± 1Å, corresponding to a pulse fraction of 0.06 ± 0.02. In contrast the pulse fractions for the quiescent Hβ and Hγ lines are 0.18 and 0.25 respectively. The 67-min pulsed emission is assumed to come from the inner regions near the white dwarf where the accretion disc is disrupted by the magnetic field. The lower pulse fraction for the quiescent Hα line is therefore consistent

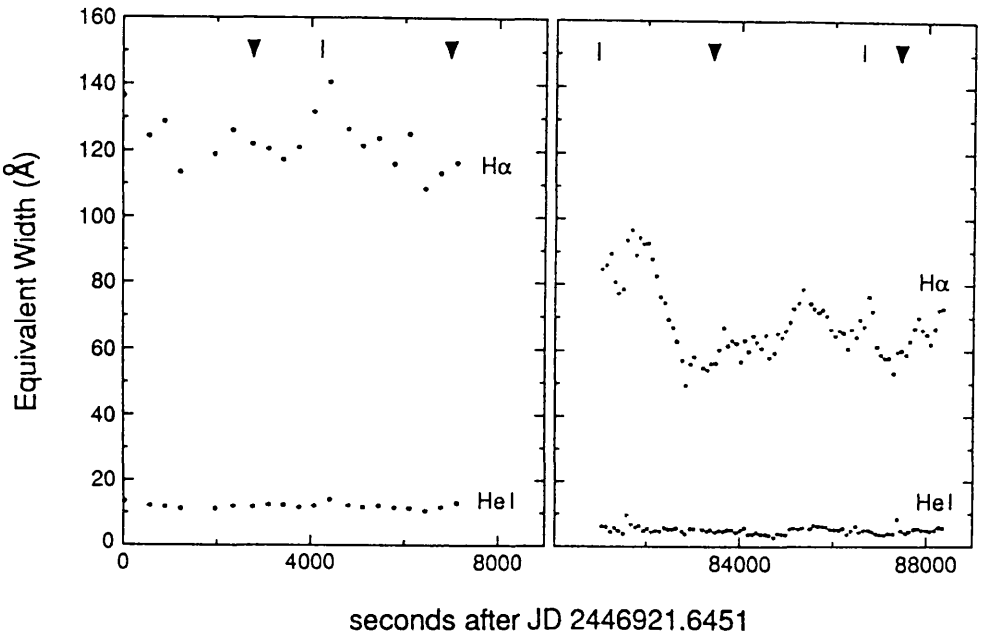

FIGURE 3.5: The equivalent widths of the Hα and He I λ 6678 lines in the individual spectra are shown together with the expected times of 67-min maxima (triangles) and the expected times of eclipse (vertical dashes).

with the narrower overall width of the Hα line compared with the Hγ and Hβ lines and suggests that the innermost, high velocity regions emit comparatively weakly in Hα during quiescence.

In outburst the lack of equivalent width variation with the 67-min period during outburst can be explained by an extension of the above effect with the inner regions emitting relatively less Hα than in quiescence. This idea is supported by the profile of the Hα line from the second outburst night which shows a decreased width in the wings compared to quiescence (Fig. 3.4). Although the summed Hα base profile from the first night appears wider than that from the second night, this is because it also contains a broad base component which is modulated with the orbital period (see Section 3.5.2). When this component is subtracted from the data the remaining profile is of similar width to that on the second night.

The quiescent emission lines in EX Hya show an increase in equivalent width during eclipse which suggests that the continuum emission is eclipsed to a greater extent than the line emission (Chapter 2). There is some evidence in the equivalent width data near eclipse (Fig. 3.5) that this also occurs during outburst.

Most of the variations in the equivalent widths over an orbital cycle are attributable to variations in the intensity of the S-wave component of the emission lines. The S-wave

is brightest soon after eclipse and is responsible for the increased equivalent width at the beginning of the second night's data. Comparison of the Hα line profiles at the start of the second night's data with those an orbital cycle later shows that the equivalent width has declined. When allowance is made for variations in the S-wave, the profiles are consistent with a progressive decline, which in Section 3.5.2 I attribute to absorption.

3.5.2 THE LINE PROFILES

Fig. 3.6a shows sample Hα profiles from the 5-min exposure spectra taken on the first night of outburst. Fig. 3.6b shows Hα data from the second night, where three adjacent 1-min exposures have been combined in each profile. Fig. 3.6c shows the He I λ 6678 profiles from the two nights; the data from the first night being single 5-min exposures, while the second night data are sums of five consecutive 1-min exposures. All data have been normalized to the continuum to aid comparison. The data are displayed in greyscale form in Fig. 3.7 as a continuous time sequence. The blank strip during the first night is a region missed because of cloud.

The S-wave

An S-wave component, varying with the orbital period, is prominent in both emission lines during the observations on both outburst nights. A similar feature is seen in quiescence. Estimating the velocity amplitude of the S-wave is complicated by the other components in the lines. Subtracting the outburst Hα line profile from the quiescent profile yields a gross difference that is approximately Gaussian (Fig. 3.4). This addition of a single peaked component results in an apparent lowering of the velocity amplitude of the S-wave compared to quiescence — this is particularly so during the first night. The opposite effect is seen in the He I λ 6678 line during the second night where the presence of strong absorption in the line centre results in the double peaked structure appearing with increased separation. To examine the S-wave in the Hα line, I have subtracted from the outburst data the largest Gaussian profile that was contained under all spectra. Having done so, I measure the full amplitude of the S-wave to be 22 ± 4Å, which corresponds to a velocity half amplitude of ~ 500 km s^{-1}. In Chapter 2 the quiescent value was measured as ~ 600 km s^{-1}, which is the expected Keplerian velocity near the outer edge of an accretion disc nearly filling the Roche-lobe of the primary. Given that the phasing of the S-wave is the same in outburst as in quiescence, I interpret the S-wave in the same way, that is, as the result of the impact of an accretion stream with the edge of an accretion disc, and conclude that the existence and position of this impact region is not substantially altered

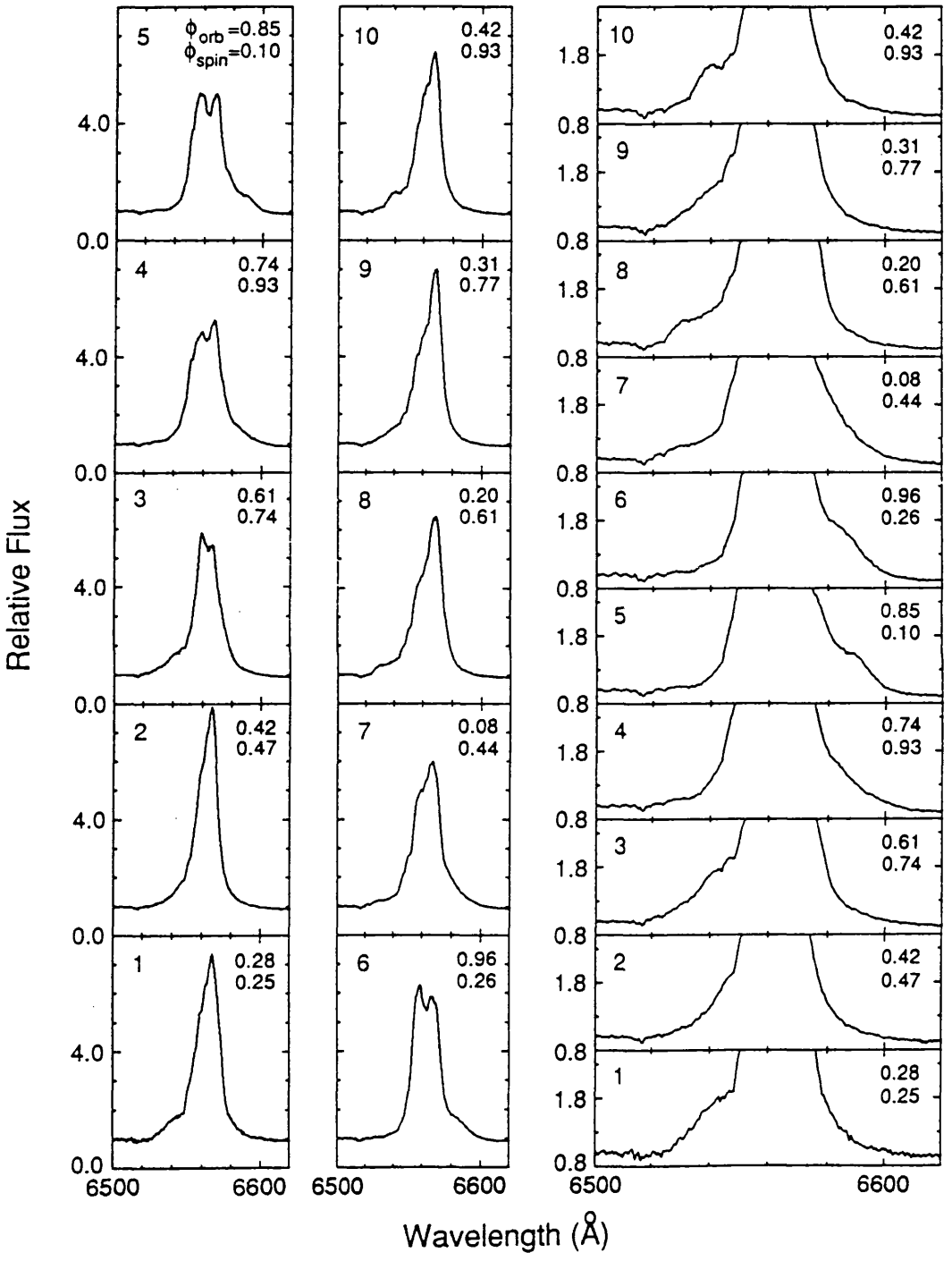

FIGURE 3.6: Sample profiles of Hα from the first night of outburst. The inset numbers give the orbital and spin phases of the spectra. Time increases up the page. On the right the profile bases are expanded to show the 'base excursion' feature varying with the orbital period. The profiles are shown relative to the continuum level.

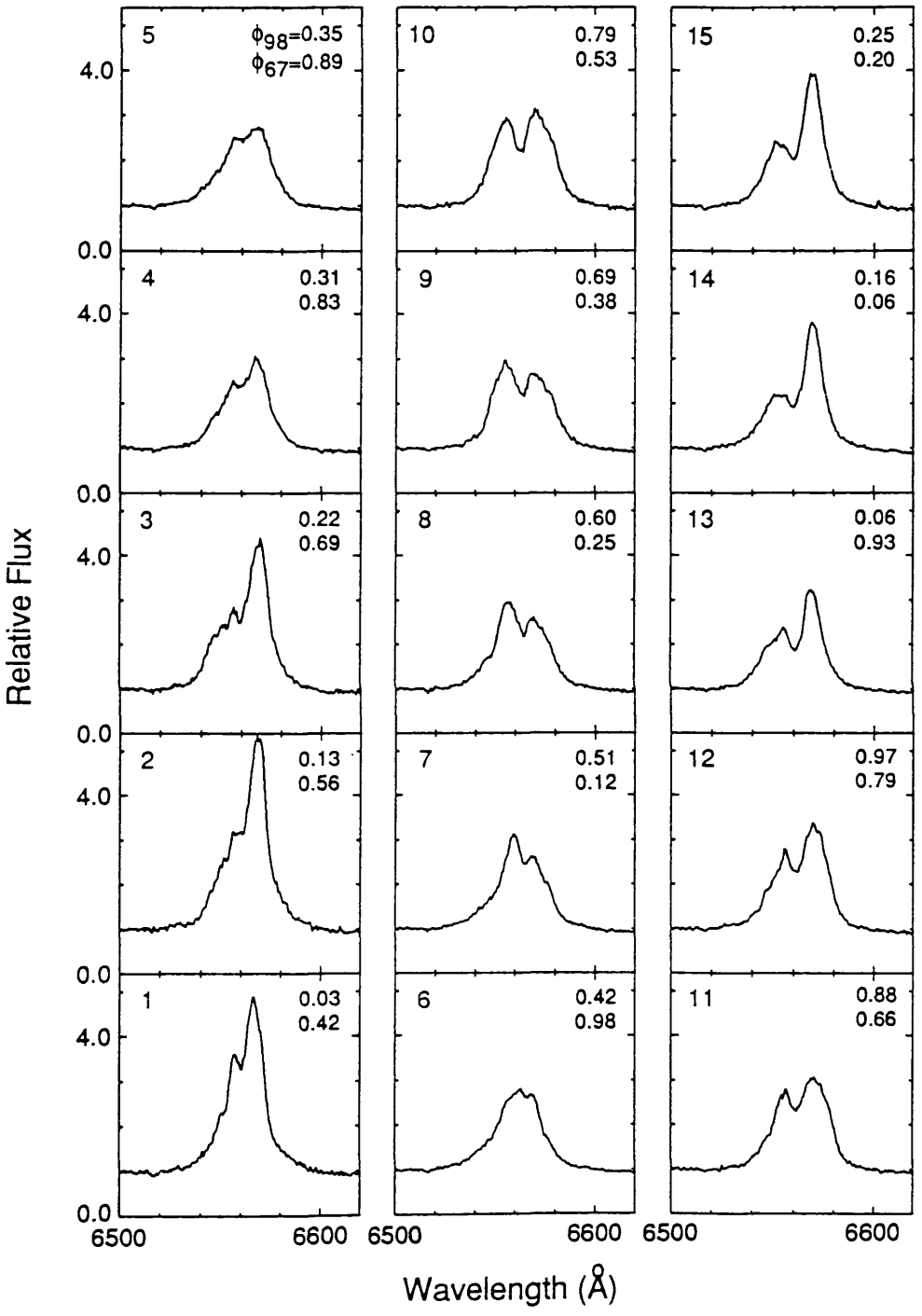

FIGURE 3.7: Profiles of the Hα line from the second night of outburst. Each profile is the sum of three consecutive spectra. The inset numbers give the orbital and spin phases.

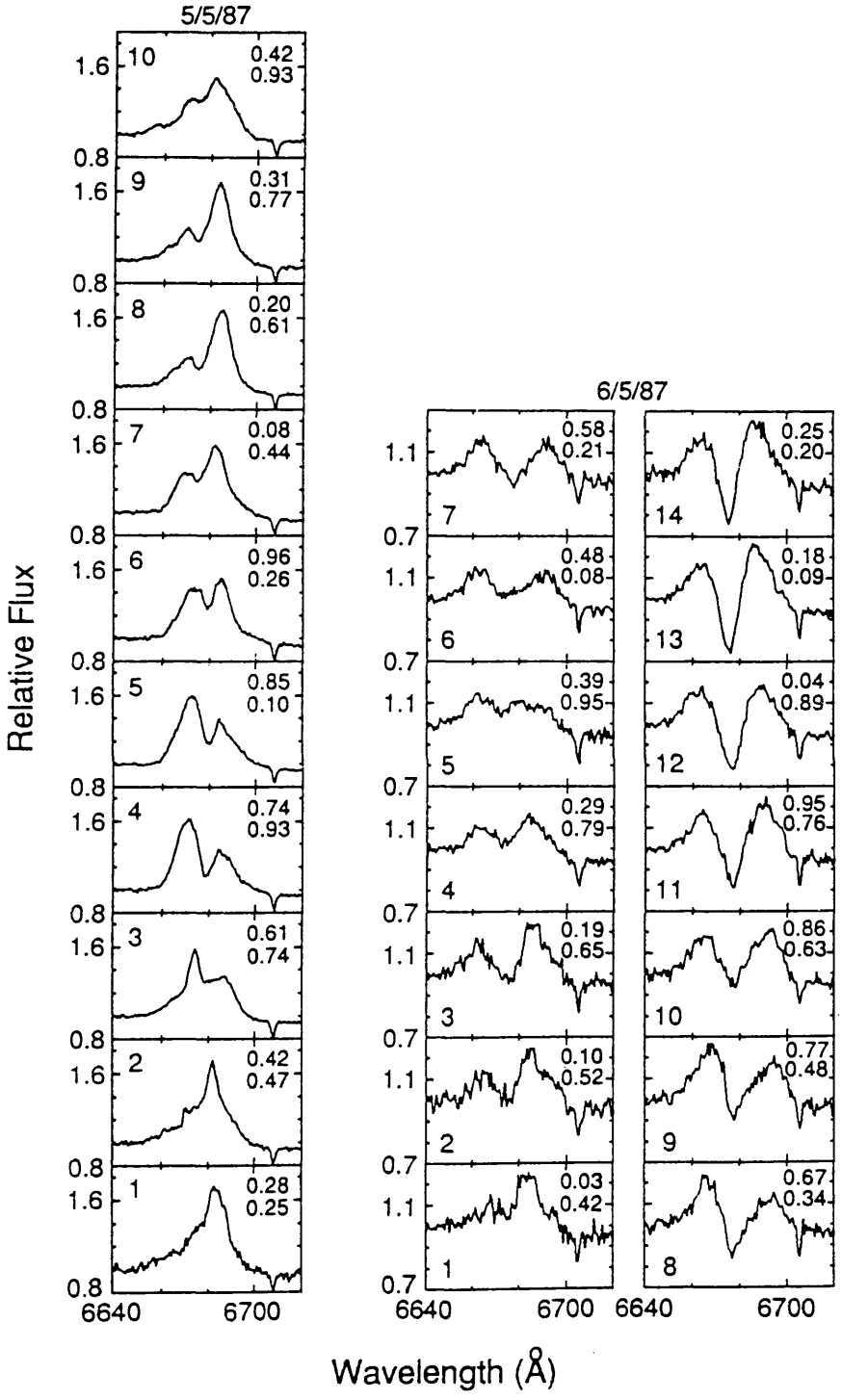

FIGURE 3.8: Profiles of the He I λ 6678 line. The left panel shows sample spectra from the first night of outburst. The right panel shows sums of five consecutive spectra taken during the second night. The upper figure in each spectrum gives the orbital phase and the lower figure the spin phase. Note the appearance of the absorption during the second night.

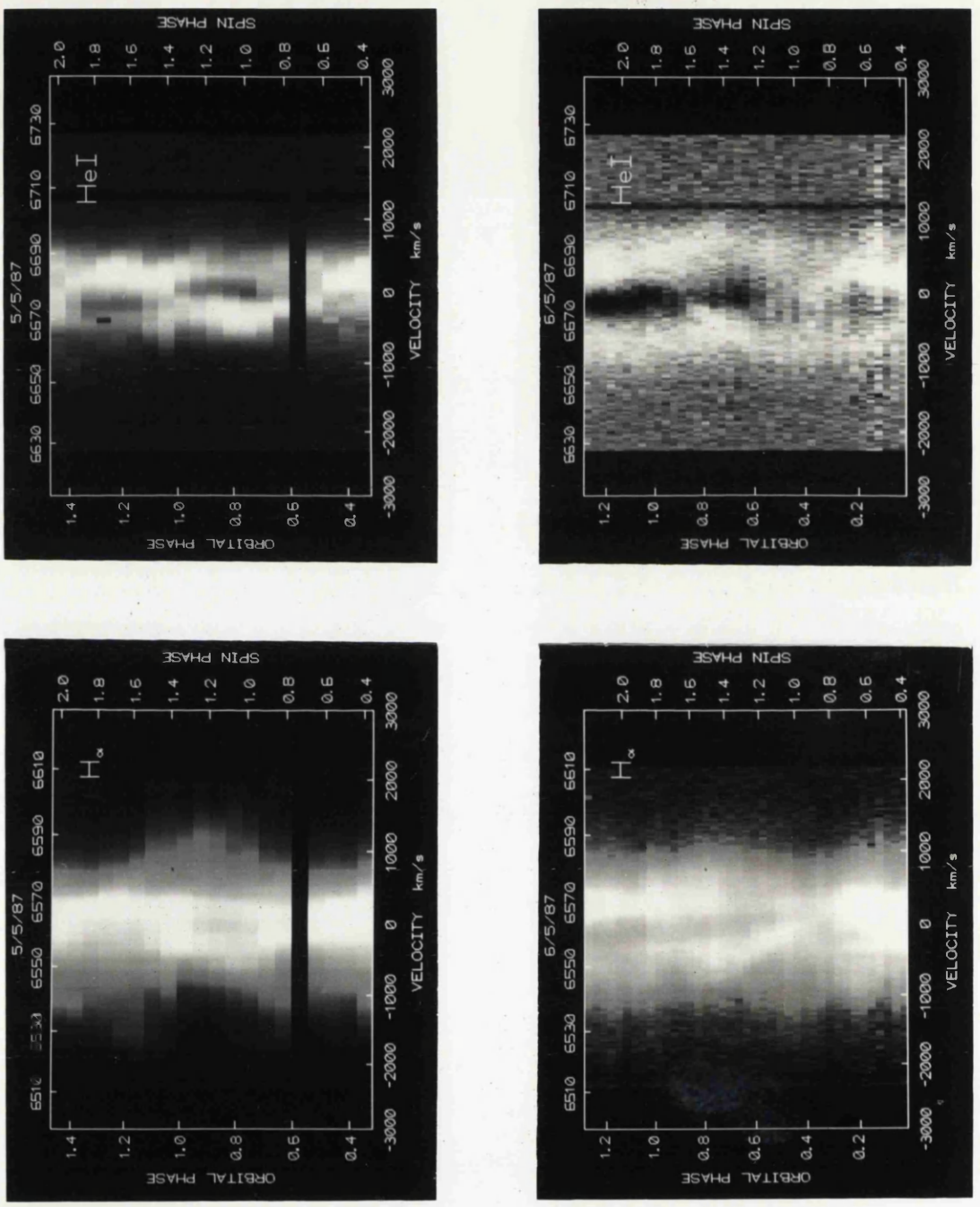

FIGURE 3.9: The spectra of EX Hya during outburst displayed as a greyscale plot against time. Note the 'base excursion' feature prominent in the Hα line on the first night (upper left) and its relationship with the narrower S-wave. The greyscaling is non-linear to enhance the interesting features of the lines.

by the outburst.

The intensity of the S-wave is much greater when at maximum redshift ($\phi_{98} \sim 0.2$) than at maximum blue shift. This asymmetry is also present in quiescence but to a lesser extent. The effect is most noticeable in the Hα spectra from the second night where the red peak is twice the height of the blue peak at some phases. This results in the summed spectra (Fig. 3.4) having a larger red peak than blue peak.

The Hα line profile base

A striking feature of the Hα profiles from the first night of outburst is evident in the high velocity wings. Initially the spectra show an enhanced blue wing; this enhancement then moves to the red wing before returning. In Fig. 3.6a the base of the line profile is expanded to show this clearly. The motion of this component is consistent with the 98-min orbital period and is clearly inconsistent with the 67-min spin period; although as the data cover only 1.2 orbital cycles the identity with the orbital period cannot be established conclusively. Assuming that the motion is at the orbital period, this modulated broad base component (hereafter referred to as the 'base excursion') is similar in appearance to that seen in AM Her stars (e.g. Rosen, Mason & Córdova 1987), which is attributed to material in the magnetically confined accretion stream near the white dwarf.

The higher velocities of the base excursion imply that it originates much nearer the white dwarf than the narrow S-wave which I assigned to the outer edge of the accretion disc (Section 3.5.2). Tracing the base excursion from its reddest extent at the phase of maximum red shift to its bluest extent at the phase of maximum blue shift yields a total amplitude of 75Å. This corresponds to a maximum velocity of ± 1700 km s^{-1}. Assuming a $0.8 M_{\odot}$ mass white dwarf (Chapter 2) this is the freefall velocity at a radius of 7×10^9 cm ($\sim 10\, R_{WD}$), which is thus the outer limit to the radius of the region emitting the base excursion. In Chapter 2, I estimated a value of 6×10^9 cm for the radius at which the accretion disc is disrupted by the white dwarf's magnetic field in quiescence. Given that the base excursion varies with the orbital cycle this suggests that it may arise from the impact of a stream of material, fixed in the orbital frame, with the magnetosphere of the white dwarf. The base excursion is phased with maximum blue shift at $\phi_{98} \sim 0.4$ and maximum red shift at $\phi_{98} \sim 0.9$. This places the emission region at the expected phase for a stream of matter that is following a ballistic trajectory from the inner Lagrangian point to the radius of the magnetosphere.

The width of the base excursion at any one phase is difficult to determine, owing to the other line components, but is around 50Å, corresponding to a velocity spread of around

2000 km s^{-1}. This could be explained by turbulence in the emission region or by requiring that the emission region be extended in phase.

Examination of the Hα profiles from the second night reveals no evidence for the base excursion. This is confirmed by the summed spectra shown in Fig. 3.4 where the width of the Hα line near the base is clearly narrower on the second night than on the first, indicating that it is not broadened by the base excursion. The He I λ 6678 line also shows evidence for the base excursion on the first night but not on the second (Fig. 3.6c). None of the quiescent studies have reported any similar feature (Chapter 2, Kaitchuck *et al.* 1987, Gilliland 1982).

The progressive absorption

The spectra from the second night show the progressive appearance of strong absorption in the line profiles on a time scale of ~ 1 hour. This is most noticeable in the He I λ 6678 profiles, which are initially entirely in emission but eventually display a central absorption trough down to 0.8 of the continuum level. The equivalent width of the line, however, stays approximately constant (Fig. 3.5) with the absorption compensated for by increased intensity of the peaks on either side. Comparison of the Hα profiles from the second night reveals changes consistent with similar levels of absorption, although the lines remain entirely in emission. The appearance of absorption in the line center is similar to that seen by Honey *et al.* 1988 in Z Cha during super-outburst. However, in other dwarf novae during outburst (e.g. RX And; Kaitchuck, Mansperger & Hantzios 1988 and SS Cyg; Clarke, Capel & Bowyer 1984) the emission lines change to absorption across their entire width which is followed by the re-appearance of an emission peak in the line center; this eventually grows to re-establish the quiescent profile.

3.6 Discussion

The most notable difference between the outburst and quiescent spectroscopy is the appearance of a broad high velocity component, probably varying with the orbital period, in the base of the Hα line profiles; the 'base excursion' (Figs. 3.6a & 3.7 and Section 3.5.2). The maximum velocity of this feature corresponds to the freefall velocity at a distance from the white dwarf of $\sim 7\times10^9$cm, similar to the radius of the quiescent magnetosphere, 6×10^9cm, estimated in Chapter 2. The radial location of the material emitting the base excursion would be less than 7×10^9cm if it had lost momentum and was travelling below the freefall velocity. The magnetospheric radius may also be decreased in outburst due

to an increased mass transfer rate ($r \propto \dot{m}^{-\frac{2}{7}}$; e.g. King, Frank & Ritter 1985). The base excursion is phased with maximum blue shift at $\phi_{98} \sim 0.4$, consistent with the expected phase of impact of a stream of material leaving the secondary star and free-falling onto the primary's magnetosphere (Lubow & Shu 1975) as illustrated in Fig. 3.8. The continued existence of the narrow, lower velocity S-wave and double peaked line structure implies that the accretion disc remains during outburst. I suggest, therefore, that the material responsible for the base excursion results from overspill of the accretion stream from the initial impact region with the disc. This material flows over the disc on a ballistic trajectory before being disrupted at the magnetospheric radius. This scenario is illustrated in Fig. 3.8.

There is no evidence for the base excursion in the Hα spectra from the second night of outburst, implying that the overspill no longer occurs. This could be accounted for by a reduced mass transfer rate from the secondary, which is supported by the fact that EX Hya was at this time ~ 2 magnitudes fainter than on the first night.

The evidence of the spectroscopy is thus in favour of a model where the outburst is caused by an increase in the flow of material overflowing the secondary's Roche-lobe. An alternative scenario invokes disc instabilities causing an increase in the accretion rate onto the white dwarf (e.g. Bath & Pringle 1985, Meyer & Meyer-Hofmeister 1984). This is harder to reconcile with the appearance of a modulation on the orbital period, although it is conceivable that such an instability might alter the disc to such an extent that the stream from the secondary overflows the disc without an increase in mass transfer rate. The similarity of the outburst S-wave to the quiescent S-wave suggests, however, that the outer edge of the disc is not significantly changed during outburst. In addition, the equivalent width of the S-wave component of the emission lines is similar in outburst and in quiescence. Thus, the flux from the S-wave participates in the outburst, suggesting increased mass transfer, whereas the disc instability model predicts a constant S-wave component which would be swamped during outburst.

The situation that I suggest occurred during the outburst has also been proposed as a property of some other intermediate polars in their normal state. Mason, Rosen & Hellier (1988) have suggested that if part of the mass transfer stream impacted directly onto the magnetosphere, a modulation at the beat of the orbital and spin periods would result. This could explain the observation of such a modulation in the X-ray light curves of H0542–407 (Tuohy *et al.* 1986) and possibly V1223 Sgr (Rosen 1987). Unfortunately, I do not have sufficient data to investigate whether a beat period modulation appears in EX Hya during the outburst. The proposed scenario is also similar to the model for intermediate polars

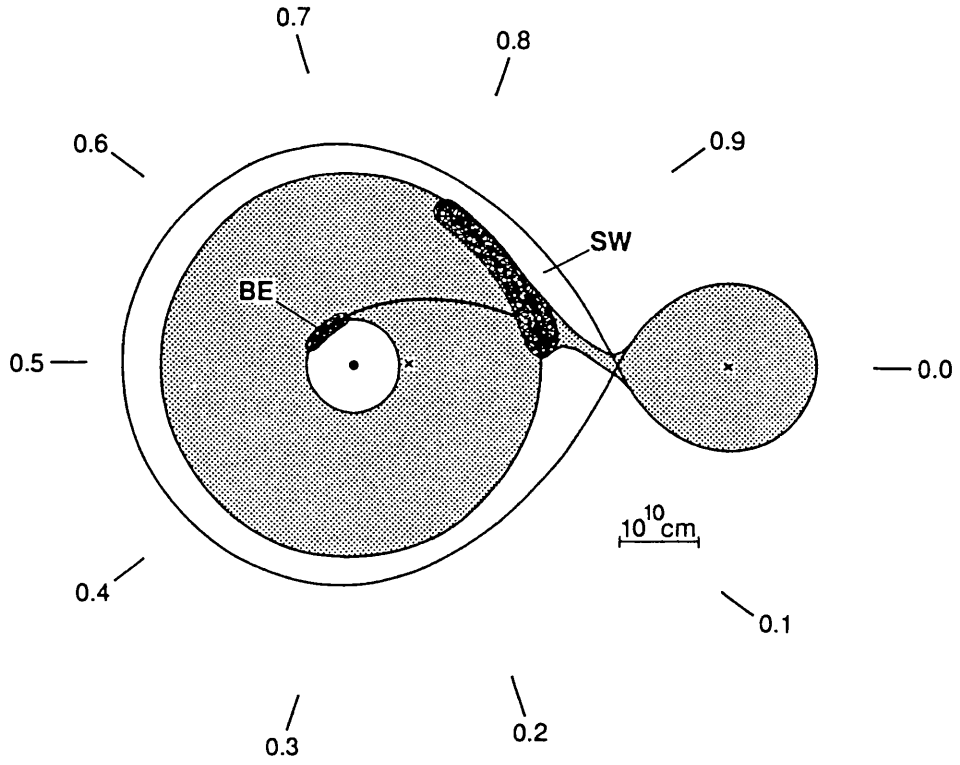

FIGURE 3.10: A schematic picture of EX Hya during outburst showing the positions of the regions emitting the *S*-wave (SW) and base excursion (BE). I suggest that the base excursion is produced by an enhanced mass flow from the secondary overflowing the initial impact region with the disc and following a ballistic trajectory to the magnetosphere of the white dwarf. The inner disc radius is drawn unchanged from its quiescent value (Chapter 2) as might be expected near the beginning of an outburst caused by increased mass flow from the secondary which has not yet permeated through to the inner disc. However the data provide insufficient information to attempt an accurate reconstruction of the complex interaction between the disc, stream and magnetic field. The illustrated system geometry is justified in Chapter 2.

by Hameury, King & Lasota (1986). They predict that in systems with orbital period less than 5 hours the magnetic field is sufficient to prevent any disc from forming and the entire accretion stream impacts directly onto the magnetosphere.

If the suggested 'disc overflow' model is correct, one might also expect the 'splash' caused by the impact of the enhanced mass stream from the secondary with the outer disc to throw up material away from the disc. Such low velocity, cooler material could be responsible for the absorption seen in the line profile centres later in the outburst.

The photometry of the May 1987 outburst contrasts with that of the July-Aug 1986 outburst, and with all quiescent photometry, in showing little evidence of the 67-min spin

modulation (Fig. 3.2). The photometry of the May 1987 outburst was, however, obtained while EX Hya was brighter ($\sim 10^{th}$ mag) than during any of the times of photometry of the July-Aug 1986 outburst. The difference could thus be explained if the mechanism producing the 67-min modulation was inoperative during the brightest parts of outburst. Alternatively, at the highest intensities, the modulated light could be a smaller than normal proportion of the total intensity and thus the 67-min modulation would be swamped.

The Hα spectroscopy of the May 1987 outburst also shows no evidence of the 67-min modulation. This modulation is visible in the Hα line during quiescence, but at a lower amplitude than in the Hβ and Hγ lines, the pulse fractions being 0.06, 0.18 and 0.25 respectively (Section 3.5.1). The 67-min modulation is produced in the high velocity material near the white dwarf and is thus most apparent in the line wings (Chapter 2). The analysis in Section 3.5.1 shows that, apart from the appearance of the base excursion, the high velocity wings of the Hα line are comparatively weak in outburst. Thus, one expects that the 67 min modulation would be decreased from its already low level.

The data are compatible, therefore, with a continuing 67-min modulation during outburst, which contributes a lower than normal fraction of the total intensity during the brightest periods. Also, near the outburst peak, the emission lines show increased equivalent width concentrated in the low velocity line center, suggesting its origin in the outer disc. These results are in agreement with the model of the outburst as a mass-transfer event which, at its peak, causes the greatest increase in optical luminosity in the outer disc and has not yet penetrated to the inner regions dominated by the white dwarf's magnetic field.

3.7 Conclusions

I present data from two outbursts of EX Hya which lasted ~ 2 days and had amplitudes of ~ 3.5 magnitudes. I suggest that the outbursts are caused by an increase in mass transfer from the secondary. The increased gas stream interacts with the outer edge of the accretion disc causing: (1) An *S*-wave feature in the emission lines with intensity greatly enhanced over quiescence. (2) Increased equivalent width in the emission lines concentrated in the line center. (3) A swamping of the light from the regions near the white dwarf and hence a lower amplitude of the 67-min spin modulation. Some of the mass transfer stream overflows the initial impact region with the disc and falls on a ballistic trajectory to the magnetosphere of the white dwarf where is gives rise to a broad, high velocity component in the wings of the Hα line, whose velocity is modulated with the orbital period. Later in the outburst this feature disappears implying a lessening of the mass transfer rate.

CHAPTER 4

Spectroscopy of FO Aquarii

4.1 Introduction

The extensive spectroscopic study of EX Hya presented in Chapter 2 showed the value of this kind of study of intermediate polars. In that chapter I proposed a new model for the optical spin period modulations in EX Hya. It was therefore worthwhile to study other IPs to discover whether the model had general applicability. Accordingly, I undertook a similar spectroscopic study of FO Aqr which is presented here.

The optical and X-ray light curves of the 13^{th} mag cataclysmic variable FO Aqr (H2215–086) are dominated by a coherent modulation with a period of 20.9-min (e.g. Patterson & Steiner 1983, Cook, Watson & McHardy 1984). This establishes it as an intermediate polar.

A second, longer period modulation is seen in optical light curves and is associated with the orbital period of the binary. Aliasing problems have hindered the determination of this period but agreement has now been reached (Osborne & Mukai 1988, 1989, Patterson 1988) that the orbital period is 4.85 hr, the one day alias of a 4.03 hr period which had previously been widely accepted.

Spectroscopically, FO Aqr shows prominent, doppler broadened Balmer and Helium emission lines. The behaviour of the emission lines with the orbital period in FO Aqr, in particular the phasing of variations, has not been well determined with seemingly conflicting results being reported in the literature (Shafter & Targan 1982, Penning 1985, Mateo 1985; see also Patterson 1988 for a discussion of these reports). This situation has been complicated by the uncertain orbital period. Penning (1985) reported that the emission line velocities also varied with the spin period although, due to the short data run, this could not be distinguished from the beat period between the orbital and spin periods.

To discover the true nature of the emission line variations with the orbital and spin periods and to investigate possible beat period variations I have accumulated 17 hours of time resolved spectroscopy of FO Aqr.

FO Aqr has generally been considered a low inclination system owing to the low values of detectable orbital motion in the emission line wings. Based on a measured K_1 value of 60 km s^{-1}, Shafter & Targan (1982) placed an upper limit on the inclination of $\sim 28°$, assuming a white dwarf primary. The data presented here, however, show that FO Aqr is actually a high inclination system with evidence of an eclipse of an accretion disc.

4.2 Observations

The observations were made at the South African Astronomical Observatory with the 1.9-m telescope, Image Tube Spectrograph and the Reticon Photon Counting System. I obtained a series of spectra, each of 1-min integration, covering over an orbital cycle on each of the nights 1988 August 2, 3 and 5. In total, 1000 spectra were obtained. The wavelength coverage was from 4200–5000Å at a resolution of 1.2Å. Regular exposures of a Cu/Ar arc determined the wavelength calibration and observation of standard stars determined the flux calibration. The third night was photometric but observations on the first two nights were affected by dust in the atmosphere.

4.3 Analysis

The phase averaged spectrum of FO Aqr derived from the data is shown in Fig. 4.1. A feature of the RPCS detector causes a semi-regular modulation of the data with a period of four pixels. I have reduced this effect by notch filtering the Fourier transform of the spectrum at the four pixel frequency before re-transforming to produce the cleaned spectrum. The spectrum is dominated by the emission lines, Hβ, Hγ and He II λ4686 while also visible are He I λ4388, 4471, 4713, 4921, 5015, He II λ4542, the C III/N III blend at λ4640–4650 and O II λ4416. Note the marked asymmetry of the He I lines which have much reduced red wings. The Balmer lines show this feature to a lesser extent. The emission line wings extend typically for $\pm$ 800 km s^{-1}.

4.3.1 Periodic variation of the emission lines

To detect variations of the emission line profiles I have calculated the two orthogonal measures, the equivalent width and the V/R ratio. The latter is simply the ratio of the equivalent widths on either side of the line rest wavelength. These quantities were then Fourier analysed; Fig. 4.2 shows the power spectra obtained. To illustrate the window pattern produced by the incomplete sampling, one panel of Fig. 4.2 contains sinusoidal

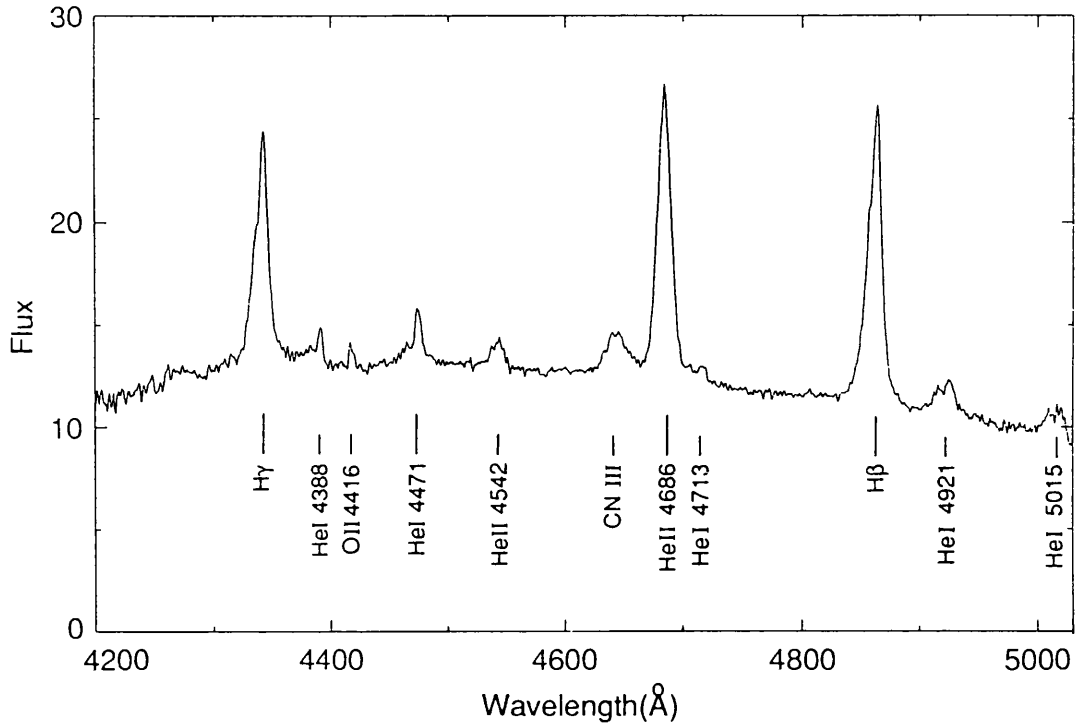

FIGURE 4.1: The phase averaged spectrum of FO Aqr

tracers at the orbital and spin periods. The sampling covers the phase space defined by the orbital, spin and beat periods uniformly, thus any variations at one period are completely smeared out when the data are folded on another period. Clearly visible in the Fourier transforms of the equivalent widths and V/R ratios are variations at the orbital (Ω) and spin (ω) frequencies. Note that there is a difference in orbital behaviour between the He II λ 4686 line, which shows power at the fundamental orbital frequency, and the Balmer lines which exhibit as much power at twice the orbital frequency. Also apparent in the He II λ 4686 line are variations at the beat periods $\omega - \Omega$, $\omega + \Omega$ and $\omega - 2\Omega$. Thus the data display the full range of periods predicted by Warner (1986). Having determined the periods of variation by Fourier analysis I have folded the equivalent widths and V/R ratios on these periods. The results are discussed below. In all analysis I have used the linear orbital ephemeris and the quadratic spin ephemeris of Osborne & Mukai (1989).

4.3.2 ORBITAL PHENOMENA

Fig. 4.3 shows the equivalent widths and V/R ratios of the emission lines in our data folded on the orbital period. Note that the behaviour of the He II λ 4686 line is very different from that of the Balmer and He I λ 4471 lines — as expected from the difference in their Fourier

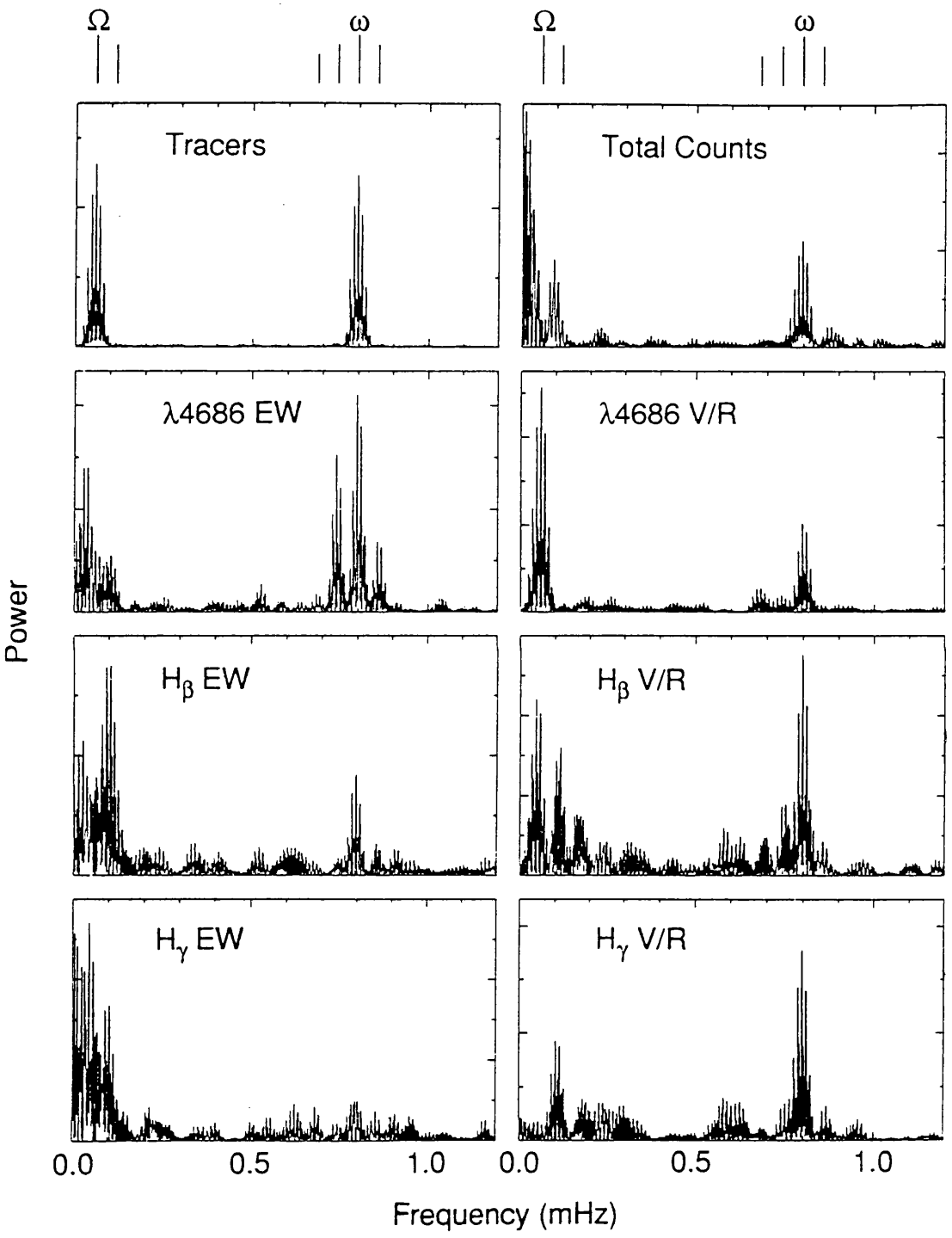

FIGURE 4.2: Fourier transforms of the equivalent widths and V/R ratios of the emission lines in FO Aqr. To illustrate the window pattern, the top left panel shows sinusoidal tracers at the spin and orbital periods sampled as the data. At top right is the fourier transform of the total counts in each spectrum. The tick marks on top indicate the orbital (Ω) frequency and its first harmonic and the spin frequency (ω) and its orbital side-bands.

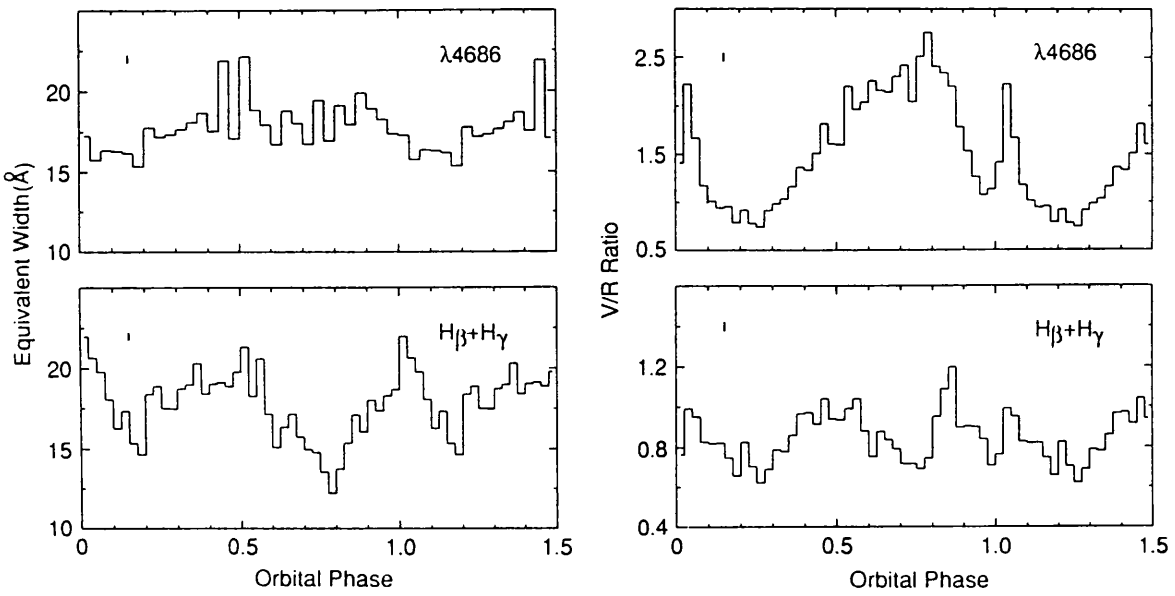

FIGURE 4.3: The equivalent widths and V/R ratios folded on the orbital period. The upper panels show data from the He II λ 4686 line and the lower panels the sum of data from Hβ and Hγ.

transforms. In the He II λ 4686 line the V/R curve shows a large sinusoidal variation characteristic of an *S*-wave together with a narrow, marked departure from this variation at phase 0.025. The equivalent width is roughly constant except for a dip between phases 0.0–0.2. The behaviour of the Balmer lines and He I λ 4471 is more complex, with two peaks (at phases 0.5 and 1.0) in equivalent width per cycle. These peaks are approximately coincident with maximum V/R ratio of the profiles.

The eclipse

To examine the changes in the He II λ 4686 line near phase 0, Fig. 4.4 shows the V/R ratio of the He II λ 4686 line folded on the orbital cycle. As there are also V/R variations with the spin period, I have subtracted a best-fit spin period sinusoid from the data before folding; this reduces the scatter when folded on the orbital period but does not significantly affect the shape of the variation. To guide the eye, I have fitted a sinusoid to the dominant *S*-wave variation, excluding data around phase 0. Just after phase 1.0 (which corresponds to photometric orbital minimum), there is a marked departure from the sinusoidal variation. The line firstly becomes redder and then rapidly bluer, before returning to the sinusoidal trend. This feature is present at all three orbital minima observed, with the same phase, and is also present in the Hβ, Hγ and He I λ 4471 lines, though less prominently. It extends

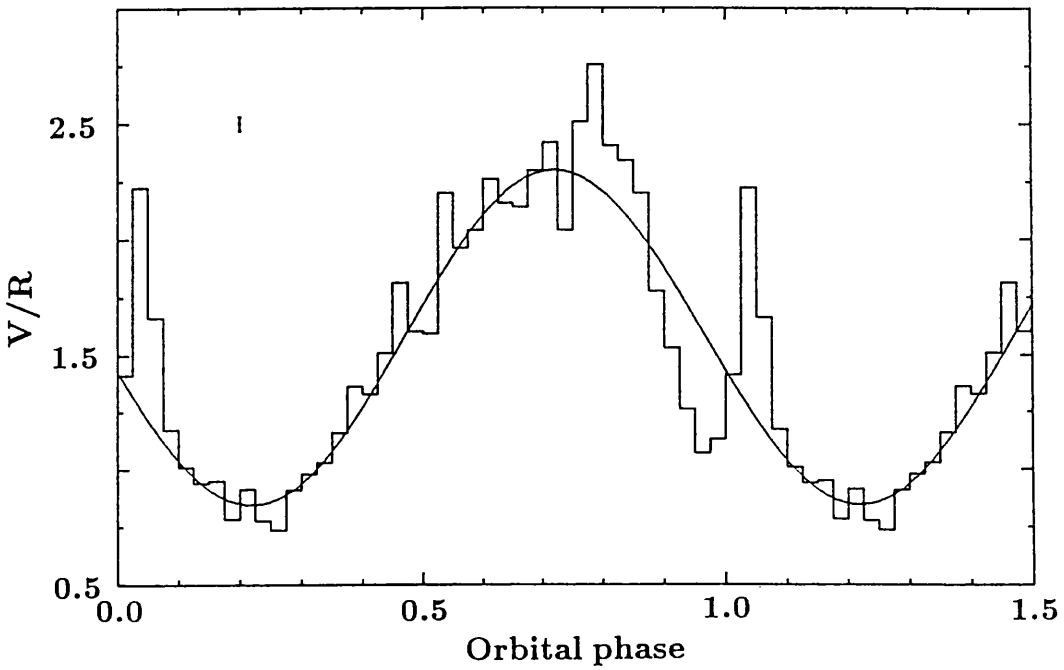

FIGURE 4.4: V/R data for the He II λ4686 line folded on the orbital cycle. I have subtracted the gross effects of the spin modulation from the data before folding; however some residual effects remain resulting in scatter greater than the photon noise error bar shown. The dominant sinusoidal modulation is caused by the S-wave component of the line — to guide the eye we show a sine wave fitted to the data, excluding the phase region 0.9 to 1.1. The rotational disturbance is prominent near photometric orbital minimum (phase 0.0). Note that as the V/R ratio is calculated about the rest wavelength, not the line centroid, the mean value is not 1.

for ~ 0.15 in phase and is centered at phase 0.025 ± 0.010 (the 2σ ephemeris error is 0.013 in phase, Mukai, private communication).

This feature, known as a 'rotational disturbance', is commonly seen in eclipsing cataclysmic variables and is interpreted as an eclipse of the accretion disc. The approaching side of the disc is eclipsed first, causing a diminution of the blue wing of the line profiles, and then the receding side is eclipsed, diminishing the red wing. This can be seen clearly in the profiles of the λ4686 line in FO Aqr; those through eclipse are shown in Fig. 4.5. The line profiles also show that the S-wave emission is eclipsed along with the disc. This contributes to a total reduction of $\sim 40\%$ in the λ4686 line flux during eclipse. A similar rotational disturbance is seen in the other eclipsing intermediate polars, EX Hya (see Hellier *et al.* 1987, Chapter 2) and DQ Her (Young & Schneider 1980; Greenstein & Kraft 1959). For many examples among non-magnetic eclipsing CVs see

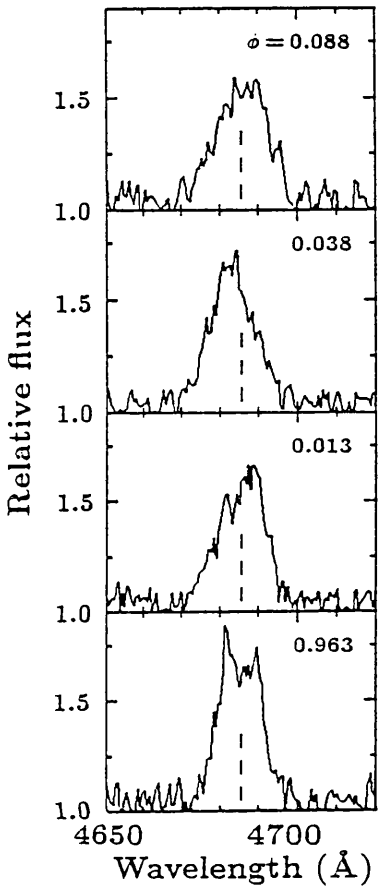

FIGURE 4.5: Profiles of the He II λ 4686 line around eclipse (inset numbers give orbital phase; time increases upward). The data are shown relative to the continuum level. Note the rapid change from diminished blue wing to diminished red wing between the second and third profile. The dashes indicate the rest wavelength.

Honeycutt, Kaitchuck & Schlegel (1987). I am not aware of any reports of similar features in confirmed non-eclipsing low inclination systems.

The S-waves

To investigate the line behaviour further, I show (Fig. 4.6) greyscale representations of the line profiles when folded on the orbital period. The phase-binned profiles are shown in Fig. 4.7. The differences between the line profiles is now clear. The He II λ 4686 line is dominated by an emission S-wave while the He I λ 4471 line and the Balmer lines show an S-wave in *absorption*. In the He I λ 4471 line the absorption extends below the continuum at many phases. Both the emission and absorption S-waves have similar semi-amplitudes (260 km s^{-1}) and widths (350 km s^{-1} FWHM) but show marked differences in other pa-

TABLE 4.1: FO Aqr orbital S-wave parameters

	He II λ4686	He I λ4471	Hβ	Hγ	
Type	Emission	Absorption	Absorption	Absorption	
γ	−20	−180	−230	−220	$\pm$40 km s^{-1}
K	250	250	270	280	$\pm$30 km s^{-1}
FWHM	350	320	310	340	$\pm$40 km s^{-1}
$\phi_{\rm blue}$	0.70	0.45	0.46	0.48	$\pm$0.03

rameters. The emission S-wave in He II λ4686 is phased with maximum blue-shift at orbital phase 0.70, while in the other lines the absorption S-wave has maximum blue-shift at phase 0.45. The emission S-wave has a mean (γ) velocity of −20 km s^{-1} and is approximately centered on the underlying emission line. In contrast, the absorption S-waves have a γ velocity of −200 km s^{-1}, being centered substantially to the blue of the underlying emission line. This results in the redness of the phase averaged Balmer and He I emission lines in the summed spectrum (Fig. 4.1). The measured parameters of the S-waves are listed in Table 4.1. In the He I λ4471 and Balmer lines, the emission appears stronger or the absorption weaker at places where the emission S-wave in He II λ4686 occurs. Therefore, these lines may also contain a similar emission S-wave although of less prominence than in He II λ4686.

The orbital velocity of the primary

In the study of CVs a standard technique is to measure the radial velocity modulation of the emission lines with the orbital period in the hope that it reflects the primary's orbital velocity (K_1). This requires that the emission region be axisymmetric about the primary, so it is necessary to exclude regions of the line contaminated be non-axisymmetric features such as S-waves. Thus, standard practice is to include only the line wings, which originate in high velocity material nearest the white dwarf, in measuring the line velocity.

Mateo (1985) measured a K_1 value in FO Aqr of 75 ± 17 km s^{-1} from the He II λ4686 line further than 400 km s^{-1} from the line center, and Shafter & Targan (1982) found 60 km s^{-1} measuring up to half height in the Balmer lines. My data show, however, that these values are unlikely to be true estimates of the orbital velocity of the white dwarf.

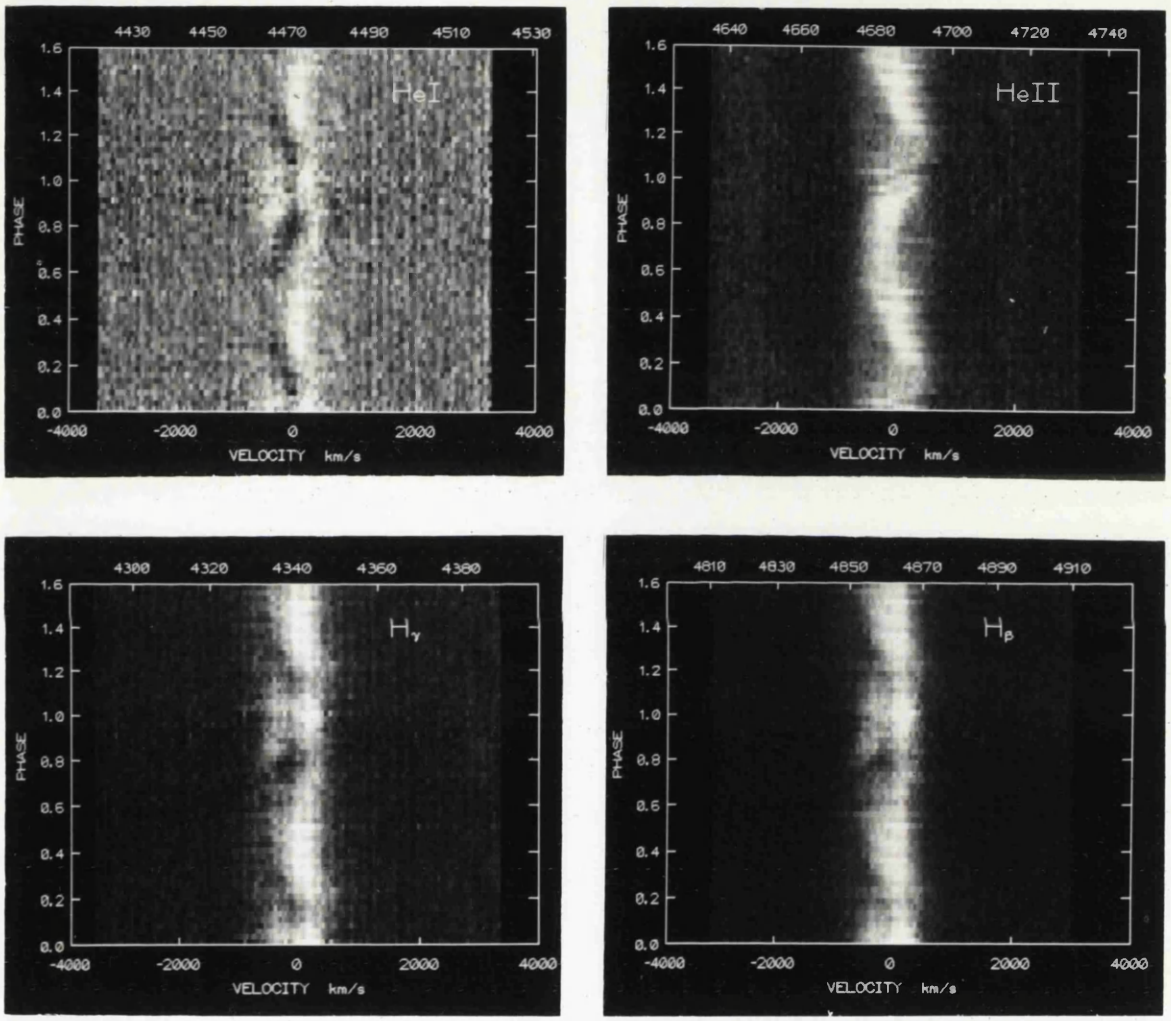

FIGURE 4.6: Greyscale representations of the line profiles in FO Aqr folded on the orbital period. The He I λ 4471 and Balmer lines show a blue-shifted absorption S-wave while the He II λ 4686 line shows an emission S-wave. Note the 'rotational disturbance' just after phase 1, most visible in the He II λ 4686 line. The phasing accords to the ephemeris of Osborne & Mukai (1989).

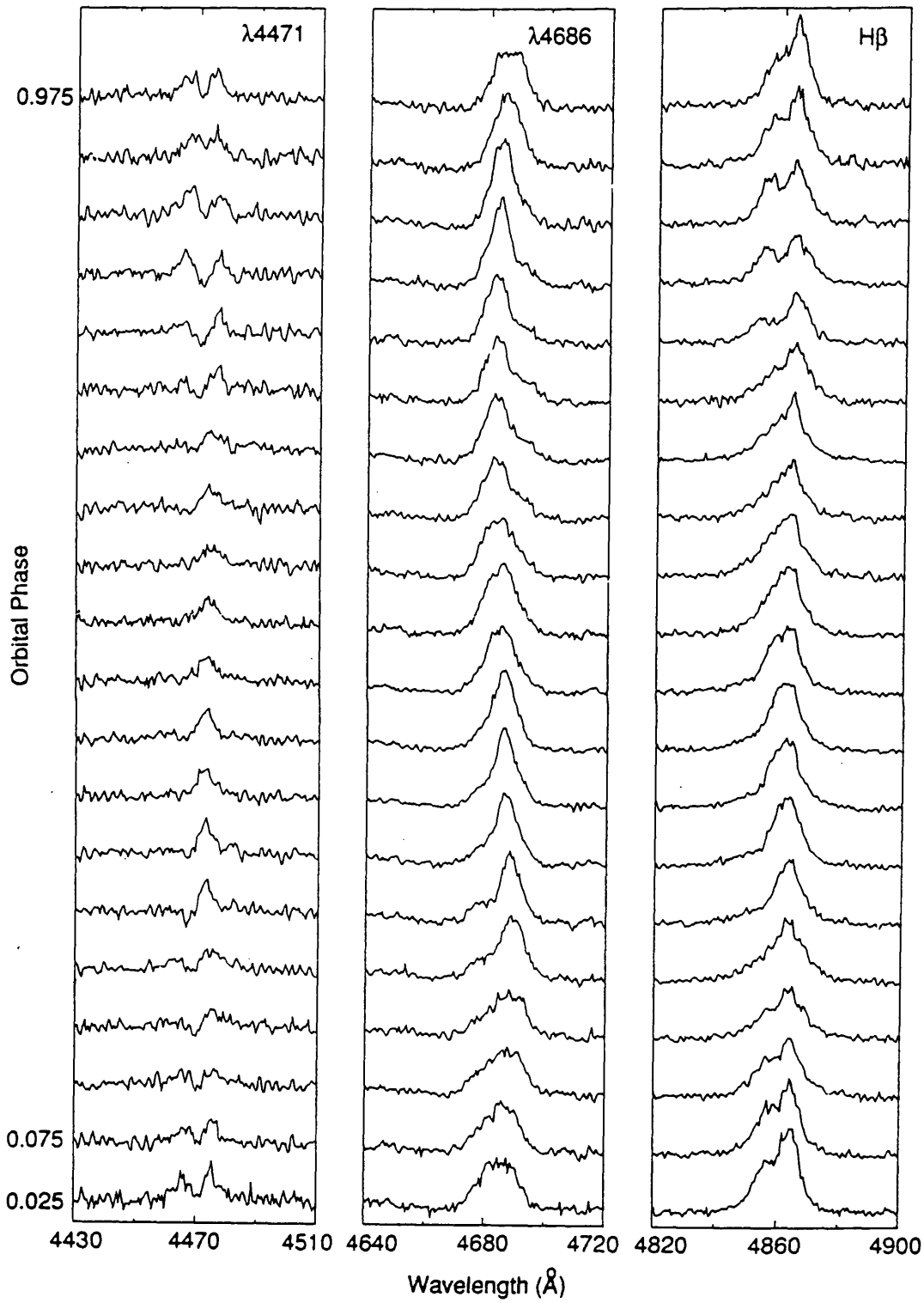

FIGURE 4.7: The phase-binned line profiles from the He I λ 4471, He II λ 4686, and Hβ lines for comparison of the orbital cycle *S*-waves. All data have been normalized to the continuum level.

In the He II λ4686 line, the full width of the emission S-wave ($\sim$800 km s^{-1}) combined with its velocity amplitude (250 km s^{-1}) means that at the phases of maximum red or blue shift it extends to the full extent of the line wings (Fig. 4.6). The red and blue wings of the He II λ4686 line are also affected by, respectively, the nearby He I λ4921 line and C III/N III λ4640–4650 blend (Fig. 4.1). In the Balmer lines the position is as bad. No part of the blue wing is free of contamination from the blue-shifted absorption S-wave. In addition the profiles of all the lines near eclipse will be distorted and so unusable for a radial velocity measurement.

In the He II λ4686 line the blue wing is dominated by the flux due to the S-wave at phases 0.5–0.8 and the red wing similarly contains S-wave flux at phases 0.1–0.3 (Fig. 4.6). Although, at these phases, the S-wave flux extends as far as the line wing can be traced, the underlying component can be seen at other phases. There is some evidence that this is varying in velocity with the phasing expected from orbital (K_1) motion. The flux in the underlying component is strong at phase 0.25 in the blue wing and phase 0.75 in the red wing. Between these regions and the phase regions containing the S-wave there is slight evidence that the lines are less broad (phases 0.4 and 0.9 in both wings, most prominent at phase 0.9 in the blue wing). Thus the line may consist of a base component varying with the orbital motion (maximum red at phase 0.75) together with the S-wave (maximum red at phase 0.20) superimposed.

It is clear, therefore, that measuring K_1 using the standard technique of fitting the line wings is not appropriate and that previously published estimates are probably incorrect. In an attempt to measure K_1 I have fitted the phase binned line profiles with the sum of two Gaussians — one representing the S-wave component and the other the underlying base component. I found, however, that the decomposition into two Gaussians was not unique. At one extreme, one Gaussian modelled the entire base of both S-wave and underlying components while the other Gaussian modelled the top of the S-wave. At the other extreme, the first Gaussian modelled both the base and top of the S-wave and the other Gaussian modelled the base emission to its side. Both extremes, and intermediate decompositions, gave very similar residuals and I could not distinguish between them by the quality of fit. The different decompositions do, however, yield very different velocity modulations of the base component, ranging from 20 km s^{-1} at the first extreme to 400 km s^{-1} at the other. Thus, there is virtually no constraint on K_1. For a system containing a $1M_\odot$ white dwarf together with a secondary of mass $0.48M_\odot$ (for a 4.85 hr binary, Patterson 1984) observed at an inclination of 70° (to produce the eclipse, see discussion), the expected orbital motion, K_1, is 125 km s^{-1}. Such a value is consistent with the data.

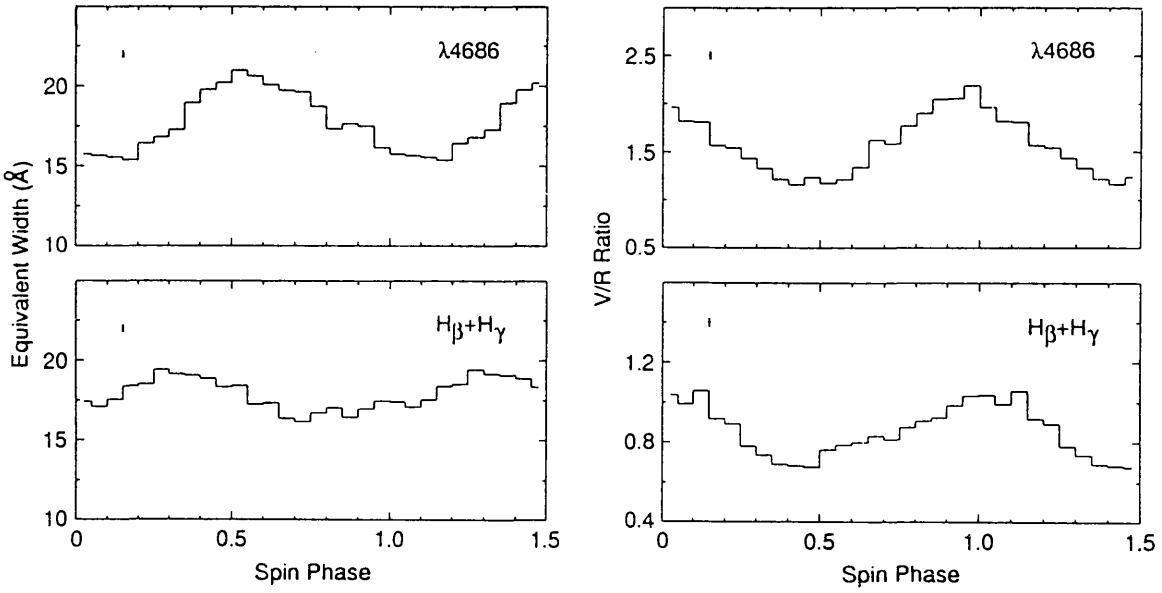

FIGURE 4.8: The equivalent widths and V/R ratios folded on the spin period. The upper panels show data from the He II λ 4686 line and the lower panels the sum of data from Hβ and Hγ.

4.3.3 SPIN PERIOD PHENOMENA

Fig. 4.8 shows the equivalent widths and V/R ratios of the emission lines folded on the 20.9-min spin cycle and Fig. 4.9 shows the line profiles folded on this period. When folding the line profiles on the spin period the variations from the other periods smear out into an average profile. In particular the effect of the orbital absorption S-wave produces a mean profile with a much larger red peak than blue peak. To enhance the spin period profile changes relative to this mean profile I have subtracted the phase averaged line profile from the data. Thus Fig. 4.9 also shows the spin period deviations from the mean profile, apparent absorption and emission being relative to this mean.

The equivalent widths of the lines are modulated sinusoidally, phased with maximum intensity at phase 0.6 for the He II λ 4686 line and at 0.3 for the Balmer lines (phase 0.0 corresponds to photometric maximum). From the line profiles it is seen that the equivalent width variation is largely confined to the low velocity center of the line.

The V/R ratio in all lines shows a quasi-sinusoidal modulation on the spin cycle phased with maximum blueness near phase 0.0 (photometric maximum). This variation is caused by a spin cycle S-wave feature in the line profiles. In Fig. 4.9 this is most easily seen when at maximum blue-shift (phase 1.0) and also as a red wing near phase 0.5. The feature can be traced for ± 1200 km s^{-1} from bluest to reddest extent.

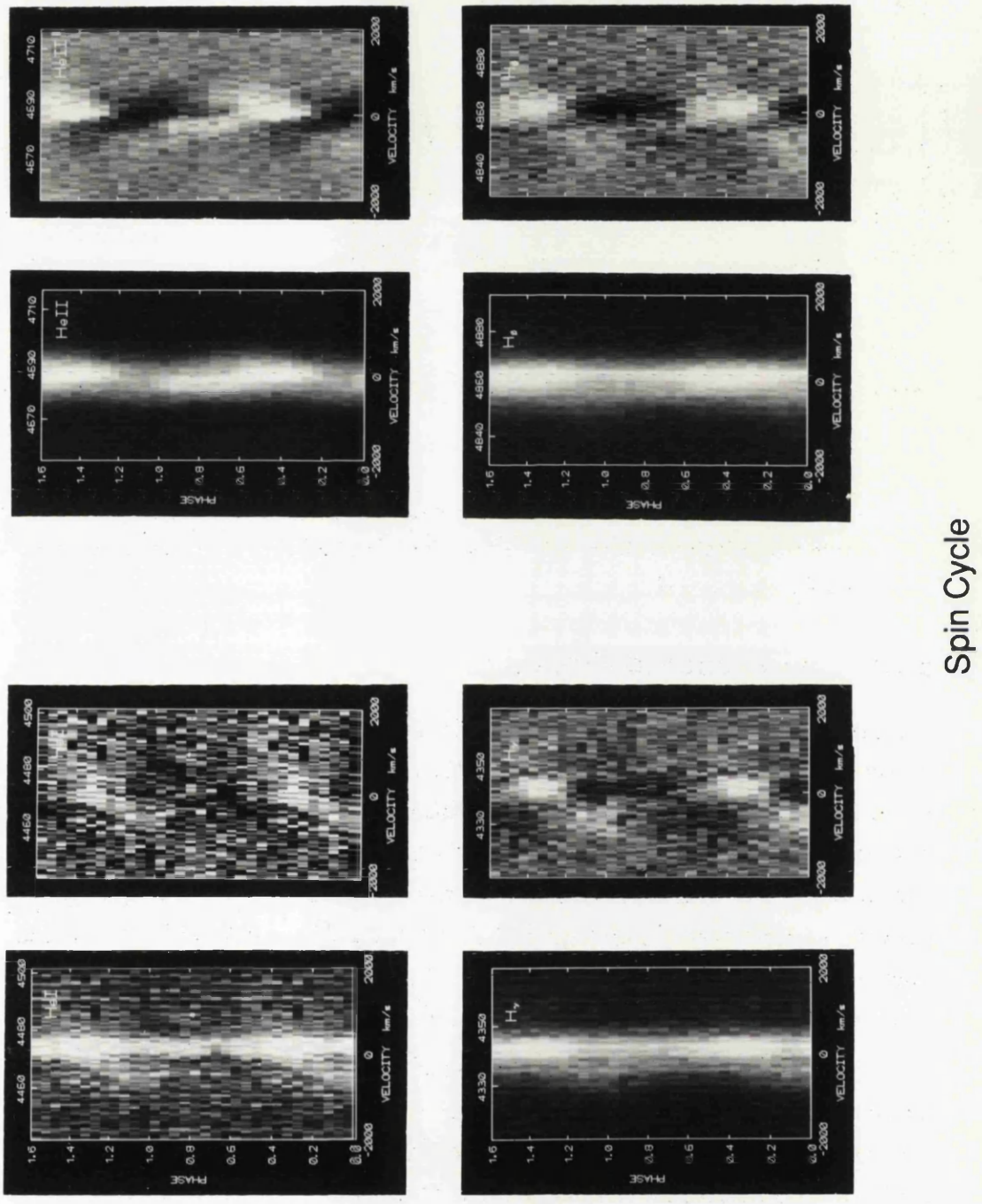

FIGURE 4.9: Greyscale representations of the line profiles in FO Aqr folded on the spin cycle. For each line I show (left) the raw image, and (right) the image when the mean line profile has been subtracted from the data. This is to enhance the relative changes in the emission lines and remove the effect of smeared out orbital cycle variations. Note the high velocity *S*-wave feature in all lines, phased with maximum blue-shift at phase 1. The phasing accords to the quadratic ephemeris of Osborne & Mukai (1989).

4.3.4 Beat period phenomena

The Fourier transforms (Fig. 4.2) show significant modulation of the He II λ4686 line equivalent width at the beat periods, 22.5-min ($\omega - \Omega$) and 19.5-min ($\omega + \Omega$). The V/R ratio of this line varies at the 22.5-min ($\omega - \Omega$) and 24.4-min ($\omega - 2\Omega$) periods. Similar peaks in the Fourier transforms of the Balmer line data are marginally significant. Fig. 4.10 shows the equivalent widths and V/R ratios of the He II λ4686 line folded on the beat periods while Fig. 4.11 shows greyscale representations of the line profiles. Again, to enhance the variations, I have subtracted the mean line profile. In folding the data I have phased the beat periods so that they are in phase with the spin period at orbital phase 0.0. The most prominent variation is a modulation of equivalent width on the 22.5-min period, phased with maximum just after phase 1.0. The V/R data folded on this period show a small variation with a rapid reddening of the line at phase 0.5 and a slow return to the blue throughout the rest of the cycle. The non-sinusoidal nature of this variation contributes to the low level of the peak in the Fourier transform of the V/R data on this period. Folded on the 19.5-min period, the equivalent width shows an increase between phases 0.7–1.1 while the V/R ratio is virtually constant — in keeping with the absence of a peak in the Fourier transform at this period. There is, however, a variation of the V/R ratio with the 24.4-min period consisting of a roughly sinusoidal variation with maximum blue-shift at phase 0.75.

4.4 Discussion

4.4.1 The eclipse

It is obviously important to consider why a photometric eclipse corresponding to the spectroscopic eclipse has not been reported in FO Aqr. Inspection of typical light curves (Fig. 4.12) shows them to be dominated by the 20.9-min spin modulation which has a timescale similar to that of the spectroscopic eclipse and whose profile is variable and suffers flickering. A shallow eclipse would thus be manifest as a distortion of the spin pulse profile at orbital minimum. Such an effect may have been overlooked, especially if the incorrect orbital period (4.03 hour) had been used. I have gathered in Fig. 4.12 published light curves of FO Aqr which contain an orbital minimum. Also included is the spectroscopic light curve from the 5th August (the conditions on the other two nights were not photometric). These show that at the expected eclipse phase the spin pulse is indeed abnormal with a count-rate $\sim 25\%$ below that expected.

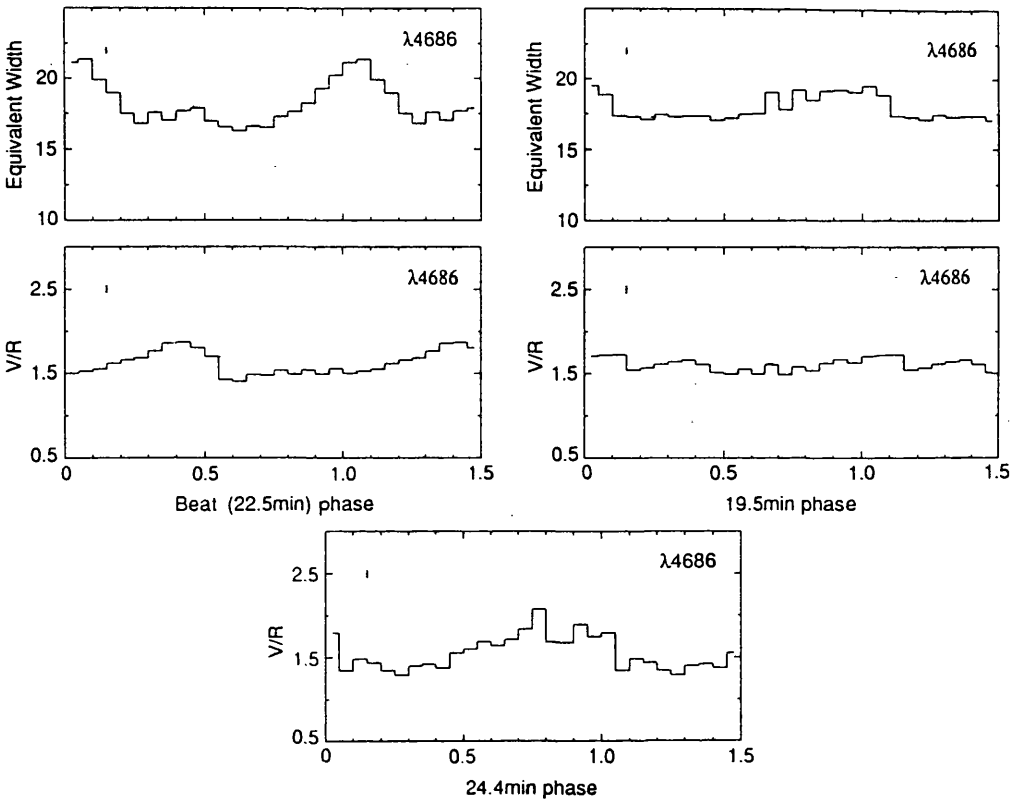

FIGURE 4.10: The equivalent widths and V/R ratios from the He II λ 4686 line folded on the beat periods. The phase convention is that the beat phase is equal to the spin phase at orbital phase 0.

The *EXOSAT* X-ray light curves (Chiappetti *et al.* 1988) contain two times of orbital minimum but show no substantial evidence for an eclipse, although because FO Aqr is a weak (2 cts s^{-1}) and variable source, a narrow (< 5 mins) eclipse could be overlooked. An earlier *EXOSAT* observation (Cook, Watson & McHardy 1984) did not cover the eclipse phase.

I suggest that in FO Aqr the secondary eclipses only the near side of the accretion disc, which projects below the primary, with the central regions remaining uneclipsed. Thus the X-ray band is unaffected, the continuum flux is partially eclipsed, and the line emission (little of which originates in the central regions as shown by the comparative narrowness of the lines) is affected most. An eclipse of this region of the disc would include the impact region of the mass transfer stream with the disc thus explaining the eclipse of the *S*-wave (seen in Fig. 4.5). The asymmetry caused by the position of the impact region could produce small phase shifts between the rotational disturbance, the orbital sinusoidal minimum and photometric manifestations of the eclipse; such phase shifts would be a fraction of the extent of the rotational disturbance (~ 0.15).

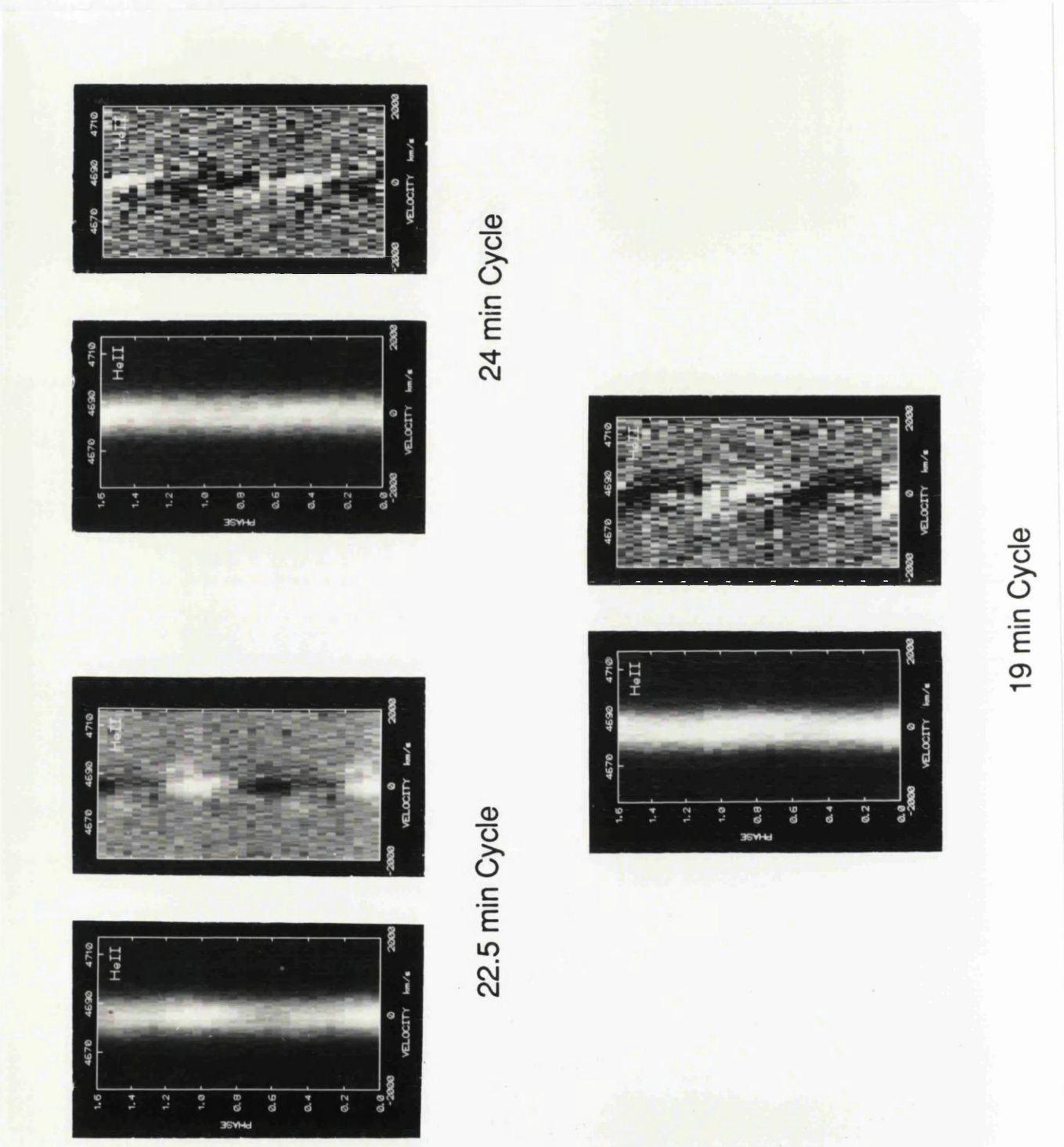

FIGURE 4.11: Greyscale representations of the He II λ 4686 line profiles folded on the three beat periods detected in the data. Again I show both the raw profile and to its right the image with the phase averaged profile subtracted to enhance the variations. The phasing is such that the beat and spin phases are equal at orbital phase 0.

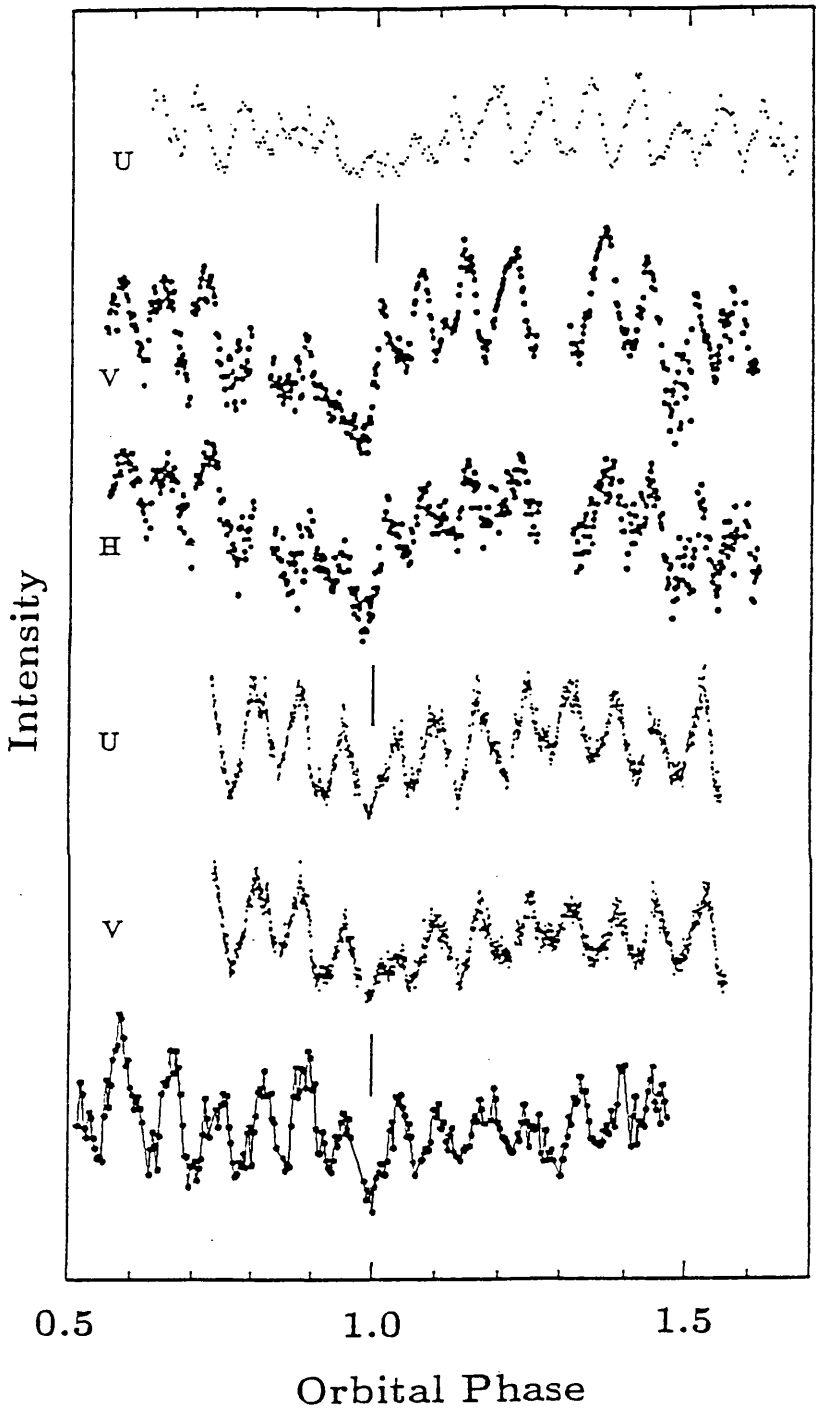

FIGURE 4.12: Previously published light curves of FO Aqr around orbital minimum and a spectroscopic curve from my data. On top of the smooth orbital modulation there is evidence that the 20.9-min modulation profiles are distorted at phase 1.0, with a lower than expected count rate. The data are from Patterson & Steiner 1983 (top), Berriman *et al.* 1986 (second), Shafter & Macry 1987 (third) and this work (bottom). The last is the countrate through a narrow spectrographic slit taken in photometric conditions. The data are plotted on linear intensity scales and the full amplitude of variability is a factor of ~ 2. Orbital phase is according to the ephemeris of Osborne & Mukai (1988).

To avoid an eclipse of the primary, assuming the Roche-lobe geometry and a main sequence secondary with a mass ($0.48M_{\odot}$) as implied by the orbital period (Patterson 1984), requires an inclination less than 75°. Achieving a rotational disturbance of the observed length places a lower limit on the inclination of $\sim 65°$. Previous measurements of the amplitude of the orbital radial velocity variation of the white dwarf, K_1, have been lower than would be expected from a high inclination system. For instance, Shafter & Targan (1982) found a K_1 value of 60 km s^{-1} (although they considered it 'highly uncertain') while Mateo (1985) measured 75 ± 17 km s^{-1} from the line wings further than 400 km s^{-1} from the line centre. The analysis of Section 4.3.2 shows, however, that even beyond this distance from the line centre there is still an S-wave component in the profiles; indeed it extends to velocities at which the line merges into the continuum. Thus there is no reliable measurement of the orbital velocity of the white dwarf. Additionally, the lack of a detectable 8190Å sodium doublet from the secondary (Friend *et al.* 1988) means that attempts to measure the orbital velocity of the secondary have not been successful.

Patterson's (1984) relationship between the mass and radius of a zero age main sequence secondary together with the orbital period implies a secondary mass of $0.48M_{\odot}$. For this mass, a 70° inclination and the range of white dwarf masses 0.5–1.4 $M_{\odot}$, the observed orbital velocity of the white dwarf lies between 110–165 km s^{-1}; the whole range being consistent with my data.

With the masses given above the measurable extent of the rotational disturbance (~ 0.15 in phase) implies that the eclipsed structure has an angular extent of $\sim 1/2$ the primary's Roche-lobe, although if only the lowest section of the disc were eclipsed the actual disc radius would be greater. This compares with EX Hya where a disc nearly filling the Roche-lobe causes a rotational disturbance extending for ~ 0.3 in phase (Chapter 2). An eclipse in FO Aqr establishes it as the third eclipsing intermediate polar (the others being EX Hya and DQ Her). The eclipse is very valuable in constraining the inclination, mass and geometry of such a system, while the effect of the eclipse on the observed flux locates the position of the emission regions within the system. Further study of the eclipse features in FO Aqr would therefore be very useful.

4.4.2 The orbital variations

I showed in Section 4.3.2 that two orbital S-wave features are evident in the emission lines of FO Aqr. The He II λ4686 line shows a prominent emission S-wave only while the He I λ4471 and Balmer lines are dominated by a γ-shifted absorption S-wave, possibly superimposed on an emission S-wave similar to that seen in the He II λ4686 line.

The emission S-wave

The emission S-wave is phased with maximum red-shift at $\phi_{\rm orb} = 0.20$ ($\phi_{\rm orb} = 0$ corresponds to orbital minimum and eclipse). If the velocity reflects the direction of motion of the disc material then this phasing places the emission region 20° ahead of the secondary in the binary frame. This feature is very similar to S-waves seen in many CVs and widely interpreted to be the result of the impact of the mass transfer stream from the secondary with the outer edge of the disc. At first sight the velocity amplitude of the emission S-wave (250 km s^{-1}) is lower than would be expected. For instance, for a $0.8M_{\odot}$ primary, the observed Keplerian velocity near the outer edge of its Roche lobe ($\sim 6\times10^{10}$cm) would be 400 km s^{-1}. However, as the emission S-wave is nearly anti-phased with the orbital velocity of the primary, its apparant amplitude will be reduced by that of the orbital motion. This is 140 km s^{-1} for a $0.8M_{\odot}$ primary with a $0.48M_{\odot}$ secondary and so, under this assumption the observed and expected S-wave amplitudes are consistent.

One can use the phasing and velocity of the emission S-wave to investigate whether the impact of the gas stream is with the outer edge of an accretion disc or with the magnetosphere of the white dwarf as occurs in the 'discless' model for IPs proposed by Hameury, King & Lasota (1986). In such a model the S-wave motion could either reflect the velocity of the accretion stream or the velocity of co-rotation with the magnetosphere of the white dwarf. The first, however, is ruled out by the phasing of the S-wave. The accretion stream is directed initially 20° ahead of the line of centers and curves towards the primary (Lubow & Shu 1975). Maximum red-shift thus occurs at phase 0.05 at latest, whereas the emission S-wave has maximum red-shift at phase 0.20. If the motion reflected the co-rotation velocity then, firstly, the magnetospheric radius must be small compared to the primary's Roche-lobe, otherwise the velocities would be much greater than observed. Hameury *et al.* quote a typical radius of 1×10^{10}cm at which the co-rotation velocity is 500 km s^{-1}. However, the impact of the accretion stream at this radius would then also be earlier than the observed phasing of the S-wave, being around 70° ahead of the line of centers compared with the observed 20°. I thus prefer a disc filling a large fraction of the primary's Roche-lobe to explain the data. Note, though, that Hameury *et al.* predict discless IPs only for orbital periods shorter than 5 hr and FO Aqr, with a period of 4.85 hr, is close to this boundary.

The absorption S-wave

The absorption S-wave seen in the Balmer and He I lines is harder to explain than the emission S-wave. Most importantly, the γ velocity of this component is shifted by −200

$km\,s^{-1}$ with respect to the emission S-wave measured in the He II λ4686 line and also with respect to the underlying components of the He I and Balmer lines. The line profiles of Shafter & Targan (1982) show evidence of a similar blue-shifted absorption S-wave (although unrecognised as such at the time) which suggests that it is a long lived feature in FO Aqr. As the width of the feature (320 $km\,s^{-1}$ FWHM) is less than the amplitude of the velocity variation (540 $km\,s^{-1}$, full amplitude) the absorbing medium must be localised in the binary frame (extending, at most, around $\sim\frac{1}{3}$ of the binary orbit). It is also clear that there is some absorption present at all phases and that therefore the absorbing medium is viewed back-illuminated at all phases. The absorption is deepest at phases 0.8 and 0.2 and least prominent at phases 0.5 and 1.0 (Fig. 4.6). In the He I λ4471 line the absorption extends below the continuum implying that the back-illumination is, at least partly, a continuum source. The velocity variation is phased with maximum red-shift at $\phi_{\rm orb} = 0.95$. However, one must consider whether the observed variation is distorted by the orbital velocity variation of the primary (as suggested above for the emission S-wave). If this is the case, then, assuming an orbital amplitude of 140 $km\,s^{-1}$, the true variation would be phased with maximum red-shift at $\phi_{\rm orb} = 1.05$. Because of the relative phasings, however, the amplitude of the true variation is only slightly different from the observed value (smaller by 15 $km\,s^{-1}$).

The γ velocity of the absorption S-wave implies that the absorbing material must be travelling out of the plane of the binary towards us. That it varies with the orbital period means that it must be due to effects fixed in the binary frame and not to material funnelled by the magnetic field of the primary star which would cause a variation with the spin period (this results in substantial γ-velocities seen in the lines of AM Her binaries). The localisation in phase of the feature then leads one to associate it with the major asymmetry in the binary frame — the secondary, mass transfer stream and disc impact region. Although it is possible that the accretion stream is diverted out of the plane by the magnetic field of the secondary (as suggested by Barrett, O'Donoghue & Warner 1988 for TV Col), it is difficult to see how the accretion stream could be viewed projected against a bright source at all orbital phases as required. It seems more promising, therefore, to consider the impact region of the stream with the disc and material thrown up over the disc by the impact. Such material would be viewed in front of the luminous regions near the primary, and therefore be well back illuminated, at phase ~ 0.8 when indeed the absorption is deepest. Half a cycle later it could be back illuminated by the impact region itself. One might expect that the material would always be viewed against some section of the disc but least so at extreme red or extreme blue shift when least disc lies along

the line of sight. This plausibly explains why the absorption feature is least prominent at these phases (0.5 and 1.0)

The phasing of the variation, maximum red-shift at phase 0.95 (observed) or 1.05 (allowing for distortion by the primary's orbital velocity) is also consistent with the direction of the mass transfer stream as it impacts the accretion disc. To produce the observed γ and K velocities (using the parameters from the He I λ 4471 line, in which the absorption is best defined) at a system inclination of $\sim 70°$, the material would have to be travelling at around 530 km s^{-1} at an angle of 60° out of the plane. If the observed Keplerian velocity at the edge of the disc is 400 km s^{-1} for an inclination of 70° (Section 4.4.2), the actual velocity will be 425 km s^{-1} and the free-fall velocity at the same radius will be 600 km s^{-1}. Thus the suggested speed of the absorbing material is consistent with that attainable by the gas stream at a radius near the edge of the disc.

I now consider whether the impact of the stream with the disc will result in material directed at the required angle of 60° out of the plane. Although a theoretical consideration of this question is beyond the scope of this work, one can approach it by considering behaviour observed in other systems. Of particular interest is the report by Mason *et al.* (1988) who observed dips in the soft X-ray flux from the dwarf nova U Gem which recurred with the orbital cycle. They concluded that they must be due to absorption in material well above the disc plane ($\sim 3\times10^{10}$cm) extending in phase from 0.5–0.9. Such a height would be attained in approximately 10 mins by material travelling with the velocity suggested above. Similar results have been obtained from observations of the low mass X-ray binaries. X 1822–371 shows material at a height of 1.5×10^{10}cm above the plane centered around phase 0.8 (Chapter 5) while dipping sources such as EXO 0748–676 (Parmar *et al.* 1986) and XB 1916–053 (Smale *et al.* 1988) also show structure at similar elevations. The suggested model for FO Aqr is shown in Fig. 4.13.

The star AC211 (= 4U 2127+11 in M15, Naylor *et al.* 1988) also exhibits anomalous absorption features similar to those in FO Aqr. Here the Balmer and He I λ 4471 lines show absorption profiles with a blue-shift of 150 km s^{-1} and an orbital velocity modulation of 40 km s^{-1}. The He II λ 4686 line is seen in emission and is not blue-shifted while there is evidence for similar un-shifted emission in the red wing of the Balmer profiles. Another similarity with FO Aqr is that the absorption is deepest when near the reddest part of its orbital velocity cycle (Naylor *et al.* 1988). Thus an explanation of the blue-shifted absorption may be applicable to both stars.

Following Naylor *et al.* (1988) one can estimate the amount of material required to produce the absorption feature. They find that a column of 10^{22} electrons cm^{-2} produces

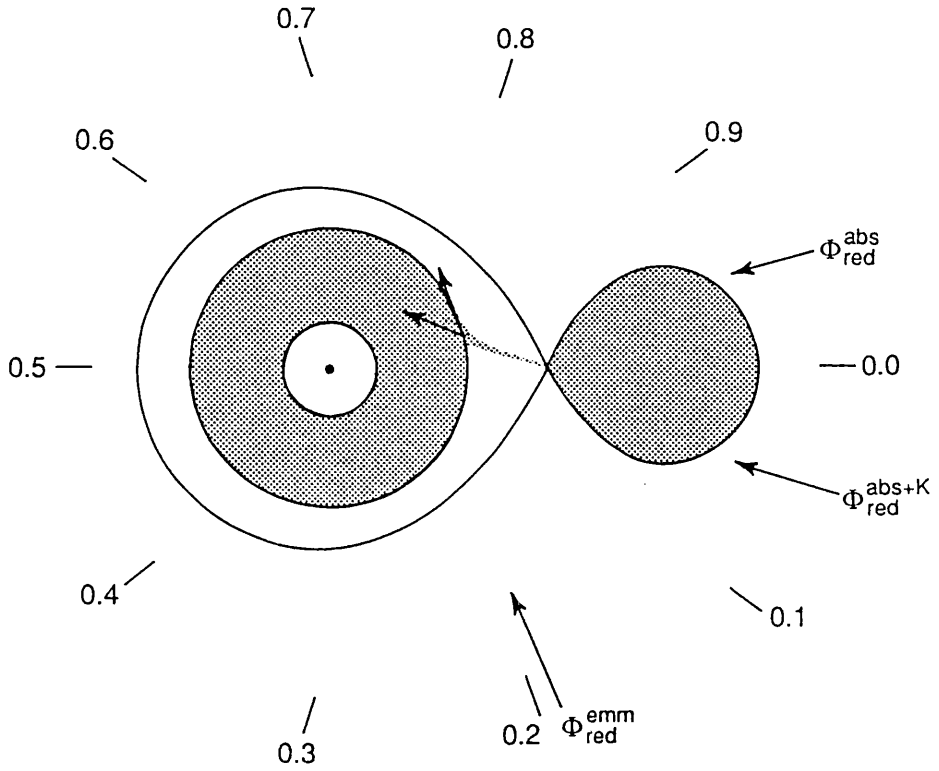

FIGURE 4.13: An illustration of the FO Aqr system. I show the phasings of maximum red-shift of the emission (emm) and absorption (abs) *S*-waves. The latter is shown twice to illustrate the change in phasing when the orbital velocity of the primary is taken into account (abs+K — see text). I also show (arrows) the vectors of the material producing the two *S*-waves in my suggested model. To reproduce the observed γ-velocity the vector representing the absorption *S*-wave is coming out of the plane at an angle of 60°. The figure is scaled for a $1M_{\odot}$ primary and $0.5M_{\odot}$ secondary for which the separation is 11×10^{10}cm. The inner and outer radii of the disc are arbitrary.

an optical depth of ~ 1 in the He I λ4471 line. If the material has a velocity of 440 km s^{-1} normal to the line of sight (as suggested above) and extends for around 3×10^{10} cm laterally, then the flow rate required is 2×10^{16} g s^{-1}. This compares with a probable mass accretion rate of 10^{17}–10^{18} g s^{-1} (Patterson 1984).

4.4.3 SPIN BEHAVIOUR

The V/R ratio variation of the emission lines with the spin period is approximately sinusoidal and phased with maximum blueness near photometric maximum (Section 4.3.3). This results from a spin cycle *S*-wave feature extending for $\pm$ 1200 km s^{-1} in the emission lines. The phasing of the variation implies that at maximum optical brightness the emit-

ting material is streaming towards the observer. Such behaviour was also seen in the line wings of the IP EX Hya by Hellier *et al.* (1987) (Chapter 2). This variation is difficult to understand within a model where the optical spin period modulations in IPs are caused by reprocessing of an X-ray beam by the disc (e.g. Warner 1985). Recent *GINGA* observations of FO Aqr show that the X-ray spin pulse is in phase with the optical pulse (Norton, private communication). In this case, at spin maximum, the X-ray beam would be reprocessing off disc material travelling across the line of sight with no radial velocity. Thus the velocity variation would be phased with maximum blue-shift at phase 0.75 instead of the phase 1.0 observed (see Penning 1985 for a discussion of the reprocessing model).

To explain the phasing of the similar V/R variation in EX Hya, I proposed a model in which the optical modulations are produced by material in the magnetically controlled accretion flow onto the poles of a white dwarf whose magnetic dipole is offset from the spin axis. The varying amount of visible surface area of this optically thick accretion curtain sweeping round with the spin cycle produces the modulation. Maximum surface area is displayed, causing a flux maximum, when the pole points away from the observer. At this phase the material will be flowing towards the observer, down onto the white dwarf, producing blue-shifted emission, as observed. When the pole points towards the observer, we look down the accretion flow and so most of the flux emitted into the line of sight will be re-absorbed by the accretion flow itself, causing a flux minimum. As the flow is directed predominantly away from us at this phase the emission is red-shifted. In parallel with the development of this 'self absorption' model to explain the optical modulations, Rosen, Mason & Córdova (1988) employed the same ideas to explain the X-ray modulations in EX Hya. The similarity of the processes producing both the optical and X-ray modulations then provides a natural explanation for their similar phasings.

The observations of FO Aqr thus provide strong support for the absorption model and suggest its applicability to the IP class as a whole. As well as explaining the phasing of the velocity modulation the model also explains why the spin cycle S-wave in FO Aqr is more prominent when it is bluest than when it is reddest (Fig. 4.9). At spin maximum (bluest) the highest velocity regions closest to the white dwarf will be readily visible. However, at spin minimum (reddest) we look along the accretion pole and the highest velocity regions will be those most obscured. In FO Aqr the spin cycle S-wave is readily visible in the emission lines. In EX Hya, however, it was much less prominent and detectable only by analysis of the line wings. I suggested (Chapter 2) that the low level of the variation in EX Hya resulted from seeing emission from both poles — the two poles then produce oppositely phased S-waves which combine to produce a much lower velocity variation. In

FO Aqr, therefore, the greater prominence of the S-wave probably indicates that we see, predominantly, only one pole.

The remaining structure in the line profile variations on the spin cycle consists of an approximately sinusoidal equivalent width variation. This is phased with maximum equivalent width at $\phi_{\rm spin} = 0.6$ in the He II λ4686 line and at $\phi_{\rm spin} = 0.3$ in the Balmer lines (Section 4.3.3). From Fig. 4.9 it is clear that this variation is largely confined to the center of the line. During the first half of the cycle (phase 0.0–0.5) we observe primarily the leading edge of the accretion curtain while in the later half we observe the trailing edge. It is possible that material swept up by the curtain causes greater line emission on the leading edge thus producing the observed asymmetry. When most readily viewed (around phase 0.25) the material forming the leading edge of the accretion curtain will be flowing across the line of sight thus causing emission concentrated in the line center.

4.4.4 The beat periods

The most prominent beat period seen in the data is that at 22.5-min (spin – orbital frequency or $\omega - \Omega$). This has also been reported photometrically (Patterson & Steiner 1983 and Semeniuk & Kaluzny 1988). Optical modulations at this beat period are commonly seen in IPs and are usually interpreted as the result of reprocessing of X-rays modulated at the spin period by localised material fixed in the binary frame — such as the secondary star or the disc bulge at the region of impact of the accretion stream. The beat periods in my data are most prominent in the He II λ4686 line. This correlates with the emission S-wave from disc bulge also being most prominent in this line and suggests reprocessing by this region.

The variation on the 22.5-min period in the He II λ4686 line (Figs. 4.2, 4.10 & 4.11) is largely an equivalent width modulation with maximum intensity at phase 1.03 ± 0.05. (The phase is defined so that beat period phase = spin period phase at orbital minimum, corresponding to inferior conjunction of the secondary.) The variation is confined to the low velocity centre of the line indicating that it originates in the outer regions of the binary. This line profile change also implies that the equivalent width modulation cannot be the result of continuum changes alone.

That the beat period equivalent width variation is in phase with the spin period variation when looking along the line of centres then implies that the beat period is caused by reprocessing off the secondary star. Note, however, that Osborne & Mukai (1989) placed the *photometric* beat and spin periods in phase at orbital phase 0.8 and therefore concluded that the continuum reprocessing is off the disc bulge. Semeniuk & Kaluzny

(1988) report spin and beat coherence varying between orbital phase 0.5 and 0.75 over several nights, so the reprocessing may be intrinsically variable between different sites. Additional information in FO Aqr comes from the eclipse which is well centered on the sinusoidal orbital minimum ($\phi_{\rm orb} = 0.025 \pm 0.010$). This suggests that a heated secondary is responsible for the orbital photometric variation and that therefore reprocessing from the secondary does occur. In all, then, reprocessing probably occurs from both secondary and disc bulge.

A modulation at the 24.4-min period ($\omega - 2\Omega$) has not been previously reported in FO Aqr. In my data it is significant only in the V/R data from the He II λ4686 line although a marginally significant peak exists at this frequency in the Fourier transform of the equivalent widths. A modulation at the $\omega - 2\Omega$ period is understood to arise from orbital period amplitude modulation of an $\omega - \Omega$ variation (Warner 1986). The visibility of the reprocessing site causing the beat period modulation would be expected to be a function of orbital phase, thus producing the observed period. There is some difficulty, however, in a direct application of this idea to the detection as according to Warner's theory the power at $\omega - 2\Omega$ is at most half that at $\omega - \Omega$ while the peak at $\omega - 2\Omega$ in the Fourier transform of the V/R data is the largest of those at the beat periods. An orbital period velocity modulation of the beat period equivalent width variation is therefore required to produce the observed V/R behaviour. This, however, is also plausible as the reprocessing region would at some orbital phases be blue-shifted and at others red-shifted.

The remaining beat period modulation is that observed in the equivalent width of the He II λ4686 line at 19.5-mins ($\omega + \Omega$). This period has also been seen photometrically (Semeniuk & Kaluzny 1988) and is interpreted as due to orbital period amplitude modulation of the spin variation (Warner 1986). A possible cause is obscuration of the central regions near the primary by non-axisymmetric structure in the binary frame. This could be the secondary star (which eclipses at least part of the disc) or material associated with the disc bulge as discussed in Section 4.4.1. The variation has an equivalent width maximum near phases 0.8–0.9 which are the phases when we see the central regions behind the disc bulge, suggesting that obscuration by these regions is the cause. (Note that as the continuum emission has a larger spin pulse amplitude than the line emission, a reduction in the spin pulse causes a larger equivalent width.) As there is no orbital velocity dependence associated with this obscuration, no V/R variation is expected at the 19.5-min period, in agreement with the observations.

4.5 Conclusions

I have obtained 1000 spectra of FO Aqr at 1-min time resolution and investigated the emission line behaviour at the orbital period, and for the first time in detail, the spin and beat periods. I summarise the findings as follows:

1) There is an eclipse of the accretion flow in FO Aqr which produces a 'rotational disturbance' of the emission line profiles at orbital minimum. Some evidence for the eclipse is seen photometrically, but not in the X-ray band. I suggest that the eclipse is only of the near side of the disc, with the primary remaining uneclipsed. This indicates an inclination in the range 65°–75°, much greater than previously believed.

2) I have discovered an absorption S-wave in the Balmer and He I λ 4471 lines at the orbital period. This is blue-shifted with respect to the line center by 200 km s^{-1}. In the He I λ 4471 line it extends below the level of the continuum. The blue-shift implies that the material responsible for the absorption is travelling out of the plane of the binary towards us. I deduce that the material is thrown up at an angle of 60° to the plane at a velocity of 530 km s^{-1} and I suggest that it may arise as the result of the impact of the stream with the disc.

3) In contrast to the Balmer and He I lines, the He II λ 4686 line displays a typical emission S-wave. The phasing of this emission S-wave suggests that it is caused by the impact of the mass transfer stream with an accretion disc rather than with the magnetosphere of the white dwarf, as occurs in the 'discless' models of Hameury *et al.* (1986).

4) The differences in orbital cycle S-wave behaviour between the He II λ 4686 and Balmer lines result in very different phasings of their velocity variations. This resolves the previous difficulties over the orbital period and the phasing of the spectroscopic conjunctions in FO Aqr (see Patterson 1988 and references therein). The presence of the S-waves also means that I am unable to measure the orbital velocity of the primary. Previous determinations are also probably incorrect.

5) There are variations of the He II λ 4686 line at three beat periods, $\omega - 2\Omega$, $\omega - \Omega$ and $\omega + \Omega$, where ω is the spin frequency and Ω is the orbital frequency. I interpret these as due to reprocessing off the secondary star and the impact region of the stream and disc together with orbital cycle amplitude modulation of the spin and reprocessed variations.

6) The phasing of the spin period velocity variations of the emission lines provides strong support for the model of spin period modulations in intermediate polars developed for EX Hya (Chapter 2). In this model, the photometric variation on the spin period is caused by the changing aspect of the accreting material falling in a curtain to the magnetic pole. The velocity modulation is bluest at photometric maximum. This implies

that at spin maximum the dominant accretion pole points away from the observer so that maximum surface area of the accretion curtain is displayed. The material flows toward the white dwarf with a net velocity towards the observer thus producing the blue-shifted emission. The prominence of the velocity modulation in FO Aqr indicates that we see emission predominantly from only one pole. The data exclude the previously accepted reprocessing model for the optical variations at the spin period. This conclusion has been reached for both EX Hya and FO Aqr which argues for the general applicability of the accretion curtain model to IPs.

CHAPTER 5

EXOSAT observations of X 1822–371

5.1 Introduction

The previous chapters have studied the accretion flows in intermediate polars using time resolved spectroscopy. In this chapter I employ another method of studying accretion flows, this time in the high inclination low mass X-ray binary (LMXB) X 1822–371 (V691 CrA). This system is the prototype of the those thought to possess an 'accretion disc corona' or ADC. The X-ray flux, resulting from the accretion by the compact primary of matter from the low mass companion, is not viewed directly but is scattered into the line of sight by a highly ionised cloud surrounding the primary. Other LMXB of this kind are 2S 0921–630 and 4U 2129+47 (for a discussion of these objects and ADCs see Mason *et al.* 1987 and White & Holt 1982; hereafter WH). X 1822–371 is viewed at high inclination, as evinced by partial eclipses recurring with a 5.6-hr orbital cycle, yet the large effective size of the X-ray source means that the light curve of X 1822–371 is relatively stable and shows little of the rapid variability characteristic of the other class of high inclination LMXB, the dipping sources (see Mason 1986).

White *et al.* 1981 (W81) found that, as well as showing the eclipse, the X-ray light curve of X 1822–371 is modulated quasi-sinusoidally with the orbital period. They proposed that the ADC is partially obscured by the accretion disk, with the profile and height of the obscuring structure varying with orbital phase. A corresponding modulation is seen in the optical band (Mason *et al.* 1980) and also in the infra-red and ultraviolet (Mason & Córdova 1982a, Mason & Córdova 1982b (MC)). Optical spectroscopy has been reported by Cowley, Crampton & Hutchings (1982) and Mason *et al.* (1982).

5.2 Observations

X 1822–371 was observed on four occasions using *EXOSAT*. On the first (1983 day 245) an on-board computer failure caused most of the data to be lost. On 1983, day 280, a complete

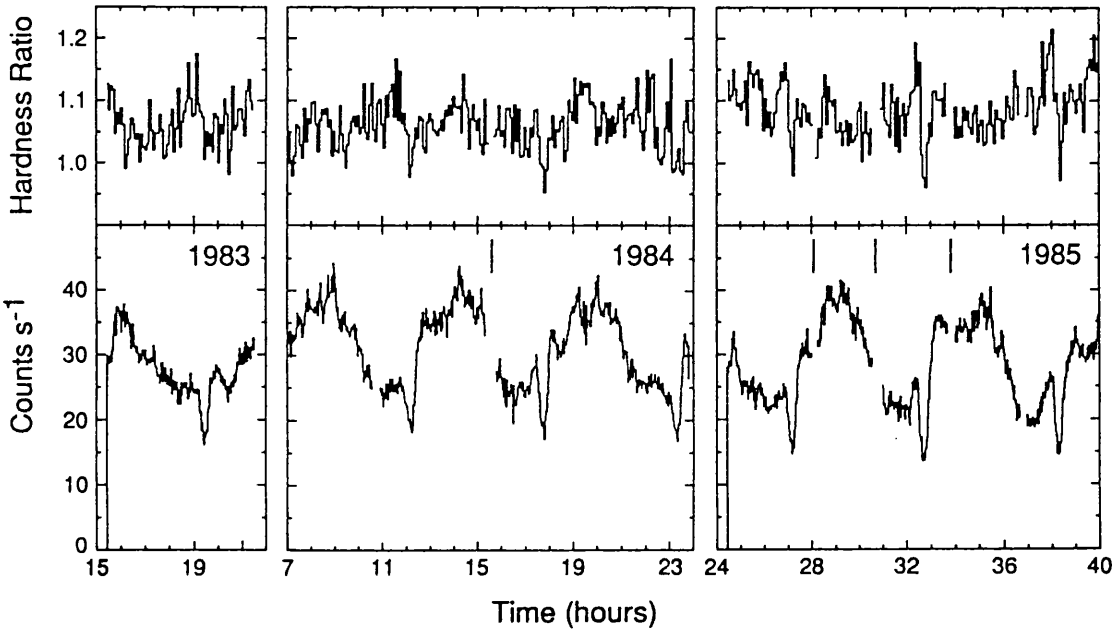

FIGURE 5.1: X-ray light curves of X 1822–371 from the three *EXOSAT* observations using the ME instrument. The tick marks show the times of array half swaps. The upper panel shows the hardness ratio defined as the count rate in the energy range 4.5–8.5 keV divided by that in the range 1.5–4.5 keV.

orbital cycle of coverage was obtained with the LE1, LE2, ME and GSPC instruments (de Korte *et al.* 1981, Turner, Smith & Zimmermann 1981, Peacock *et al.* 1981), with half of the ME array being pointed off-source to monitor the background. This observation suffered from background variations caused by solar activity and the spectral information must be treated with caution. Two further observations in 1984 (day 263) and 1985 (day 126) each spanned three orbital cycles of the source and employed the LE1, ME and GSPC instruments; the on-source and off-source halves of the ME array were alternated during the observation to aid background subtraction for spectral analysis. The X-ray light curves from the ME detector are shown in Fig. 5.1, with the times of array swaps marked.

For comparison with the X-ray data, optical photometry covering 0.85 of an orbital cycle was obtained using the Danish 1.5m telescope and CCD camera at ESO. The observations were made on the $25^{\rm th}$ August 1984 and consisted of 5-min integrations starting at $0^{\rm hr}\,40^{\rm m}$ UT.

5.2.1 THE LIGHT CURVES

The X-ray light curve of X 1822–371 is dominated by a modulation with the orbital (5.57 hr) period (see Fig. 5.1). This can be described as consisting of two components; a

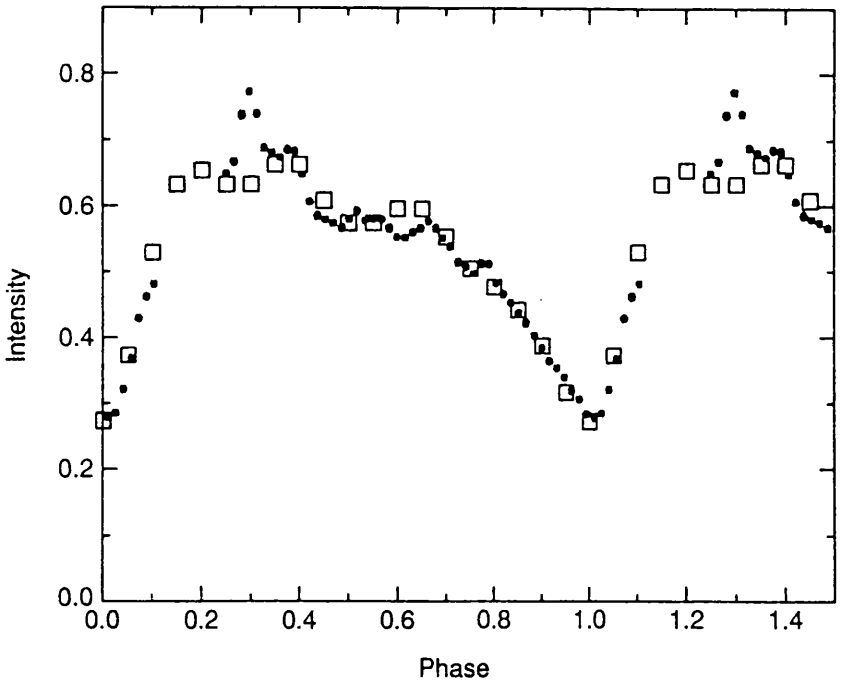

FIGURE 5.2: The optical light curve of X 1822–371 obtained in August 1984 at ESO. For comparison I also show (squares) the optical light curve of Mason *et al.* (1980) which is binned and normalized to my light curve.

dip, lasting about 20 mins, believed to be due to an eclipse by the companion star, and a broader, quasi-sinusoidal variation whose minimum precedes the eclipse minimum by about 0.2 in phase. This modulation remains locked in binary phase while showing small profile changes from cycle to cycle and more substantial changes between observations (see Fig. 5.1 and also W81).

The optical light curve, shown in Fig. 5.2, is substantially the same as that of Mason *et al.* (1980). For comparison I also show their data, binned and normalized to my light curve.

Ephemerides

I determined the mid-times of X-ray eclipse by fitting the data around eclipse with a Gaussian profile together with a linear component; the times are listed in Table 5.1. A linear least squares fit to the eclipse times yields the ephemeris;

$$JD_{\odot} = 2445615.30945(24) + E\,0.23210893(13), \text{ with mean scatter}, \sigma = 3.5 \times 10^{-4}\text{d}$$

Combining the data with further X-ray eclipse times from W81 gives;

$$JD_{\odot} = 2445615.30966(51) + E\,0.23210880(10),\ \sigma = 1.6 \times 10^{-3}\text{d}$$

Comparison of the optical and X-ray eclipse times is complicated by the differing shape of the profiles in the two bands. The optical eclipse is wider than the X-ray eclipse and asymmetric (Figs. 5.1 & 5.2). Consequently, although the optical eclipse times can be made internally consistent by cross-correlating the profiles, it is less easy to define the mid-point of eclipse so that it is comparable to the X-ray timings. I have defined the eclipse time of the optical light curve (Fig. 5.2) as the lowest point of a 5^{th} order polynomial fitted to the eclipse region. I have obtained 6 other optical eclipse times, measured by cross-correlating with this template for consistency; these times are given in Table 5.1 together with previously published data.

There is one simultaneous measurement of an optical and X-ray eclipse (on JD 2445615) which gives eclipse times coincident to within the error bars, the difference being 3.0 ± 3.4 mins. When the optical eclipse residuals are plotted with respect to the above X-ray ephemeris (Fig. 5.3) there is a suggestion of a systematic offset. In the region where I have accurate information on eclipses in both bands (cycle numbers 0–3000) the midpoint of optical eclipse occurs around 3 mins later than that of the X-ray eclipse. This would not be surprising if the X-ray emitting region were centered on the primary while the optical emission were from a non-axisymmetric disc whose flux-weighted centroid did not coincide with the centroid of X-ray emission. I discuss this further in the modelling section. W81 reported a phase shift of 0.04 (13 mins) between the optical and X-ray eclipses, however this is comparable to the error in the ephemeris they used and is not supported by the present data.

I have exploited the longer baseline provided by combining the X-ray and optical eclipse times to investigate whether the orbital period is constant. A quadratic fit to all eclipse times simultaneously yields the ephemeris;

$$JD_{\odot} = 2445615.30905(40) + E\ 0.23210914(16) + E^2\ 5.0 \pm 2.4 \times 10^{-11}, 1\sigma \text{ errors}$$

The quadratic fit has a χ^2_ν of 1.05 compared with 1.51 for a linear fit ($\nu = 29$). The quadratic term has a 99% confidence error of 4.4×10^{-11} and is thus significant at this level. Although the quadratic term is not significant in either of the optical or X-ray data sets alone (due to the shorter base line of the X-ray data and the fewer accurate timings of the optical data) it is not caused by the systematic shift between the two discussed above. The residuals to a linear ephemeris are as large as 9 mins in the most recent epochs compared with the shift of ~ 3 mins suggested by the data where there are accurate timings of both X-ray and optical eclipses. Including a 3 min shift with the optical timings I have measured, which are thus measured consistently, and combining

TABLE 5.1: Eclipse times of X 1822–371.

X-ray eclipses			**Optical eclipses**		
$JD_\odot$	Uncertainty	Ref.	$JD_\odot$	Uncertainty	Ref.
2443413.5266	0.0046	1	2443629.841	0.013	3
2443591.5515	0.0046	1	2444044.845	0.006	3
2443776.5453	0.0023	1	2444090.114	0.008	3
2443778.4059	0.0046	1	2444101.028	0.008	3
2443969.4247	0.0069	1	2444105.665	0.006	3
2444133.5263	0.0034	1	2444106.597	0.006	3
2445580.4932	0.0005	2	2444137.935	0.010	3
2445615.30940	0.00038	2	2444411.132	0.008	4
2445963.00914	0.00033	2	2444412.058	0.008	4
2445963.24046	0.00030	2	2444664.812	0.008	5
2445963.47254	0.00034	2	2444783.894	0.006	4
2446191.63643	0.00031	2	2445579.565	0.003	6
2446191.86768	0.00033	2	2445580.725	0.003	6
2446192.10008	0.00029	2	2445615.3115	0.0020	7
			2445937.7110	0.0021	2
			2446234.5787	0.0018	7
			2447296.4798	0.0011	8
			2447379.3410	0.0010	2

(1) White *et al.* 1981 (2) This work (3) Mason *et al.* 1980 (4) Mason *et al.* 1982 (5) Cowley *et al.* 1982 (6) This work. Observer; Middleditch. (7) This work; Observer; Cropper. (8) This work. Observer; Smale.

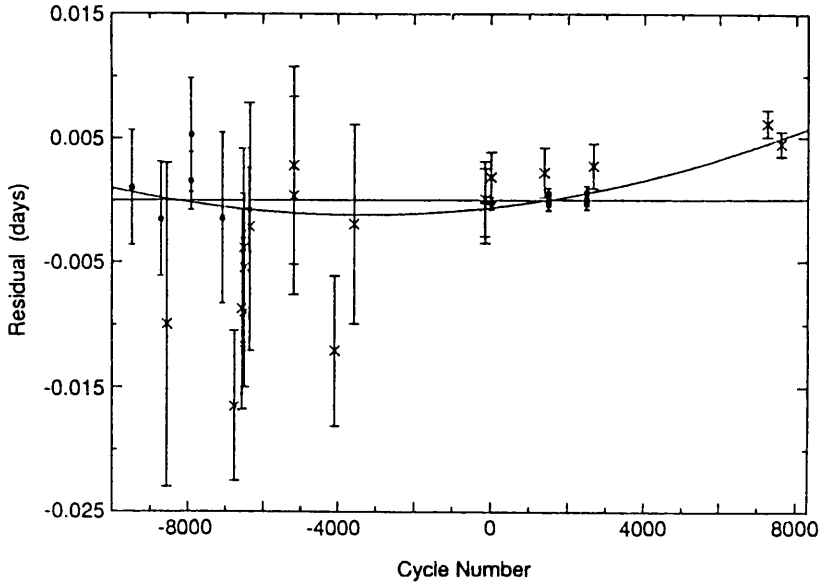

FIGURE 5.3: The residuals to the eclipse timings given in Table 5.1. Filled circles represent X-ray timings and crosses optical timings. The residuals are with respect to a linear ephemeris fitted to the X-ray data only. Also shown is a quadratic ephemeris gained by a simultaneous fit to all data.

these with the X-ray timings gives an E^2 term of $4.1 \pm 3.8 \times 10^{-11}$ (95% error). The quadratic ephemeris is compared with the linear X-ray ephemeris in Fig. 5.3.

5.2.2 X-RAY SPECTRAL ANALYSIS

The dominant sinusoidal modulation in the light curve of X 1822–371 is not accompanied by large spectral changes. Fig. 5.1 shows the light curves from the 1984 and 1985 observations together with the hardness ratio (defined as the ratio of the counts in the 4.5–8.5 keV band to those in the 1.5–4.5 keV band). Correction has been made for the difference in spectral response between the two halves of the ME array. The data from the two energy bands and the hardness ratio are displayed folded in Fig. 5.4. Both observations show a roughly constant hardness ratio throughout the broad modulation and a slight softening of the spectrum during eclipse, also noticed by W81. In addition, in the 1985 observation, a recurrent hardening of the spectrum is seen immediately preceeding the eclipse. This feature is not apparent in the 1984 data.

That spectral changes occur during eclipse is confirmed by measuring the eclipse depth as a function of energy. Table 5.2 gives the eclipse depths, defined as the ratio between the count deficit in a 22 min wide region centered on eclipse and the counts expected from

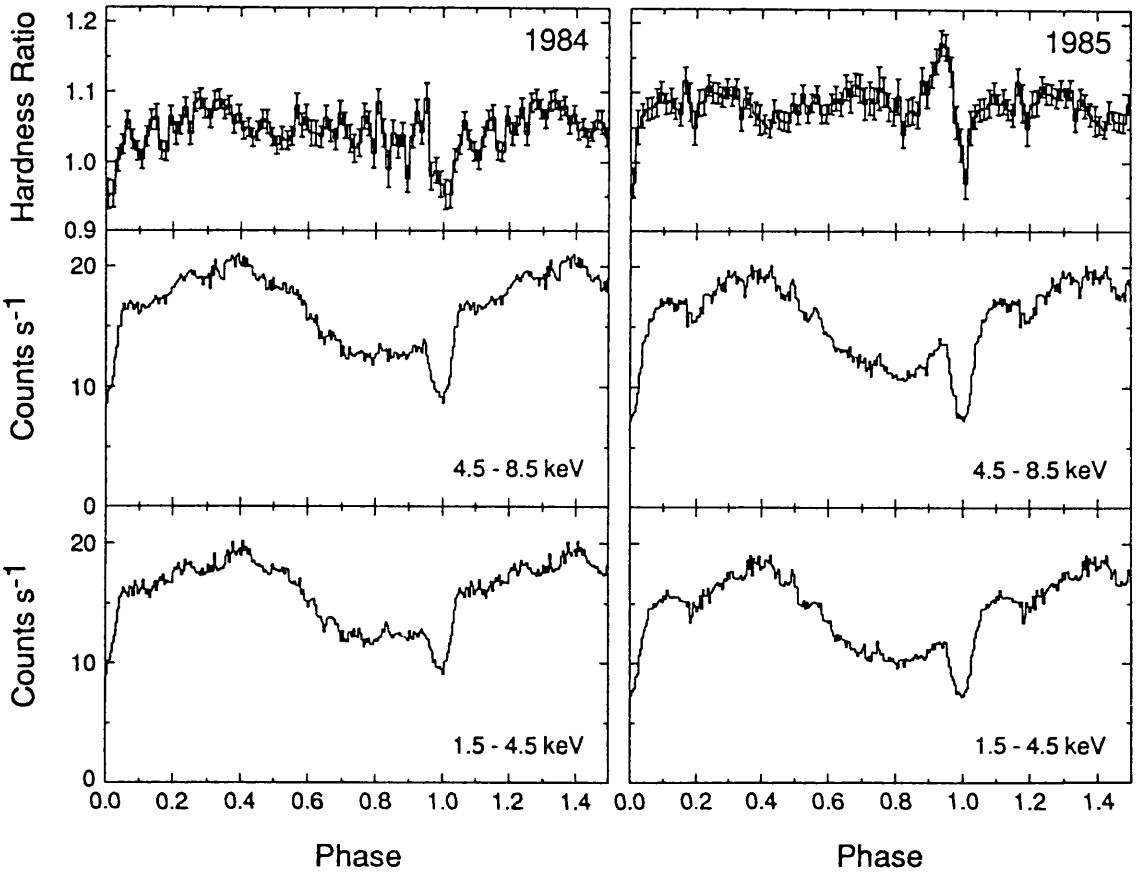

FIGURE 5.4: The X-ray data from the 1984 and 1985 observations folded on the 5.6-hr orbital period. I show the count rate in two energy bands and their ratio.

interpolating linearly between the edges of this region. The data are displayed in graphic form in Fig. 5.5 showing an increasing eclipse depth with energy. In contrast the depth of the sinusoidal modulation (defined as the full amplitude divided by the peak value) remains constant at around 0.44 in all energy bands (Table 5.2).

For detailed spectral analysis of X 1822–371 I divided the observations into phase selected regions and combined the data from the LE and ME instruments. The best single component model fit to these data was a power law; however this yielded a $\chi^2_\nu \sim 7$ and the addition of an iron line at 6.7 keV only reduced it to $\chi^2_\nu \sim 6$. Having tried models with two continuum components, combinations of power laws, black bodies and thermal bremsstrahlung, the only satisfactory representation of the data found consisted of a power law together with a black body component and an iron line; with this model values of $\chi^2_\nu \sim 1$ were achieved.

The results of fitting the phase resolved data were as suggested by the hardness ratios:

TABLE 5.2: Modulation depths as a function of energy.

Energy band (keV)	Eclipse depth	Dip depth
0.1–2	0.14 ± 0.05	0.45 ± 0.03
2–4	0.217 ± 0.006	0.428 ± 0.010
4–6	0.233 ± 0.005	0.420 ± 0.010
6–8	0.252 ± 0.008	0.439 ± 0.012
8–10	0.270 ± 0.016	0.450 ± 0.015

I found that the spectra from all regions of an observation with the exception of the eclipse and, in the case of the 1985 data, the region just before eclipse, could be fit with the same model parameters (allowing the overall normalization to be a free parameter). The parameters fitted to the 1985 data were a power law slope of −0.8, a black body temperature of 1.8 keV, an iron line equivalent width of 270 eV and an absorbing column of 6×10^{20} H atom cm^{-2}; full details are given in Table 5.3. The best parameter values from the 1984 and 1985 data are consistent within the errors.

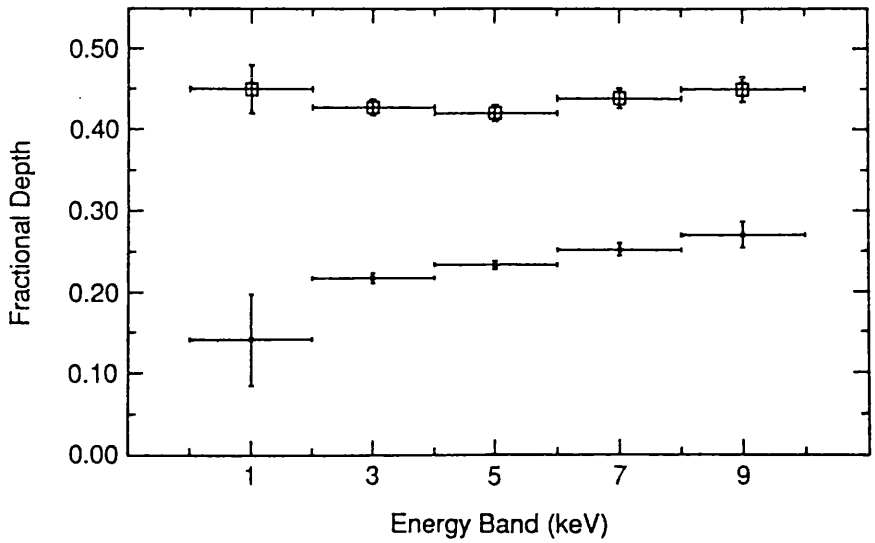

FIGURE 5.5: The open squares give the depth of the sinusoidal modulation as a function of energy. The small circles give the eclipse depth as a function of energy, showing a clear trend to greater depth at higher energies.

TABLE 5.3: Spectral analysis of X1822–371.

1985 Observation		χ^2_ν	Power Law		Black Body		Fe Line	Column
Model	Phase region	ν=25	A($\times 10^{-2}$)	Slope	A($\times 10^{-3}$)	Temp (keV)	EW (eV)	10^{20} cm^{-2}
	0.1–0.3	1.29	1.72	-0.79 ± 0.09	2.28	1.80 ± 0.13	270 ± 60	6 ± 3
	0.3–0.6	1.10	1.81	"	2.38	"	"	"
Fixed	0.6–0.85	0.83	1.09	"	1.72	"	"	"
	0.85–0.95	2.31	1.31	"	1.70	"	"	"
	0.96–1.03	2.24	0.77	"	1.42	"	"	"
Free	0.85–0.95	1.21	1.22	–0.79	1.45	1.99	240	6
Temp	0.96–1.03	0.70	0.81	–0.79	2.02	1.58	440	2
Free	0.85–0.95	1.22	1.04	–0.67	1.85	1.80	260	6
Slope	0.96–1.03	0.77	1.08	–0.99	1.34	1.80	360	4

1984 Observation		χ^2_ν	Power Law		Black Body		Fe Line	Column
Model	Phase region	ν=52	A($\times 10^{-2}$)	Slope	A($\times 10^{-3}$)	Temp (keV)	EW (eV)	10^{20} cm^{-2}
	0.1–0.3	0.89	2.05	-0.93 ± 0.11	1.80	2.03 ± 0.17	190 ± 40	8 ± 4
	0.3–0.6	1.27	2.22	"	2.13	"	"	"
Fixed	0.6–0.85	1.06	1.48	"	1.37	"	"	"
	0.85–0.95	0.93	1.60	"	1.66	"	"	"
	0.96–1.03	1.46	1.43	"	0.85	"	"	"
Free	0.85–0.95	0.92	1.60	–0.93	1.62	2.04	180	7
Temp	0.96–1.03	1.03	1.36	–0.93	1.30	1.79	310	8
Free	0.85–0.95	0.92	1.58	–0.91	1.63	2.03	185	8
Slope	0.96–1.03	1.08	1.53	–1.05	1.01	2.03	260	7

Fitting the parameters derived from phase regions away from eclipse to the regions near eclipse, where the hardness ratio shows departures from the mean, resulted in χ^2_ν values larger by ~ 1. Fitting the 1985 data with the black body temperature a free parameter, it increased to 2.0 keV preceeding eclipse and fell to 1.6 keV during eclipse; alternatively, freeing the power law slope gave values of –0.7 and –1.0 respectively — both alternatives yielded χ^2_ν values similar to those achieved for the other phase regions (~ 1), and I could not distinguish between them. Fitting the 1984 eclipse data required either a fall in black body temperature from 2.0 keV to 1.8 keV, or a change in slope from –0.9 to –1.0.

I show in Fig. 5.6 the average source spectrum from the 1985 observation, excluding regions near eclipse, together with the fitted model. To illustrate the changes during the period preceding eclipse and during the eclipse, I show in the lower panel the residuals of the spectra from these regions with respect to the spectrum in the top panel.

To investigate the 6.7 keV iron line I combined the ME data with those from the Gas Scintillation Proportional Counter which has greater energy resolution. From a summed spectrum of the 1985 observation, the best fit to the data from both detectors simultaneously was obtained using an iron line of FWHM ~ 1 keV, although the range of acceptable values was 0.6–3.0 keV FWHM (90% confidence). The EW values listed in Table 5.3 were measured using a line of FWHM fixed at 1 keV. The data are consistent with a constant equivalent width around the orbital cycle, except during the eclipse where there is a significant increase of around 100 eV (Table 5.3). This increase is consistent with the iron line flux remaining uneclipsed. However, the eclipsed spectrum was fitted with either a different power law slope or black body temperature from the out of eclipse spectra, and equivalent width values are not strictly model independent.

W81 reported an iron line at 6.7 keV with 4 keV FWHM and EW 1090±320 eV compared with my value of 270±60 eV EW with a 1 keV FWHM. They modelled the continuum with a simple power law and if I do likewise, I also see a broad excess centered around 6 keV (with a $\chi^2_\nu \sim 7$). This disappears on addition of the black body component leaving a narrower residual excess centered on 6.7 keV which I have modelled as an iron line (resulting in $\chi^2_\nu \sim 1$).

5.3 Modelling the light curve

White & Holt 1982 (WH) showed how the gross features of the X-ray light curve of X 1822–371 could be reproduced by a model where a central ADC was partially obscured by the outer rim of an opaque accretion disc whose height is a function of azimuthal

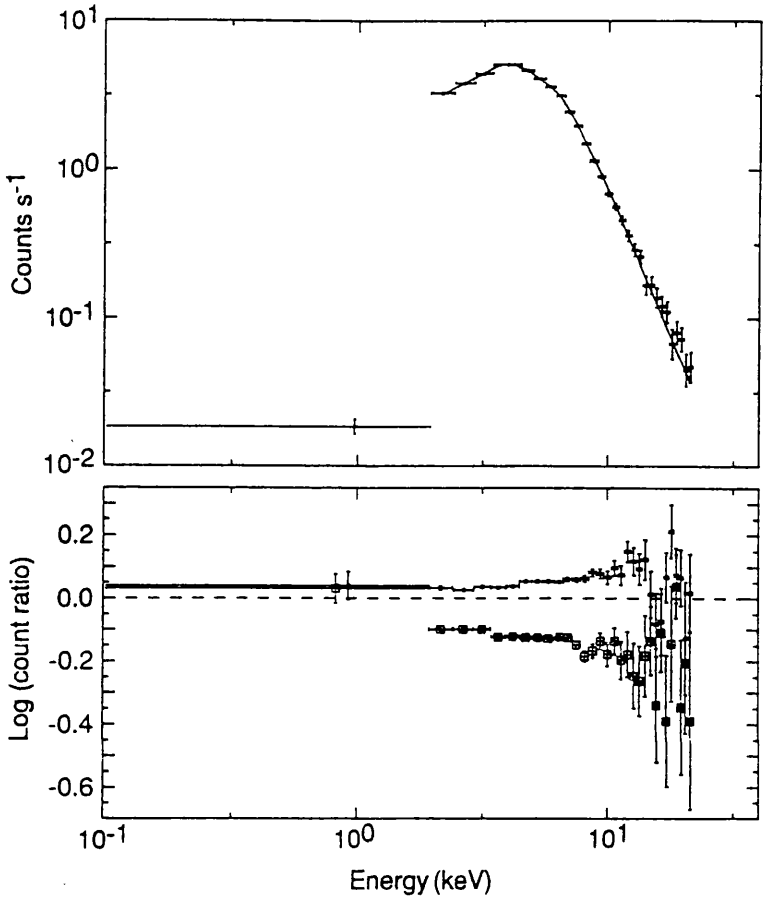

FIGURE 5.6: The upper panel shows the X-ray spectrum from the 1985 observation of X 1822–371 summed from all regions away from eclipse. The fitted model parameters are given in Table 5.3. To illustrate the changes to the spectrum near eclipse the lower panel shows the deviations from this spectrum. The upper data are from the pre-eclipse region and show a harder spectrum. The lower data are from the eclipses and show a softer spectrum.

angle, together with a similar obscuration from the secondary star to produce the eclipse. They arrived at a model consisting of an ADC of radius 2×10^{10}cm and a thin disc of radius 4×10^{10}cm and height 0.2×10^{10}cm on which exist two saw-tooth bulges which have maxima at phases 0.89 and 0.24 and heights 1.5×10^{10}cm and 0.8×10^{10}cm respectively. In the model, the bulges decay linearly downstream over about half the disc circumference.

Mason & Córdova 1982b (MC) showed that the gross features of the optical and UV light curves could be similarly reproduced. They took the bulge profile given by WH and added up the contribution to the light curves expected from the inner and outer surfaces

of the accretion disc (the inner surface being that illuminated directly by X-rays and the outer surface being that shielded from the X-ray source). They also added a constant and a sinusoidal component as would be expected from an illuminated secondary star.

In this chapter I repeat this modelling using the *EXOSAT* data, which unlike that used by WH gives full phase coverage, together with new optical data. I adjust the parameters of the model in order to give the best fit to the X-ray and optical data simultaneously thus investigating how robust the conclusions of WH and MC are.

5.3.1 Modelling the eclipse

I begin by assuming that the system obeys Kepler's law and that the secondary fills its Roche lobe. There is also a value for the orbital velocity of the primary, $K_1 = 70$ km s^{-1} (Mason *et al.* 1982, Cowley *et al.* 1982). As the orbital period is known, the orbital geometry is then a function of the mass of one of the binary components (e.g. M_x, the mass of the compact star) and the system inclination, i, only. For the purposes of the model I assume that the X-ray eclipse is a partial occultation by the secondary of a spherical, uniformly X-ray emitting ADC centered on the primary star and of radius R_c (including any portion visible below the disc). One can thus determine R_c by fitting the eclipse light curve. As shown by WH, R_c is relatively insensitive to reasonable variations in M_x and i. However it is sensitive to variations of the disc rim profile at the relevant phases. The eclipse is not set into a flat region of the light curve which implies that the rim profile is likely to be altered during the model fitting. For this reason I keep R_c as a free parameter throughout the modelling process, although the eclipse data effectively confine it to a narrow range around 3×10^{10}cm. The optical eclipse is approximately twice the width of the X-ray eclipse (Figs. 1 & 2) which leads one to expect that the eclipsed optical emitting region (i.e. the disc) is of radius, $R_d \sim 2R_c$.

5.3.2 Modelling the accretion disc rim

To represent the disc rim profile in a general way the model included a set of nodes each specified by a disc phase angle and a height above the plane of the binary. The rim height at any phase angle was then calculated by a linear interpolation between the nodes on either side. The X-ray flux at any phase in the binary orbit is then calculated by summing over the ADC visible above the disc rim. The code varied both parameters for each node independently in order to minimize the χ^2 of the data with respect to the model over the orbital cycle. The fitting was done using the Marquardt algorithm as encoded by Press *et al.* (1986). I included provision to vary the number of nodes in order to investigate the

increase in fit quality with additional free parameters. For fitting the X-ray light curve, therefore, the free parameters were a phase and a height for each node used to model the disc rim together with M_x, i, R_d, R_c and a normalization parameter.

To obtain a simultaneous fit to the optical light curve I added two more parameters: 1) I assumed that the outer surface of the disc rim emits uniformly and added a normalization parameter for this emission. 2) I assumed that the optical light visible from the inner surface of the disc scales as the projected area between the rim of the rear of the disc and the rim of the front of the disc and added another normalization parameter for this contribution (this corresponds to the sum of components 1 and 2 in MC). Following MC, I also added an optional constant plus sinusoidal component as would be expected from an illuminated secondary.

It is not clear whether one can add in an *a priori* constraint that the disc rim must be of sufficient height, given R_d and i, that the line of sight to the primary star is obscured at all times. If the ADC were sufficiently optically thick this would not be necessary. My code contains a switch allowing for both cases. In the optically thin case the model is constrained to always hide the primary star with the disc rim. In the optically thick case no such restriction is included.

5.3.3 Results

I ran the modelling code using the folded X-ray light curves from the *EXOSAT* observations and the optical light curve. The similarity of the optical curve with that of Mason *et al.* 1980 (which was used by MC in their modelling) suggests that the optical light curve is similar to the X-ray light curve in being relatively stable over several years, and that therefore a simultaneous fit to non simultaneous data in the two wavelength ranges is physically meaningful. The X-ray data were fitted using a constant error bar gained by taking the mean of the deviations from cycle to cycle in the unfolded data when binned at the resolution used for the fitting. The error bars on the optical data were adjusted to equalize the contributions to the χ^2 from the optical and X-ray components during a simultaneous fit. As the best fits resulted in $\chi^2_\nu \sim 1$ the size of the errors indicates the deviation of the models from the light curve. The error bars are displayed with the model fits.

I found that an adequate fit to the 1984 data was achieved using a disc rim parameterized by only two nodes i.e. using only 2 straight lines to draw the profile as a function of phase. Fig. 5.7 shows the fit using this profile where the overall χ^2_ν is 1.45; the fitted parameters are given in Table 5.4. The fit was obtained using the optically thin ADC

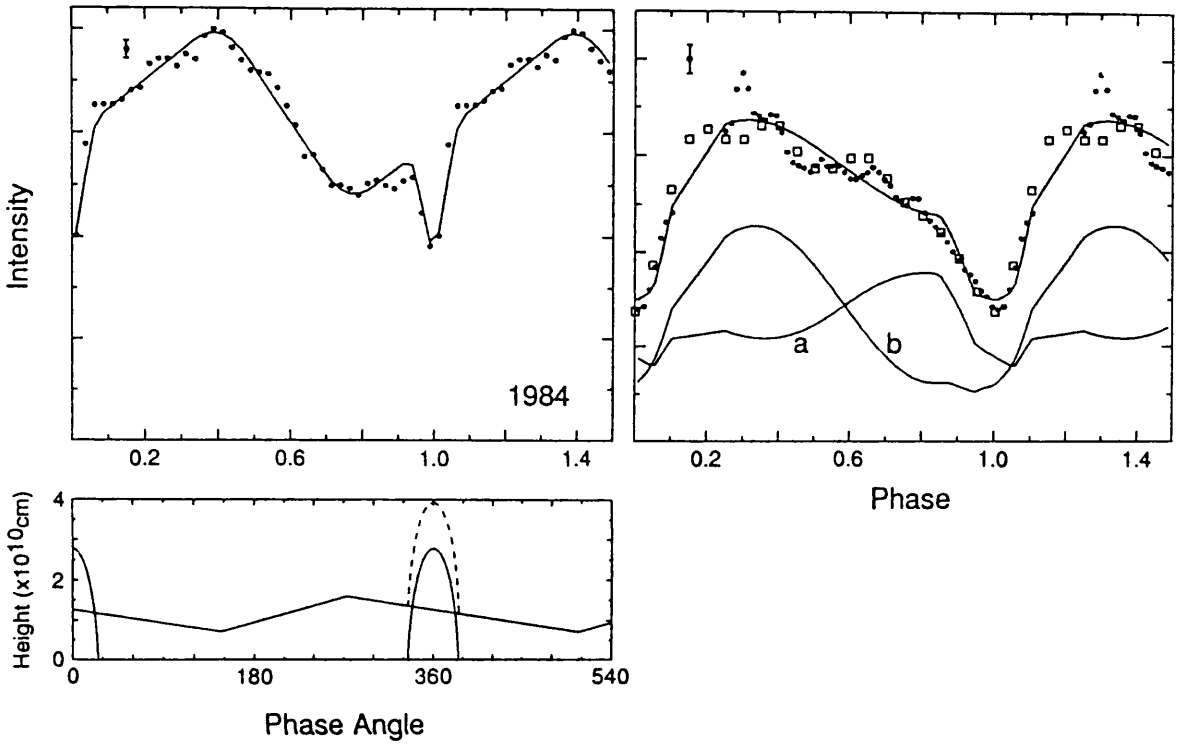

FIGURE 5.7: The result of the model fitting to the 1984 *EXOSAT* data (left panel) and the optical data (right panel) simultaneously. The curves *a* and *b* show the contributions from the inner and outer regions of the accretion disc respectively. Also shown, but not included in the fit, are the data of Mason *et al.* 1980 (squares). The lower panel shows the fitted disc rim profile and the relative sizes of the ADC (dotted) and the secondary. This panel has an expanded vertical axis for clarity. The parameters of the fit are given in Table 5.4.

condition and thus the line of sight to the primary is always obscured. The simultaneous fit to the optical data is displayed together with the optical data of MC (square boxes) which are shown for comparison but not fitted. The two components, from the outer disc and inner disc, contributing to the optical light curve are also shown separately. I found that I could not improve the fit by adding a constant and sinusoidal component. The lower panel to Fig. 5.7 shows the fitted disc rim profile together with the secondary and the fitted ADC (dotted), drawn as it would appear at phase 0.0, for comparison. Note that I have expanded the vertical dimension of this figure for clarity.

A 2 node bulge profile similar to that in Fig. 5.7 is less adequate in fitting the 1985 *EXOSAT* data. These data are displayed in Fig. 5.8. The fainter line shows the fit obtained

TABLE 5.4: X 1822–371 model fitting parameters.

1984 Observation		
$\chi^2_\nu = 1.45\ (\nu = 85)$	$i = 84° \pm 2$	
$M_x = 1.2 \pm 0.4_\odot$	$a = 12.5 \pm 1.5$	$\times 10^{10}$cm
$R_d = 7.2 \pm 0.8$	$R_c = 3.3 \pm 0.3$	$\times 10^{10}$cm
Node phase angles	147, 273	degrees
Node heights	0.71, 1.60	$\times 10^{10}$cm
Inner disc/Outer emissivity	2.4 ± 0.1	
1985 Observation		
$\chi^2_\nu = 0.92\ (\nu = 79)$	$i = 85° \pm 2$	
$M_x = 1.2 \pm 0.4_\odot$	$a = 12.5 \pm 1.5$	$\times 10^{10}$cm
$R_d = 7.3 \pm 0.7$	$R_c = 3.3 \pm 0.3$	$\times 10^{10}$cm
Node phase angles	72,137,245,321,352	degrees
Node heights	0.97,0.57,1.37,1.55,0.75	$\times 10^{10}$cm
Inner disc/Outer emissivity	2.1 ± 0.1	

with a 2 node profile whose χ^2_ν is 1.7. To improve the fit I have added more nodes. The heavier line in Fig. 5.8 shows a fit using 5 nodes while the resultant profile is shown in the lower panel; this yielded a χ^2_ν of 0.92. Using 3 or 4 nodes, the bulge profile is intermediate between the 2 and 5 node cases, with similarly intermediate χ^2_ν values; using more than 5 nodes is not justified by improvements in the fits. Again this 5 node fit was obtained using the optically thin ADC constraint. The overall shape of the profile is similar to the 2 node profile while the extra structure provides a better fit particularly to the regions near eclipse. Note that the model optical light curve is not as sensitive to the increased structure as the X-ray curve. This is because the optical emission is summed from the whole accretion disc whereas the X-ray emission is affected only by that part of the disk projected in front of the ADC. The necessity for a more complex rim profile near phase 0.0 in the 1985 observation may be related to the greater spectral changes in this phase region during this observation (see Section 5.2.2).

As with the 1984 data I found that the optical fit is not improved by adding a constant component and a sinusoidal component. These components were present, however, in the

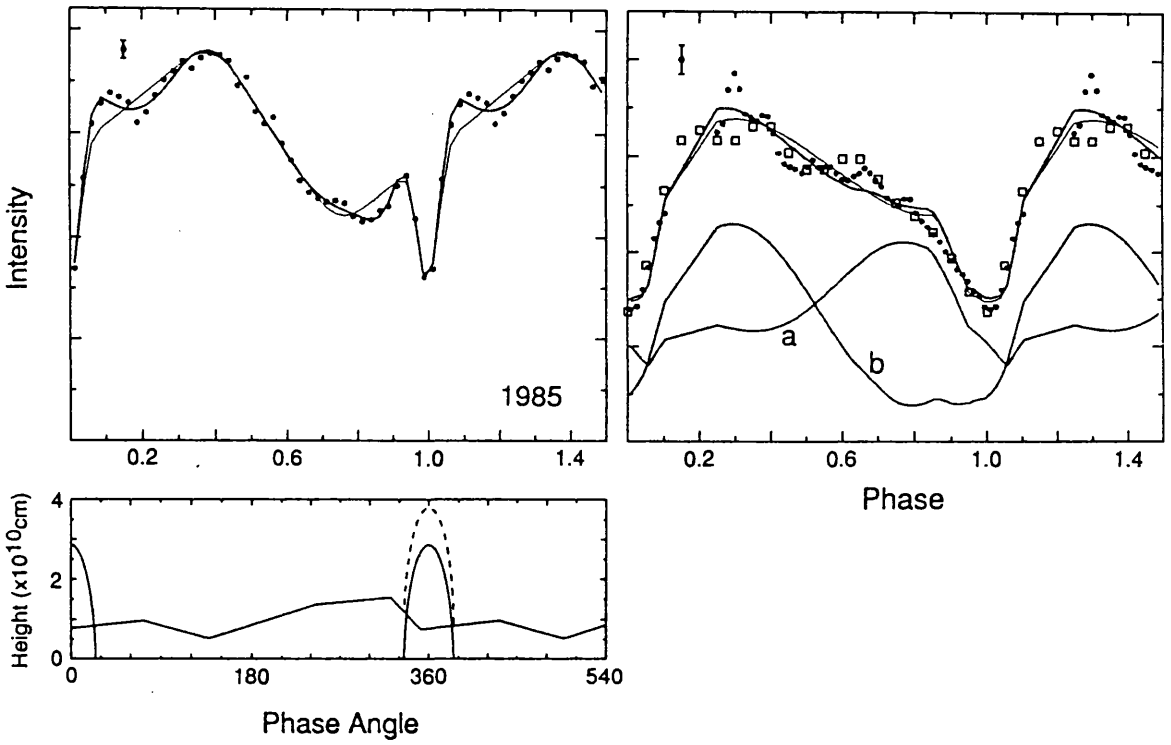

FIGURE 5.8: As for Fig. 5.7 but fitting the 1985 *EXOSAT* data. The lighter line shows a fit using a rim profile similar to that used for the 1984 data. The heavier line results from the more complex profile shown in the lower panel. The parameters of the fit are given in Table 5.4.

fits of MC and I have therefore investigated whether my data exclude their presence. I found that this was not the case and that very similar fits can be obtained with these components contributing up to 30% of the optical light. Thus the result is consistent with that of MC — as would be expected given the similarity of the data. The optical fit produces an eclipse that is slightly shallower than the data and also has trouble reproducing the horizontal region of the light curve between phases 0.5 and 0.7 (Figs. 5.7 & 5.8). I have attempted to improve these features by adding extra free parameters to the model. However, I could not find a simple addition which both improved the optical curve and did not degrade the X-ray fit unacceptably.

I have also fitted the 1984 *EXOSAT* data with a profile similar to the more complicated 5 node profile used for the 1985 data. The improvement is less than with the 1985 data, the resultant χ^2_ν dropping from 1.45 to 1.21.

The derived 5 node disc rim profile (Fig. 5.8) is similar to that of WH, which also

requires 5 straight lines to draw it. A large bulge is centered around phase 0.8 which may be associated with the impact of the accretion stream with the edge of the accretion disk. As in WH's model, a second lesser bulge is present around phase 0.2.

The above fits are at high inclination ($\sim 85°$) and the line of sight to the primary is always obscured by the disc rim. I have investigated the fits obtained without this constraint, allowing the possibility of lower inclinations such as indicated by the modelling of WH and MC ($\sim 80°$). At high inclinations the removal of the constraint makes no difference to the best fits obtained. I have searched for fits at lower inclinations but was unable to find any with χ^2_ν less than 3. Starting the code from the model of WH and allowing it to make small adjustments to the parameters results in a fit to the data with $\chi^2_\nu = 3.2$. I conclude that the overall best fit to the *EXOSAT* data is obtained at high inclinations ($\sim 85°$) where the line of sight to the primary is always obscured. Thus the modelling does not constrain the optical depth of the ADC. Both optically thin and optically thick ADCs result in the same best fit model parameters.

The best model fits are obtained with a disk radius, R_d, about twice the ADC radius, R_c. Frank, King & Lasota (1987) have suggested that the vertical structure occulting the X-rays from the ADC does not lie at the disk rim but is further in, at a similar radius to the ADC, whose radial extent it constrains. A major motivation for this model is to decrease the required height of the occulting structure above the disc plane. If there were still optically emitting material outside the vertical structure then the width of the optical eclipse would not rule out this possibility, although the occulting structure would still be required to reproduce the optical light curve.

In considering this model I have investigated whether the X-ray data alone constrain R_d; I find that reducing the radius of the occulting material worsens the X-ray fit. The critical factor is the ratio of the diameter of the obscuring material to that of the emitting ADC and thus the proportion of obscuring material projected in front of the ADC at any one phase; as the disc structure moves inwards the simulated X-ray light curve becomes a smeared out version of that observed. As the modelling employs a spherical ADC, a high obscuring structure means that only the upper regions, with a smaller effective radius, are visible. Thus, fitting the X-ray data with the radius of obscuring material constrained to be near that of the ADC results in the height of the disc structure above the disc plane being similar to or even greater than that needed when the structure lies further out (which ranges from 0.6 to 1.5×10^{10}cm). Even so, the fit is worse with a best achievable χ^2_ν of ~ 2 compared with ~ 0.9 when fitting the X-ray data alone with $R_d = 2\,R_c$. Maintaining the height of the obscuring material while reducing the radius increases the elevation angle

subtended at the primary star. It is also worth noting that at my inclinations ($\sim 85°$), moving the obscuring material inwards along the line of sight has only a small effect on the absolute height and will in itself increase the height to radius ratio of material which projects above the primary star. Attempts to obtain a fit while forcing the height of the obscuring material to be significantly lower fail as they do not occult a sufficient fraction of the ADC and hence cannot yield the required modulation depth. One is not at liberty to greatly alter the size of the ADC to alleviate this effect as it is heavily constrained by the X-ray eclipse profile. I have modelled the ADC as spherical to minimize the number of parameters. However, I have also tried other shapes but without finding any improvement. Changing to a cylindrical ADC produces marginally poorer fits and does not alter the above results.

When no constraint is applied to R_d then, fitting the X-ray data alone, it adjusts to around $1.9\,R_c$, which is evidence that the X-ray occulting material is located at a similar radius in the system to the outer edge of the optically emitting disc. The effect on the optical light curve of reducing the radius of the occulting material is also evidence against such an idea. The smaller radius effectively weights the central regions of the disc and thus produces an optical eclipse profile that is too deep, even if the profile width is maintained by emitting material outside the occulting structure.

I give in Table 5.4 the errors associated with the major parameters in the fits, allowing the other parameters freedom to compensate where possible. The fits are insensitive to changes in M_x which can vary between 0.8 and $1.6 M_\odot$. Varying K_x by ± 20 km s^{-1} has a similarly small effect. The inclination, i, is however well determined by the fitting. Unacceptable increases in χ^2_ν result if the inclination is altered by more than $\sim 3°$ from the best fit value (90% confidence). The radii of the accretion disc and the corona are determined as $7.3 \pm 0.7 \times 10^{10}$cm and $3.3 \pm 0.3 \times 10^{10}$cm respectively. To illustrate the results of the modelling, Fig. 5.9 shows three-dimensional views of the X 1822–371 binary model with the geometry fitted to the 1985 *EXOSAT* data.

As mentioned in Section 5.2.1 there is evidence that the minimum of the optical eclipse occurs about 3 mins (0.01 in phase) later than the X-ray eclipse. The modelling shows that the disc is not axisymmetric and therefore this result is not surprising. The optical eclipse can be considered as consisting of two components; the eclipse of the inner disc emission, which has a minimum prior to the X-ray phase 1.0, and the eclipse of the outer disc emission, which has a minimum after phase 1.0 (Fig. 5.8). The resulting model fits follow the data in having a minimum delayed by $\phi \sim 0.01$ compared to the X-ray eclipse.

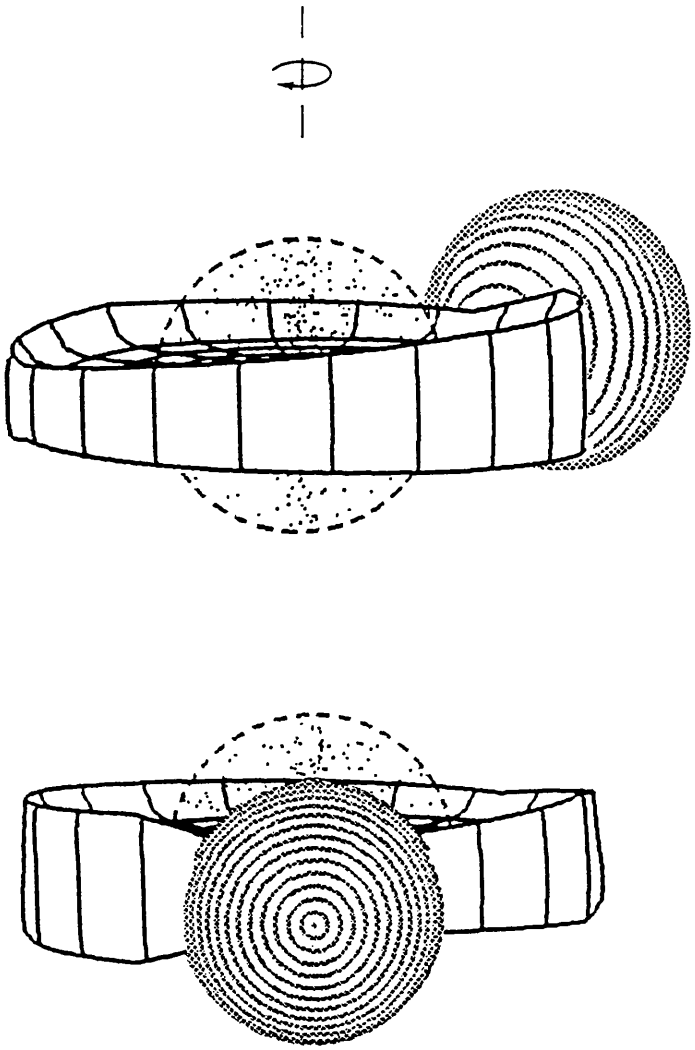

FIGURE 5.9: A three-dimensional view of the X 1822–371 binary system. The illustrated geometry is determined by a simultaneous model fit to the 1985 *EXOSAT* data and the optical light curve. The two views show the system as it appears at binary phase 0.6 and at phase 0.0 (mid eclipse). Centered on the primary is a spherical X-ray emitting ADC. This is surrounded by a thick accretion disc which hides the primary from view. The variable height of the disc rim causes the modulation in the X-ray light curve by obscuring the ADC. By summing the flux contribution from the projected area of the disc, allowing the inner and outer surfaces to have different emissivities, the optical light curve is reproduced.

5.4 Discussion

I have modelled the spectra of X 1822–371 by the sum of a power law and a black body component (Section 5.2.2). In models of LMXB spectra the power law is associated with

emission from the inner accretion disc while the black body component is thought to originate from the neutron star surface (White, Stella & Parmar 1988, White *et al.* 1986). For a distance of 3 kpc for X 1822–371 (MC) the measured black body parameters imply an emission region radius of 0.25 km, considerably smaller than a neutron star. A more typical value for observed black body radii is ~ 5 km (White *et al.* 1986). Hence the radius value implies that we see only $\sim 1/400^{\rm th}$ of the total flux in X 1822–371, suggesting that the scattering ADC is optically thin. This argument is consistent with the unusually low $L_x/L_{opt} = 20$ for X 1822–371 compared with a more typical LMXB value of 1000.

A major task for a model of X 1822–371 is to explain the spectral behaviour associated with the flux variations. There are no significant spectral changes with phase associated with the quasi-sinusoidal modulation that dominates the X-ray light curve. On top of the limitations imposed by photon statistics, the data contain non-periodic changes in the spectrum which are not completely averaged out when folded over the few cycles of the observations; thus an upper limit on a phase related spectral change, taking both these effects into account, is equivalent to a 5% change in hardness ratio. As shown in Section 5.2.2, there are spectral changes near the eclipse which produce 10% changes in hardness ratio. The eclipse itself is accompanied by a softening of the spectrum (Figs. 5.4, 5.5 & 5.6) while in the 1985 *EXOSAT* observation there is a hardening of the spectrum just prior to eclipse (Figs. 5.4 & 5.6). The simplest model consisting of an ADC of uniform effective temperature being occulted by an opaque disc rim with a sharp boundary naturally predicts the energy independence of the sinusoidal modulation, but is unable to explain the spectral changes near eclipse.

The softening of the spectrum during eclipse (where the ADC is being occulted by the sharp-edged secondary) suggests that the effective temperature of the ADC decreases with height above the disc plane. The spectral difference between the eclipse and the other regions of the light curve is adequately described by either a change in power law slope (from –0.9 to –1.0 in the 1984 data and from –0.8 to –1.0 in the 1985 data) or by a change in black body temperature (from 2.0 to 1.8 keV and from 1.8 to 1.6 keV in the two observations respectively). During mid eclipse the X-ray flux is approximately half the mean level out of eclipse. Thus if one associates the softer parameters with the upper region of the ADC then one expects that the lower region has parameters similarly harder than the mean values. The implied gradient in the ADC is then $0.3\,{\rm keV}/10^{10}{\rm cm}$ or, in power law slope, $0.2/10^{10}{\rm cm}$. The increase of iron line equivalent width during eclipse also suggests that the iron line emission originates mainly in the non-eclipsed portions of the system.

The probable existence of an energy gradient in the ADC raises the question of why the sinusoidal modulation depth does not also depend on energy, producing a softer spectrum at lower flux levels. With the geometry of the model fits, shown in Figs. 5.7 & 5.8, the height of the secondary projected onto the ADC is approximately twice that of the disc rim. If the temperature gradient were greatest in the upper part of the ADC then the eclipse occultation would result in the greatest spectral change. The varying obscuration by the disc rim of the more uniform lower regions of the ADC would nevertheless produce a spectral modulation by altering the relative proportions of the soft and hard X-ray emitting ADC regions, but, as the proportion of the total ADC area involved is lower, this variation would be smaller than that caused by the eclipse by a factor of ~ 2; such an effect is near the limit detectable in the data.

An analogy with Cyg X-3 suggests an alternative explanation for the energy independence of the sinusoidal modulation. It has been suggested (WH) that Cyg X-3 may also be an ADC source, principally because of its quasi-sinusoidal X-ray light curve which has a 4.8 hour period. In this system the modulation depth is energy dependent, showing a decrease with increasing energy (Molnar & Mauche 1986). This energy dependence is suggestive of photo-electric absorption as would occur if the ADC were occulted by a disc rim which does not have a sharp edge but has an optical depth decreasing with height above the disc plane. If this is the situation in Cyg X-3 then one might expect similar behaviour from X 1822–371. The decrease in modulation depth with increasing energy, caused by photo-electric absorption, might then combine with the increase in modulation depth caused by the decrease in ADC effective temperature with height, to produce a net energy dependence that is below the level detectable in the data. Inspection of Fig. 5.5 shows marginal evidence for a minimum in the modulation depth curve at ~ 5 keV such as might be expected from the combination of these two competing processes.

In this scenario one can explain the hardening of the spectrum just prior to eclipse as the result of increased photo-electric absorption dominating the spectrum. The extra disc structure at this phase may produce material with a greater scale height which consequently produces the extra photo-electric absorption. Such material may be associated with the impact of the mass stream from the secondary with the outer edge of the disc.

A further similarity between Cyg X-3 and X 1822–371 is suggested by the analysis of the X 1822–371 ephemeris. It is well established that the period of Cyg X-3 is increasing with a time scale $P/\dot{P} = 4.5 \times 10^5$ years (Molnar 1988). An increasing orbital period is the opposite of that expected from simple LMXB evolutionary theory if the secondary is a main sequence star and so far has been seen only in Cyg X-3. In Section 5.2.1, I advance

a tentative ephemeris for X 1822–371 which indicates that the period is changing in the same sense as that of Cyg X-3 with a timescale $P/\dot{P} = 1.8 \times 10^6$ years. This ephemeris is unsatisfactory being based on both X-ray and optical timings which may not be exactly coincident. Further X-ray observations are required to confirm the value of $\dot{P}$.

My modelling of the light curves of X 1822–371, fitting both the X-ray and optical data simultaneously, is in broad agreement with previous results (WH, MC) and confirms the viability of the ADC model. WH modelled the X-ray light curve with a flat disc on which they placed two saw-tooth bulges. As the disc height away from the bulges was fixed at the thin disc value, there was a large variation in height around the disc with the top of the highest bulge being 7 times as high as the thin disc. I have used a more general formulation which results in a flatter profile with a smaller variation in height, the range in disc thickness with azimuth being only a factor of 3. The fit to the 1984 *EXOSAT* observation data yields a single bulge around phase 0.8 which decays in both directions to a trough centered at phase 0.4 (Fig. 5.7). Fitting the 1985 data required a more complex profile (Fig. 5.8) which has bulges at similar phases to those of WH, a larger bulge at phase 0.8 and a lesser bulge around phase 0.2. The larger bulge is near the phase expected for the impact of an accretion stream with the disc while the presence of a second bulge is also supported by the optical spectroscopy of Mason *et al.* (1982).

My modelling determines the system inclination to be in the range 82°–87°. WH reported bulge parameters for the range 70°–80°, however they did not exclude fits at higher inclinations. The flatter bulge profile in my modelling obscures more of the ADC on average causing a larger fitted ADC radius and consequently a higher inclination to preserve the X-ray eclipse depth. I believe that the tighter constraint on the inclination arises because my more general modelling finds a better bulge profile that was not available to WH given the inbuilt constraints of their code. I am also fitting the model to X-ray data with complete phase coverage whereas WH were hampered by their highest quality data (from the *Einstein* MPC) being only 60% complete.

As the X-ray eclipse of X 1822–371 determines the absolute size of the ADC, the modelling also constrains the absolute size of the accretion disc. The disc has a radius ($7.3 \pm 0.7 \times 10^{10}$cm), approximately twice that of the ADC ($3.3 \pm 0.3 \times 10^{10}$cm, Section 5.3.2). These values correspond to 1.0 ± 0.1 and 0.47 ± 0.04 $R_\odot$ and compare with the values from WH which are 0.7 and 0.3 $R_\odot$. My values for these parameters are larger for similar reasons to those given above, the higher inclination and larger average height of the disc rim profile produce a larger ADC radius. The ratio of R_d to R_c is less dependent on these effects and here I am in agreement with WH. This ratio of the radius of the

obscuring material to that of the ADC is crucial to obtaining a fit to the X-ray data. My results (Section 5.3.3) indicate that its value must be ~ 2; this is similar to the value of the ratio of the width of the optical and X-ray eclipses and suggests that the obscuring bulges are located at the outer edge of the accretion disc. The modelling is therefore strong evidence against the proposal of Frank *et al.* (1987) that the obscuring structure is located at a smaller radius in the disc, at the circularisation radius of the gas stream.

The disc structure has a height above the plane of the disc of between 0.6 and 1.6×10^{10}cm, corresponding to an angle subtended at the primary of between 5° and 12°. Comparable results have been obtained for other (dipping) LMXB; Parmar *et al.* (1986) found that the highest disc structure in EXO 0748−676 subtends an angle in the range 8°–15° while Smale *et al.* (1988) reported a lower limit of 11° for similar structure in XB 1916−053. In my best fit model the disc structure is of sufficient height that, at the fitted inclination, the primary is never visible. This was not a requirement built into the model which allowed the possibility that the primary was rendered invisible by an optically thick ADC rather than the disc rim structure. The result supports the idea that the difference between X 1822–371 and a system such as EXO 0748−676 (Parmar *et al.* 1986) is mainly one of inclination. A small residual X-ray flux during the flat-bottomed eclipse of EXO 0748−676 suggests that it also possesses an ADC, but the X-ray light curve is dominated by large erratic dips characteristic of occultations of a point source. If the inclination of EXO 0748−676 were slightly increased from its value of 75° we would presumably only ever see the X-rays scattered by the ADC and thus a system with a smoother light curve and smaller L_x/L_{opt} ratio, similar to X 1822–371, would result.

Given the parameters affecting the X-ray light curve, the simultaneous fit to the optical light curve requires only two additional variables; an overall normalization and a relative normalization of the inner and outer accretion disc surfaces. Considering the limited number of degrees of freedom the resultant fit is excellent while the consistency between the X-ray and optical components of the model is a strong indication of its validity. MC compared the results from their modelling of the optical light curve with the overall spectrum of X 1822–371 to derive temperatures for the two main optically emitting regions and hence, with the modelled emitting areas, an estimate of the distance to the star (1–5 kpc). The errors of these estimates were dominated by uncertainty in interstellar reddening with the result that my modelling does not produce values significantly different from theirs. The optical modelling did not require a contribution from the secondary star. At a distance of 2 kpc, an unheated secondary would be $\sim 21^{st}$ magnitude in V (compared with a system magnitude of 16). To contribute significantly to the optical flux, say 25%,

the heated face would have to be at least 10 000 K. Such a contribution is not ruled out be the modelling.

The value for the orbital velocity of the primary star was reported to be $\sim 70 \mathrm{km\,s^{-1}}$ by Mason *et al.* (1982) and Cowley *et al.* (1982) from measurements of the high velocity wings of the emission lines. This determination depends on the assumption that the visible regions emitting this radiation are axisymmetric about the primary. The modelling indicates that the visibility of regions of the disc is highly dependant on orbital phase and thus the measured value of the orbital velocity should be treated with caution. Fortunately the details of the modelling are insensitive to variations in K_1, the effect being to scale the entire system rather than change relative sizes. Equally this means that the component masses are ill-determined and I cannot exclude masses much greater than used in the modelling.

5.5 Conclusions

I summarise the findings from three *EXOSAT* observations and optical photometry as follows.

1) The ADC model for X 1822–371 provides a good explanation of the X-ray and optical light curves of the star.

2) The dominant X-ray modulation is largely free of spectral changes. There are, though, spectral changes near eclipse; *vis.* a softening of the spectrum during eclipse and a hardening just prior to eclipse. The softening during eclipse implies a gradient in effective temperature of the ADC. The effect of this may be countered by photo-electric absorption in the disc producing the observed null energy dependence.

3) Analysis of the X-ray eclipses, together with optical data, suggests that the binary period is increasing on a time-scale of 1.8×10^6 years.

4) The optical and X-ray light curves can be simultaneously reproduced using disc structure parameterized by as few as two straight lines. The system inclination is $85° \pm 3°$, slightly higher then previously thought. The modelling fixes the absolute sizes of the X-ray emitting ADC and the optically emitting disc. It also places the X-ray obscuring material at the outer edge of the disc, rather than further in near the ADC radius.

CHAPTER 6

Overview

To conclude the thesis, I present an overview of the previous chapters. The bulk of the thesis is concerned with optical observations of the intermediate polars EX Hya and FO Aqr. In considering the implications for the intermediate polar class, it is useful to summarise the results from X-ray studies of intermediate polars which have proceeded largely in parallel with this work.

The X-ray light curves of all intermediate polars are modulated quasi-sinusoidally with the spin period. The modulation depth always increases at lower energies (e.g. Norton & Watson 1989). This led Rosen, Mason & Córdova (1988, RMC), studying the X-ray behaviour of EX Hya, to propose that photo-electric absorption is the dominant mechanism producing the spin modulation. Alternative mechanisms are occultation of the accretion region by the body of the white dwarf (first suggested by King & Shaviv 1986) and electron scattering in the accretion column (e.g. Buckley & Tuohy 1989). Both of these mechanisms yield energy independent modulations and so are not sufficient alone; they may, though, be a contributing factor, particularly at higher energies where absorption is not efficient.

RMC employ simple geometrical arguments to show that if the white dwarf accretes via a disc, then the flow onto the white dwarf is probably confined to a narrow arc around the magnetic pole, occupying $\sim 1\%$ of the surface area of the white dwarf. This results in an 'accretion curtain' whose cross-sectional area is small compared to its height. For EX Hya, RMC estimate that the dominant accretion shock occurs at a height of ~ 1 white dwarf radius, with most of the accretion energy being liberated in the sub-shock region. In such an accretion column the optical depth is least through its sides and greatest along its length. Thus, maximum light, corresponding to minimum photo-electric absorption, is expected when the column is viewed most nearly side on, i.e. when the magnetic pole points furthest away from the observer (see Fig. 6.1).

The X-ray results are thus in excellent agreement with the model derived from my optical studies of intermediate polars. In EX Hya and FO Aqr (and also AO Psc, Hellier, Cropper & Mason, in preparation) I have discovered a spin cycle S-wave feature in the

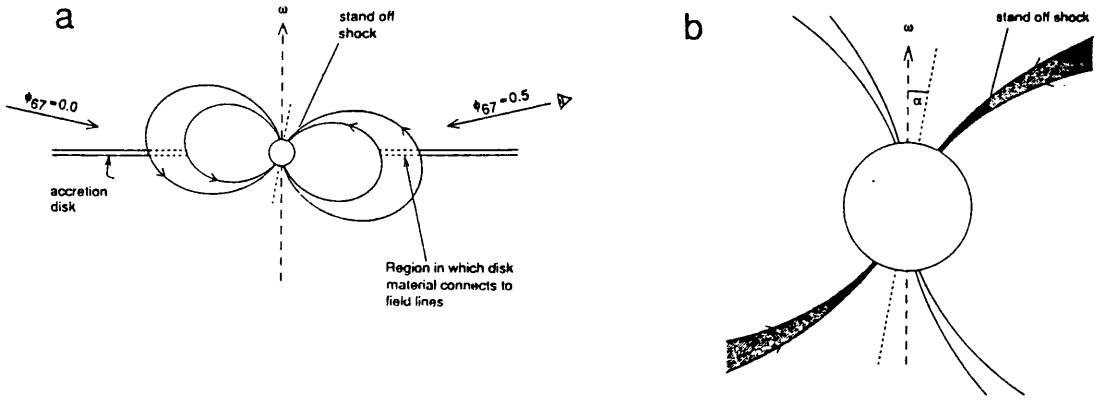

FIGURE 6.1: Schematic representation of the accretion geometry in EX Hya. The disc is disrupted by the magnetic field at 10 white dwarf radii. The material threads onto the field lines and is channelled onto the magnetic poles where it encounters a stand-off shock. The observer's views at phases 0.0 (maximum) and 0.5 (minimum) are indicated. The view at right is a close up of the inner regions showing the shock and the sub-shock region where most of the X-ray radiation is emitted. To produce a modulation, the magnetic dipole is offset by an angle α from the rotation axis. (From Mason, Rosen & Hellier 1988.)

emission lines, phased with maximum blue-shift at optical maximum light. In all of these cases optical and X-ray spin maxima are coincident. The blue-shift implies that the material is travelling towards the observer, which places the accretion curtain on the far side of the white dwarf at maximum light. The optical and X-ray modulations can thus be produced in a similar may (by absorption) which elegantly explains the similarity in their phasings and profiles. For a full account of the X-ray model and its relationship to the optical observations and previous models of the X-ray modulation see Mason, Rosen & Hellier (1988).

Given that all known intermediate polars have similar spin cycle X-ray behaviour, the model proposed here could well be applicable to all intermediate polars. One area which needs exploring is the intermediate polars (such as V1223 Sgr and TV Col) which show no optical photometric modulation at the spin period but only at the beat period between the spin and orbital periods. Preliminary work (Hellier *et al.*, in preparation) reveals that in V1223 Sgr the emission lines do show variations with the spin period and that the basic model is also applicable here. The continuum modulation may simply be at a lower amplitude due, possibly, to a lower system inclination.

Analysis of the emission lines, and their behaviour through eclipse, in the quiescent

EX Hya (Chapter 2) indicated that there is substantial line emitting material circulating the white dwarf between 10 white dwarf radii and ~ 40 white dwarf radii. Evidence for similar material was found in FO Aqr (Chapter 4). Conventionally this would be considered a viscously interacting Keplerian disc. Alternatively, Hameury, King & Lasota (1986) have proposed that in a 'discless' intermediate polar such material could be stripped from the accretion stream and forced to corotate with the magnetosphere, spiralling inwards or outwards depending on whether it is inside or outside the magnetosphere radius and on whether the white dwarf spin rate is at equilibrium. With corotating material, the highest velocities are furthest from the white dwarf, the opposite of the case with a Keplerian disc. The eclipses seen in EX Hya and FO Aqr offer the potential of mapping the velocity distribution of the circulating material and so distinguishing between the 'disc' and 'discless' intermediate polar models. This would need data with better statistical quality at higher time resolution than has so far been obtained, and would be complicated by the S-waves — possibly only eclipse ingress data would be useful.

The S-waves, though, provide information about the location of the impact region producing them. In EX Hya and FO Aqr the S-waves have velocities and phasings compatible with an impact of the accretion stream with the edge of a large Keplerian disc. Corotating material at a large radius would, in the case of FO Aqr, have a much larger velocity of ~ 2500 km s^{-1} compared with the observed S-wave semi-amplitude of 260 km s^{-1} (in EX Hya, due to the slow, 67-min spin period and smaller system size the corotation velocity is always lower than the Keplerian velocity). If the S-waves were produced by an impact with the magnetosphere at a smaller radius ($\sim 1\times10^{10}$ cm as suggested by Hameury *et al.* 1986), then later phasings would result and, if the observed velocity reflected the radial infall velocity acquired by the stream, high velocities would again be expected.

Just such a feature, with a late phasing and a high velocity, appears in EX Hya during outburst in addition to the lower velocity S-wave seen in quiescence (Chapter 3). To explain the two S-waves, I suggested that in outburst the accretion stream overflows the initial impact with the disc and continues to a second impact with the magnetosphere.

To account for the disc overflow, I proposed that an increase in the mass transfer rate from the secondary, rather than a disc instability, is the cause of the outburst. EX Hya is one of only two confirmed intermediate polars to exhibit dwarf nova like outbursts (the other being GK Per). In both of these systems the recurrence time is years rather than ~ 1 month as is typical for dwarf novae. Two other intermediate polars, TV Col and V1223 Sgr have produced 'flares' during which the optical flux increased by ~ 1 mag lasting for around 12 hr (Schwartz *et al.* 1988, van Amerongen & van Paradijs 1989). Because

of these differences it is not clear how relevant the EX Hya outburst model is to other systems, either intermediate polars or the dwarf novae. However, Angelini & Verbunt (1989) have considered the effect of magnetic disruption of the inner disc on a dwarf nova outburst. They find that generally the outbursts are shorter than would occur with a complete disc (the EX Hya outbursts are only two days long). They also predict that outbursts caused by disc instabilities are less frequent and of lower amplitude — possibly producing events similar to those seen in TV Col and V1223 Sgr.

The disc overflow model for EX Hya during outburst is supported by the calculations of Lubow (1989). He finds that the mass transfer stream can overflow the initial impact with the disc and that the overflow material falls back onto the disc near closest approach to the white dwarf (or in the case of intermediate polars, at the magnetosphere); this would produce the high velocity *S*-wave seen in EX Hya. Evidence for a similar interaction was observed by Marsh (1985) in the dwarf nova Z Cha. Lubow (1989), though, did not consider the vertical deflection of the stream by the accretion disc. I found (Chapter 4) that to explain spectra of FO Aqr, part of the stream needed to be deflected out of the plane at an angle of 60°. Recent Ginga X-ray observations (Norton, private communication) support this scenario. Absorption dips are seen recurring with the orbital cycle at the phase when the deflected stream is in front of the central X-ray source.

Similar X-ray dips are seen in other intermediate polars (e.g. EX Hya, Córdova, Mason & Kahn 1985; AO Psc, Pietsch *et al.* 1987 and BG CMi, McHardy *et al.* 1987) and non-magnetic CVs (e.g. U Gem, Mason *et al.* 1988). This suggests that 'thick discs' (including consideration of the out of the plane direction) are as important in CVs as they have been found to be in LMXBs, where they produce a range of behaviour from 'dipping' sources to the 'accretion disc corona' sources. Studying such behaviour leads to much of our information about accretion discs. My work modelling the disc in X 1822–371 (Chapter 5) is a good example and has resulted in the best 'picture' of an accretion disc so far. The disc structure in X 1822–371 must subtend an angle at the primary of 5°—12°, which agrees well with determinations in the dipping LMXB. Further evidence of the similarities between CVs and LMXBs in this respect is provided by the anomolous absorption seen in FO Aqr which has many parallels to the blue-shifted absorption seen in the LMXB AC211. Naylor *et al.* (1988) have suggested that this star is an ADC source similar to X 1822–371. The observational evidence is thus overwhelmingly against the assumption of a thin, axisymmetric disc commonly made to simplify theoretical disc models, and points to the need for a full three dimensional treatment including the perturbing effect of the secondary and the mass transfer stream.

APPENDIX A

V426 Oph: an intermediate polar?

A.1 Introduction

In this appendix to the thesis, I consider the classification of V426 Ophiuchi, particularly whether or not it is an intermediate polar. As there are currently only 8 well established intermediate polars (e.g. Osborne 1988), it is important for studies of the class that further candidates are genuinely intermediate polars. For example the correlation between their orbital and spin periods (e.g. Warner & Wickramasinghe 1989) would be distorted by imposters.

V426 Oph has an orbital period of 6.85 hr and is a Z Cam type dwarf nova varying between 11^{th} and 13^{th} magnitude (Hessman 1988). Szkody (1986) proposed that V426 Oph is also an intermediate polar, reporting a 60-min X-ray period from a 5-hr *EXOSAT* observation. In an attempt to confirm this status, I have obtained spectroscopy of this star and also reanalysed the *EXOSAT* data. I also present optical photometry gained by members of the University of Cape Town (O'Donoghue, private communication).

A.2 Observations and analysis

A.2.1 SPECTROSCOPY

Time resolved spectroscopy of V426 Oph was obtained on the night of 1988 August 8 using the 1.9-m telescope, Image Tube Spectrograph and Reticon Photon Counting System of the South African Astronomical Observatory. The series of spectra covered almost one orbit (6.5 hr) with a time resolution of 1 minute. The wavelength coverage was 4200–5000Å at a resolution of 1.2Å.

The summed spectrum is very similar to previously published spectra of V426 Oph (Williams 1983, Hessman 1988). Strong, broad Balmer lines have equivalent widths of 36Å (Hβ) and 30Å (Hγ). Weaker helium lines have equivalent widths of 6Å (He I λ4471) and 3Å (He II λ4686). The orbital variations of the lines have been well studied by Hessman

(1988) and the data are consistent with his analysis.

I have searched for shorter period line variations by calculating the equivalent widths of each line in the individual spectra and also the ratio of the equivalent widths on either side of the line rest wavelength (the V/R ratio). These quantities were then Fourier analysed (Fig. A.1). The results show significant power at the orbital timescale. There is also a peak at around 100 mins in the transform of equivalent widths; although suggestive of a period this could also be purely flickering behaviour and so is not significant without corroboration by other data sets. The presence of a spin period V/R variation is a common feature of intermediate polars (e.g. Penning 1985, Chapter 4), however the data show no significant periods shorter than the orbital period.

A.2.2 PHOTOMETRY

Four fast photometric time series, of duration 1.4, 2.0, 1.8 and 3.9 hr, were obtained at the SAAO on the nights of 1989 May 4/5, 5/6 and July 4/5 and 6/7. The light was unfiltered except during the third run when an R filter was used. V426 Oph was at quiescence ($13^{\rm th}$ mag or fainter) on all four occasions.

The light curves (Fig. A.2) show large amplitude (50% peak-to-peak) flickering on timescales from minutes to hours, producing low frequency power in the Fourier transforms (Fig. A.1). There is, however, no evidence for a consistent period in the optical photometry: the longest run sets a limit of 2% semi-amplitude for any such period shorter than 1200s; longer periods are large fractions of the data length and so flickering will not smear out, hindering the search for a period. At frequencies near the 1 hr period, there is a local minimum in the longest run's Fourier transform with a semi-amplitude of 2%.

A.2.3 X-RAY DATA

Having failed to find optical support for the suggested 60-min X-ray period, I have re-analysed the data from the *EXOSAT* satellite (White & Peacock 1988) to assess whether the period is significant or merely the result of flickering. The observation was made on 1984 September 25, details are given in the original report by Szkody (1986).

I show (Fig. A.3) the background subtracted LE (0.1–2keV) and ME (1.5–8.5 keV) light curves. Also shown is the hardness ratio derived from the ME data (defined as the ratio of the count rates in the bands 4.5–8.5 keV and 1.5–4.5 keV). The Fourier transforms of the LE and ME data (binned at 10 sec resolution) are displayed in Fig. A.1. Although there is power at the 60-min period in the ME data, it is not the largest peak and so cannot be regarded as significant. The largest peak, at around 0.13 mHz (130 mins), is

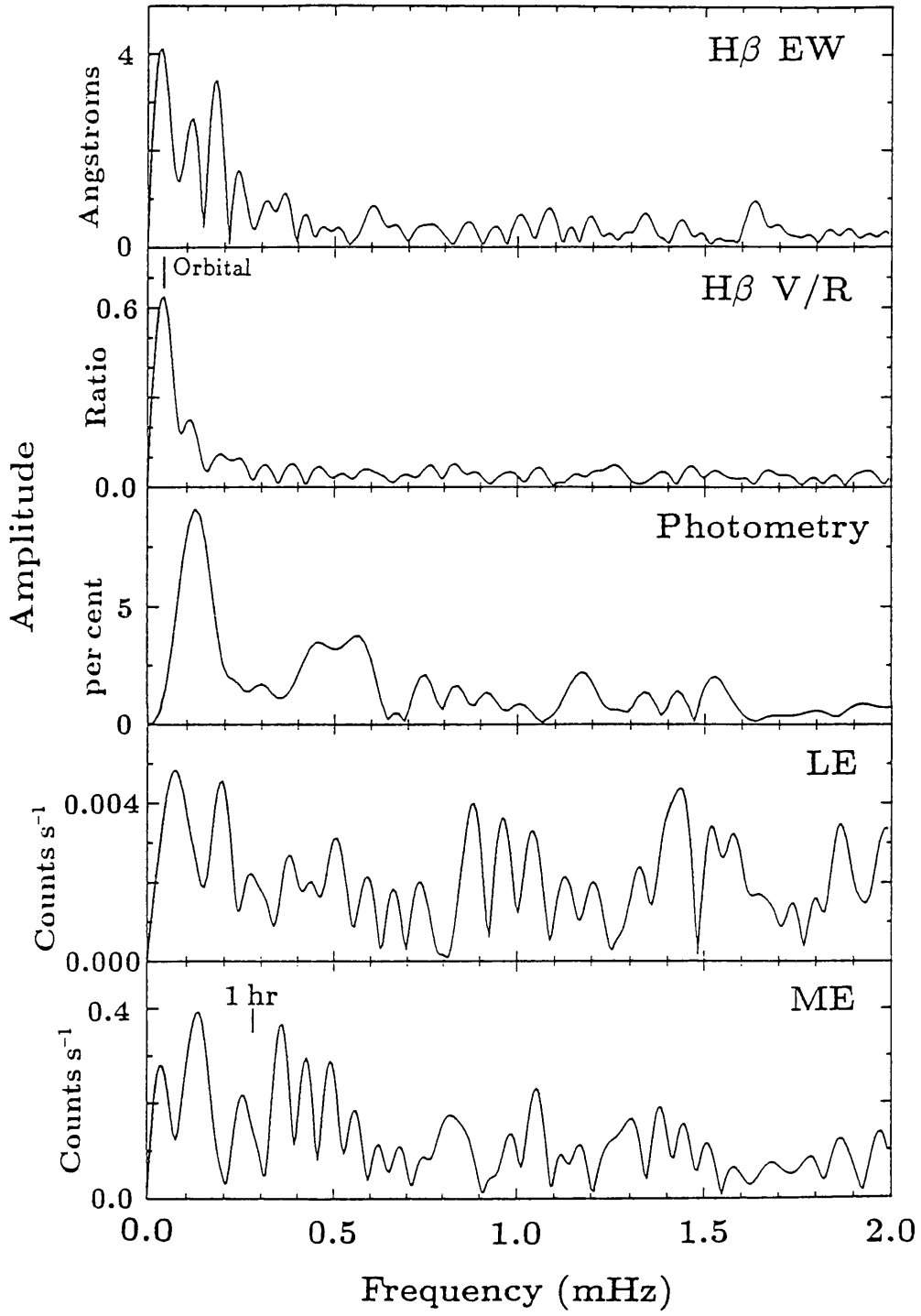

FIGURE A.1: Fourier transforms of, from the top, Hβ equivalent width, Hβ V/R ratio, July 6/7 photometry, *EXOSAT* LE (0.1–2.0 keV) data and ME (1.5–8.5 keV) data.

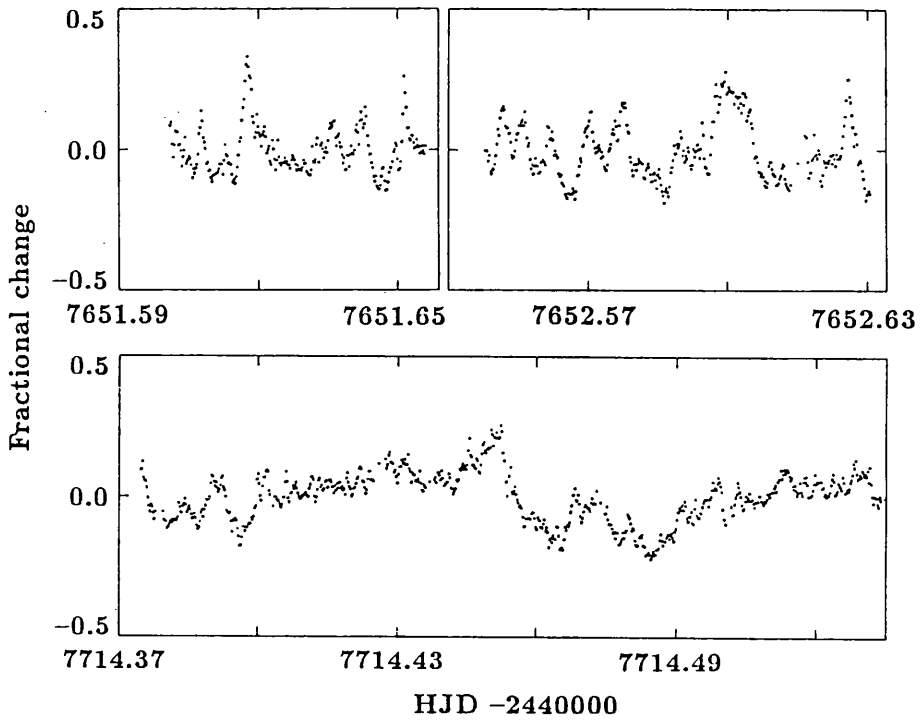

FIGURE A.2: Photometric light curves of V426 Oph from the nights of 1989 May 4/5, 5/6 and July 6/7 at a resolution of 20s. All were gathered in 'white light', the first two using the SAAO 0.75-m reflector with an S-11 response photomultiplier tube and the last using the SAAO 0.5-m reflector with an extended response S-20 tube.

only 10% larger than the next largest peak and only 20% larger than several others. Thus no peak is significant and the variability is attributable to flickering. The LE data are of low statistical quality and again show substantial flickering but no significant period.

A further test of whether the variability is related to intermediate polar spin behaviour is gained from the hardness ratio. In all confirmed intermediate polars the spin modulation is deepest at low energies, suggestive of absorption as the major cause (e.g. Norton & Watson 1989). The hardness ratio is therefore anti-correlated with the source intensity. In V426 Oph, however, accumulating the hardness ratio and intensity data in 5-min intervals I obtain a Spearman rank correlation coefficient of 0.29 (a positive correlation which is greater than zero with 90% confidence).

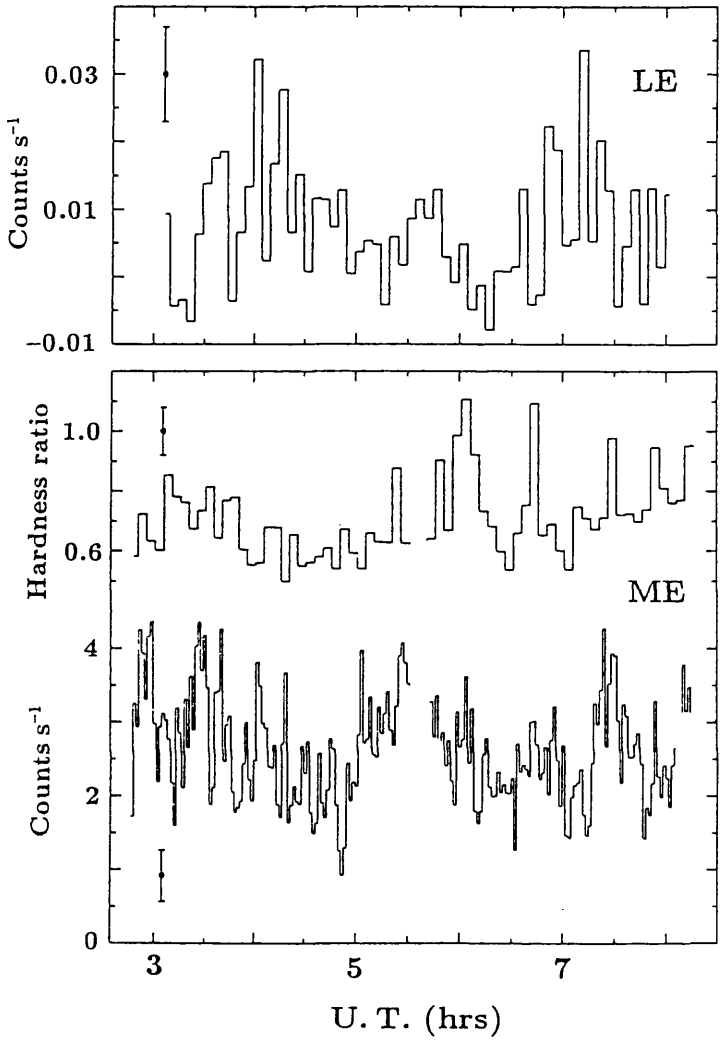

FIGURE A.3: *EXOSAT* X-ray light curves of V426 Oph taken on 1984 Sept 25. The LE (0.1–2.0 keV) data are binned to 5 min resolution. We also show the 1.5–8.5 keV data from the ME instrument (100-sec bins) together with the hardness ratio (4.5–8.5/1.5–4.5 count rate, 5-min bins).

A.3 Discussion

Intermediate polars are primarily distinguished by a second coherent periodicity in addition to, and normally much shorter than, the orbital variation. Secondary diagnostics include a strong, hard X-ray flux, typically greater than from non-magnetic cataclysmic variables, and prominent He II λ 4686 emission, often comparable in strength to the adjacent Hβ.

In the Fourier transforms of optical photometry, spectroscopy and X-ray data from V426 Oph (Fig. A.1), no peaks at frequencies shorter than the orbital period occur consistently in the different data sets. The peaks that are seen are entirely compatible with random flickering variability — such flickering is prominent in the optical and X-ray light curves (Figs. A.2 & A.3).

The X-ray flux from V426 Oph (*EXOSAT* ME count rate of 3 counts sec^{-1}) is comparable to that seen in other intermediate polars (see the tabulation in Szkody 1986). However, Hessman (1988) shows that the X-ray luminosity is also comparable to that of the very similar non-magnetic system SS Cyg. V426 Oph has only a weak He II λ 4686 line, with an equivalent width $\sim 10\%$ of the Balmer lines (Section A.2.1; see Williams 1983 for spectra of V426 Oph and magnetic systems). Additionally, the outburst behaviour of V426 Oph is not typical of intermediate polars. V426 Oph is a Z Cam type dwarf nova with outbursts recurring on a timescale of 22 days (Hessman 1988). Only two confirmed intermediate polars (EX Hya and GK Per) show dwarf-nova-like outbursts and these are much rarer, recurring on a timescale of years (the possible intermediate polar, SW UMa, is also a dwarf nova with an unusually long recurrence time; Shafter, Szkody & Thorstensen 1986).

I conclude that there is no evidence that V426 Oph is an intermediate polar. In particular, the necessary characteristic of a well established second coherent period is lacking.

Acknowledgements

Firstly, and most importantly, I thank my supervisor Keith Mason. I also wish to thank Len Culhane for having me in his laboratory and those who study (have studied) binary stars at MSSL, *vis.* Mark Cropper, Koji Mukai, Simon Rosen and Alan Smale for much advice, assistance, programs *etc.*

I also thank Alan Smale and Robin Corbet for giving me the EX Hya outburst data, Mark Cropper and Fred Marang for helping me obtain the FO Aqr data and Keith Mason for the quiescent EX Hya data and the *EXOSAT* X 1822–371 data. Also, I am grateful to Frank Bateson and the Royal Astronomical Society of New Zealand for visual light curves of EX Hya outbursts and Darragh O'Donoghue and others of the University of Cape Town for photometry of EX Hya in outburst and of V426 Oph.

I thank Michael Feast of the South African Astronomical Observatory for allocating substantial telescope time to my studies of intermediate polars and I acknowledge the SERC for grant support during my studentship.

Publications

The work reported in this thesis has also resulted in the following publications:

Hellier, C., Mason, K. O., Rosen, S. R. & Córdova, F. A. 1987.
'Time resolved optical spectroscopy of the eclipsing intermediate polar EX Hydrae'
Mon. Not. R. astr. Soc., **228**, 463.

Mason, K. O., Rosen, S. R. & Hellier, C. 1988.
'The accretion geometry of intermediate polars (DQ Her stars)'
Adv. Space Res., **8**, (2)293.

Hellier, C., Mason, K. O. & Cropper, M. S. 1989.
'An eclipse in FO Aquarii'
Mon. Not. R. astr. Soc., **237**, 39p.

Hellier, C., Mason, K. O., Smale, A. P., Corbet, R. H. D., O'Donoghue, D., Barrett, P. E. & Warner, B. 1989
'EX Hydrae in outburst'
Mon. Not. R. astr. Soc., **238**, 1107.

Hellier, C. & Mason, K. O. 1989.
'*EXOSAT* observations of X 1822–371: Modelling of the accretion disc rim'
Mon. Not. R. astr. Soc., **239**, 715.

Hellier, C., Mason, K. O. & Cropper, M. S. 1989.
'Spectroscopy of the intermediate polar FO Aquarii'
Mon. Not. R. astr. Soc., in press.

Hellier, C., O'Donoghue, D., Buckley, D & Norton, A. 1989.
'Is V426 Oph really an intermediate polar?'
Mon. Not. R. astr. Soc., submitted.

References

van Amerongen, S., & van Paradijs, J., 1989. *Astron. Astrophys.*, **219**, 195.

Angelini, L. & Verbunt, F., 1989. *Mon. Not. R. astr. Soc.*, **238**, 697.

Barrett, P., O'Donoghue, D. & Warner, B., 1988. *Mon. Not. R. astr. Soc.*, **233**, 759.

Bateson, F. 1987. *IAU Circ. No. 4383.*

Bateson, F. M. 1979. In: *Changing trends in variable star research*, IAU Colloq. 46, p. 89 *eds.* Bateson, Smak & Ulrich. Hamilton, New Zealand.

Bath, G. T. & Pringle, J. E. 1985. In: *Interacting Binary Stars*, p. 177 *eds.* J.E. Pringle & R.A. Wade, Cambridge University Press, Cambridge.

Berriman, G., Bailey, J., Axon, D. J. & Hough, J. H. 1986. *Mon. Not. R. astr. Soc.*, **223**, 449.

Berriman, G., Szkody, P. & Capps, R. W. 1985. *Mon. Not. R. astr. Soc.*, **217**, 327.

Beuermann, K. & Osborne, J. P. 1985. *Space Sci. Rev.*, **40**, 117.

Beuermann, K. & Osborne, J. P. 1988. *Astron. Astrophys.*, **189**, 128.

Bond, I. A., Freeth, R. V., Marino, B. F. & Walker, W. S. G. 1987. *Inf. Bull Var. Stars.*, 3037.

Bond, I. A. & Freeth, R. V. 1988. *Mon. Not. R. astr. Soc.*, **232**, 753.

Bonnet-Bidaud, J. M., Motch, C. & Mouchet, M. 1985. *Astron. Astrophys.*, **143**, 313.

Bonnet-Bidaud, J. M., Mouchet, M. & Motch, C. 1982. *Astron. Astrophys.*, **112**, 355.

Breysacher, J. & Vogt, N. 1980. *Astron. Astrophys.*, **87**, 349.

Buckley, D. A. H. & Tuohy, I. R. 1989. *Astrophys. J.*, in press

Buckley, D. A. H. & Tuohy, I. R. 1989. *Astrophys. J.*, in press

Chiappetti, L., Maraschi, L., Belloni, T., Bonnet-Bidaud, J. M., De Martino, D., Mouchet, M., Osborne, J., Tanzi, E. G. & Treves, A. 1988. In: *The Physics of Compact Objects*, *Adv. Space Res*, **8**, (2)309.

Clarke, J. T., Capel, D. & Bowyer, S. 1984. *Astrophys. J.*, **287**, 845.

Cook, M. C., Watson, M. G. & McHardy, I. M. 1984. *Mon. Not. R. astr. Soc.*, **210**, 7P.

Córdova, F. A. & Mason, K. O. 1983. In: *Accretion Driven Stellar X-ray Sources*, *eds.* Lewin, W. H. G. & van der Heuvel, E. P. J. Cambridge University Press.

Córdova, F. A. & Mason, K. O. 1984. *Mon. Not. R. astr. Soc.*, **206**, 879.

Córdova, F. A., Mason, K. O. & Kahn, S. M. 1985. *Mon. Not. R. astr. Soc.*, **212**, 447.

Córdova, F. A., Mason, K. O. & Nelson, J. E. 1981. *Astrophys. J.*, **245**, 609.

Cowley, A. P., Crampton, D. & Hutchings, J. B. 1982. *Astrophys. J.*, **255**, 596.

Cowley, A. P., Hutchings, J. B. & Crampton, D. 1981. *Astrophys. J.*, **246**, 489.

Cropper, M. S. 1986. *Mon. Not. R. astr. Soc.*, **222**, 225.

Cropper, M. S. 1989. *Space Sci. Rev.*, in press.

Eggleton, P. P. 1976. In: *The Strucure and Evolution of Close Binary Systems*, IAU Symp. No. 73 *eds.* P. Eggleton, S. Mitton & J. Whelan D. Reidel p. 209.

Eggleton, P. P. 1983. *Astrophys. J.*, **268**, 368.

Fabian, A. C., Pringle, J. E. & Rees, M. J. 1976. *Mon. Not. R. astr. Soc.*, **175**, 43.

Frank, J., King, A. P. & Lasota, J.-P. 1987. *Astron. Astrophys.*, **178**, 137.

Frank, J., King, A. R. & Raine, D. J. 1985. In: *Accretion power in astrophysics*, Cambridge University Press.

Friend, M. T., Martin, J. S., Smith, R. C. & Jones, D. H. P., 1988. *Mon. Not. R. astr. Soc.*, **233**, 451.

Gilliland, R. L. 1982. *Astrophys. J.*, **258**, 576.

Ghosh, P. & Lamb, F. K. 1979. *Astrophys. J.*, **234**, 296.

Greenstein, J. L. & Kraft, R. P. 1959 *Astrophys. J.*, **130**, 99.

Hameury, J.-M., King, A. R. & Lasota, J.-P. 1986. *Mon. Not. R. astr. Soc.*, **218**, 695.

Hassall, B. J. M., Pringle, J. E., Ward, M. J., Whelan, J. A. J., Mayo, S. K., Echevarria, J., Jones, D. H. P., Wallis, R. E., Allen, D. A. & Hyland, A. R. 1981. *Mon. Not. R. astr. Soc.*, **197**, 275.

Hellier, C. & Mason, K. O., 1989. *Mon. Not. R. astr. Soc.*, **239**, 715.

Hellier, C., Mason, K. O. & Cropper, M. S., 1989. *Mon. Not. R. astr. Soc.*, **237**, 39p.

Hellier, C., Mason, K. O., Rosen, S. R. & Córdova, F. A. 1987. *Mon. Not. R. astr. Soc.*, **228**, 463.

Hessman, F. V. 1988. *Astron. Astrophys. Suppl.*, **72**, 515.

Honey, W. B., Charles, P. A., Whitehurst, R., Barrett, P. E. & Smale, A. P. 1988. *Mon. Not. R. astr. Soc.*, **231**, 1.

Honeycutt, R. K., Kaitchuck, R. H. & Schlegel, E. M. 1987. *Astrophys. J. Suppl.*, **65**, 451.

Jablonski, F. & Busko, I. C. 1985. *Mon. Not. R. astr. Soc.*, **214**, 219.

Kaitchuck, R. H., Hantzios, P. A., Kakaletris, P, Honeycutt, R. K. & Schlegel, E. M. 1987. *Astrophys. J.*, **317**, 765.

Kaitchuck, R. H., Mansperger, C. S. & Hantzios, P. A. 1988. *Astrophys. J.*, **330**, 305.

King, A. R. 1986. In: *The physics of accretion onto compact objects, Lecture Notes in Physics, eds.* K. O. Mason, M. G Watson & N. E. White. Springer-Verlag **266**, 137.

King, A. R. 1988. *Q. Jl. R. astr. Soc.*, **29**, 1.

King, A.R., Frank, J. & Ritter, H. 1985. *Mon. Not. R. astr. Soc.*, **213**, 181.

King, A.R. & Shaviv, G. 1984. *Mon. Not. R. astr. Soc.*, **211**, 883.

de Korte, P.A.J., Bleeker, J.A.M., den Boggende, A.J.F., Branduardi-Raymont, G., Brinkman, A.C., Culhane, J.L., Gronenschild, E.H.B.M., Mason, I. & McKechnie, S.P. 1981. *Space Sci. Rev.*, **30**, 495.

Kruszewski, A., Mewe, R., Heise, J., Chlebowski, T., van Dijk, W. & Bakker, R. 1981. *Space Sci. Rev.*, **30**, 221.

Kubiak, M. & Krzeminski, W. 1989. Preprint

Kylafis, N.D. & Lamb, D.Q. 1982. *Astrophys. J. Suppl.*, **48**, 239.

Lamb, D.Q. & Melia, F. 1986. In: *The physics of accretion onto compact objects, Lecture Notes in Physics, eds.* K.O. Mason, M.G Watson & N.E. White. Springer-Verlag **266**, 113.

Lubow, S.H. 1989 *Astrophys. J.*, **340**, 1064.

Lubow, S.H. & Shu, F.H. 1975 *Astrophys. J.*, **198**, 383.

Marsh, T.R. 1985. Ph.D. thesis, Cambridge University.

Marsh, T.R., Horne, K. & Shipman, H.L. 1987. *Mon. Not. R. astr. Soc.*, **225**, 551.

Mason, K.O. 1986. In: *The physics of accretion onto compact objects, Lecture Notes in Physics, eds.* K.O. Mason, M.G Watson & N.E. White. Springer-Verlag **266**, 29.

Mason, K.O., Branduardi-Raymont, G., Córdova, F.A. & Corbet, R.H.D. 1987. *Mon. Not. R. astr. Soc.*, **226**, 423.

Mason, K.O. & Córdova, F.A. 1982a *Astrophys. J.*, **255**, 603.

Mason, K.O. & Córdova, F.A. 1982b *Astrophys. J.*, **262**, 253.

Mason, K.O., Córdova, F.A., Middleditch, J., Reichert, G.A., Bowyer, S, Murdin, P. & Clark, D. 1983. *Pub. Astr. Soc. Pacific*, **95**, 370.

Mason, K.O., Córdova, F.A., Watson, M.G. & King, A.R. 1988. *Mon. Not. R. astr. Soc.*, **232**, 779.

Mason, K.O., Middleditch, J., Nelson, J.E., White, N.E., Seitzer, P., Tuohy, I.R. & Hunt, L.K. 1980. *Astrophys. J.*, **242**, L109.

Mason, K.O., Murdin, P.G., Tuohy, I.R., Seitzer, P. & Branduardi-Raymont, G. 1982. *Mon. Not. R. astr. Soc.*, **200**, 793.

Mason, K.O. 1985. *Space Sci. Rev.*, **40**, 99.

Mason, K.O., Rosen, S.R. & Hellier, C. 1988. In: *The physics of compact objects, Adv. in Space Res.*, **8**, (2)293 *eds.* N.E.White & L.G.Filipov, Pergamon Press.

Mateo, M. 1985. In: *Ninth North American Workshop on Cataclysmic Variables*, p. 80 *eds.* P.Szkody. University of Washington, Seattle

Mattei, J. A. 1987. *IAU Circ. No. 4385.*

McClintock, J. E. & Rappaport, S. A. 1985. In: *Cataclysmic variables and Low-Mass X-Ray Binaries, eds.* D. Q. Lamb & J. Patterson D. Reidel **113**, 61.

McHardy, I. M., Pye, J. P., Fairall, A. P., Warner, B., Cropper, M. & Allen, S. 1984. *Mon. Not. R. astr. Soc.*, **210**, 663.

McHardy, I. M., Pye, J. P., Fairall, A. P. & Menzies, J. W. 1987. *Mon. Not. R. astr. Soc.*, **225**, 355.

Meyer, F. & Meyer-Hofmeister, E. 1984. *Astron. Astrophys.*, **132**, 143.

Molnar, L. A. 1988. *Astrophys. J.*, **331**, L25.

Molnar, L. A. & Mauche, C. W. 1986. *Astrophys. J.*, **310**, 343.

Mukai, K. & Charles, P. A. 1987. *Mon. Not. R. astr. Soc.*, **226**, 209.

Mumford, G. S. 1967 *Astrophys. J. Suppl.*, **15**, 1.

Naylor, T., Charles, P. A., Drew, J. E. & Hassall, B. J. M., 1988. *Mon. Not. R. astr. Soc.*, **233**, 285.

Norton, A. J. & Watson, M. G. 1989. *Mon. Not. R. astr. Soc.*, **237**, 853.

Osborne, J. P. 1988. *Mem. S. A. It.*, **59**, 117.

Osborne, J. P. & Mukai, K. 1988. *IAU Circ. No. 4657.*

Osborne, J. P. & Mukai, K., 1989. *Mon. Not. R. astr. Soc.*, **238**, 1233.

Osborne, J. P., Rosen, S. R., Mason, K. O. & Beuermann, K. 1985. *Space Sci. Rev.*, **40**, 143.

Parmar, A. N. & White, N. E. 1988. *Mem. S. A. It.*, **59**, 147.

Parmar, A. N., White, N. E., Giommi, P. & Gottwald, M. 1986. *Astrophys. J.*, **308**, 199.

Patterson, J. 1984. *Astrophys. J. Suppl.*, **54**, 443.

Patterson, J. 1979. *Astrophys. J.*, **234**, 978.

Patterson, J., 1988. *Inf. Bull. Var. Stars*, No. 3264.

Patterson, J., Branch, D., Chincarini, G. & Robinson, E. L. 1980. *Astrophys. J.*, **240**, L133.

Patterson, J. & Steiner, J. E. 1983. *Astrophys. J.*, **264**, L61.

Peacock, A., Andresen, R. D., Manzo, M., Taylor, B. G., Villa, G., Re, S., Ives, J. C. & Kellock, S. 1981. *Space Sci. Rev.*, **30**, 525.

Penning, W. R. 1985. *Astrophys. J.*, **289**, 300.

Penning, W. R., Schmidt, G. D. & Leibert, J. 1986. *Astrophys. J.*, **310**, 885.

Pietsch, W., Pakull, M., Tjemkes, S., Voges, W., Kendziorra, E. & van Paradijs, J. 1984. In: *X-ray Astronomy '84. International Symposium on X-ray Astronomy, Bologna, Italy*, 67 *eds.* Oda, M. & Giacconi, R. Institute of Space & Astronautical Science.

Pietsch, W., Voges, W., Kendziorra, E. & Pakull, M. 1987. *Astrophysics & Space Science*, **130**, 281.

Press, W.H., Flannery, B.P., Teukolsky, S.A. & Vetterling, W.T. 1986. In: *Numerical Recipes*, Cambridge University Press.

Rappaport, S.A. & Joss, P.C. 1983. In: *Accretion Driven Stellar X-Ray Sources, eds.* W.H.G.Lewin & E.P.J.van der Heuvel CUP p. 1.

Rappaport, S.A. Verbunt, F. & Joss, P.C. 1983. *Astrophys. J.*, **275**, 713.

Robinson, E. L. 1976. *Ann. Rev. Astron. & Astrophys*, **14**, 119.

Robinson, E. L. & Nather, R. E. 1983. *Astrophys. J.*, **273**, 255.

Rosen, S.R. 1987. *Ph.D. Thesis*, University of London.

Rosen, S.R., Mason, K.O. & Córdova, F.A. 1987. *Mon. Not. R. astr. Soc.*, **224**, 987.

Rosen, S.R., Mason, K.O. & Córdova, F.A. 1988. *Mon. Not. R. astr. Soc.*, **231**, 549.

Schneider, D.P. & Young, P.J. 1980. *Astrophys. J.*, **238**, 946.

Schrijver, J., Brinkman, A.C. & Van Der Woerd, H. 1987 *Astrophysics and Space Science*, **130**, 261.

Schwarz, H., van Amerongen, S., Heemskerk, M.H.M. & van Paradijs, J. 1988. *Astron. Astrophys.*, **202**, L16.

Semeniuk, I. & Kaluzny, J., 1988. *Acta Astr.*, **38**, 49.

Shafter, A.W. 1985. In: *Cataclysmic variables and Low-Mass X-Ray Binaries, eds.* D.Q.Lamb & J.Patterson D. Reidel **113**, 355.

Shakura, N.I. & Sunyaev, R.A. 1973 *Astron. Astrophys.*, **24**, 337.

Shapiro, S.L. & Teukolsky, S.A. 1983. In: *Black holes, white dwarfs and neutron stars. The physics of compact objects.*, Wiley. New York.

Shafter, A.W. & Macry, J.D. 1987. *Mon. Not. R. astr. Soc.*, **228**, 193.

Shafter, A.W., Szkody, P. & Thorstensen, J.R. 1986. *Astrophys. J.*, **308**, 765.

Shafter, A.W. & Targan, D.M. 1982. *Astr. J.*, **87**, 655.

Smale, A.P., Mason, K.O., White, N.E. & Gottwald, M. 1988. *Mon. Not. R. astr. Soc.*, **232**, 647.

Spruit, H.C. & Ritter, H. 1983 *Astron. Astrophys.*, **124**, 267.

Sterken, C., Vogt, N., Freeth, R., Kennedy, H.D., Marino, B.F., Page, A.A. & Walker, W.S.G. 1983. *Astron. Astrophys.*, **118**, 325.

Stone, R.P.S. & Baldwin, J.A. 1983. *Mon. Not. R. astr. Soc.*, **204**, 347.

Szkody, P. 1986. *Astrophys. J.*, **301**, L29.

Tuohy, I.R., Buckley, D., Remillard, R., Bradt, H.V. & Schwartz, D.A. 1986. *Astrophys. J.*, **311**, 275.

Turner, M. J. L., Smith, A. & Zimmermann, H. U. 1981. *Space Sci. Rev.*, **30**, 513.

Verbunt, F. 1987. *Astr. Astrophys. Suppl.*, **71**, 339.

Vogt, N., Krzeminski, W. & Sterken, C. 1980. *Astron. Astrophys.*, **85**, 106.

Warner, B. 1987. *Mon. Not. R. astr. Soc.*, **227**, 23.

Warner, B. 1976. In: *The Strucure and Evolution of Close Binary Systems*, IAU Symp. No. 73 *eds.* P. Eggleton, S. Mitton & J. Whelan D. Reidel p. 85.

Warner, B. 1983. In: *Cataclysmic variables and related objects*, *eds.* M. Livio & G. Shaviv D. Reidel **101**, 155.

Warner, B. 1985. In: *Cataclysmic variables and Low-Mass X-Ray Binaries*, *eds.* D. Q. Lamb & J. Patterson D. Reidel **113**, 269.

Warner, B., 1986. *Mon. Not. R. astr. Soc.*, **219**, 347.

Warner, B. & Cropper, M. 1984. *Mon. Not. R. astr. Soc.*, **206**, 261.

Warner, B. & McGraw, J. T. 1981. *Mon. Not. R. astr. Soc.*, **196**, 59p.

Warner, B. & Wickramasinge, D. T. 1989. preprint.

Watson, M. G. 1986. In: *The Physics of Accretion onto Compact Objects*, *eds.* K. O. Mason, M. G. Watson & N. E. White Springer-Verlag **266**, 97.

Watson, M. G., King, A. R. & Osborne, J. 1985. *Mon. Not. R. astr. Soc.*, **212**, 917.

Watts, D. J., Giles, A. B., Greenhill, J. G., Hill, K. & Bailey, J. 1985. *Mon. Not. R. astr. Soc.*, **215**, 83.

Watts, D. J., Greenhill, J. G., Hill, P. W. & Thomas, R. M. 1982. *Mon. Not. R. astr. Soc.*, **200**, 1039.

White, N. E., Becker, R. H., Boldt, E. A., Holt, S. S., Serlemitsos, P. J. & Swank, J. H. 1981. *Astrophys. J.*, **247**, 994.

White, N. E. & Holt, S. S. 1982. *Astrophys. J.*, **257**, 318.

White, N. E. & Marshall, F. E. 1981. *Astrophys. J.*, **249**, L25.

White, N. E. & Mason, K. O. 1985. *Space Sci. Rev.*, **40**, 167.

White, N. E. & Peacock, A. 1988. *Mem. S. A. It.*, **59**, 7.

White, N. E., Peacock, A., Hasinger, G., Mason, K. O., Manzo, G., Taylor, B. G. & Branduardi-Raymont, G. 1986. *Mon. Not. R. astr. Soc.*, **218**, 129.

White, N. E., Stella, L. & Parmar, A. N. 1988. *Astrophys. J.*, **324**, 363.

Williams, G. 1983. *Astrophys. J. Suppl.*, **53**, 523.

Young, P. J. & Schneider, D. P. 1980. *Astrophys. J.*, **238**, 955.

Young, P. J. & Schneider, D. P. 1981. *Astrophys. J.*, **247**, 960.

Young, P. J., Schneider, D. P. & Shectman, S. A. 1981. *Astrophys. J.*, **245**, 1035.